Sunlight on
Atmospheric Water Vapor and Mineral Aerosol

Modeling the Link between
Laboratory Data and Remote Sensing

Sunlight on
Atmospheric Water Vapor and Mineral Aerosol

Modeling the Link between
Laboratory Data and Remote Sensing

een wetenschappelijke proeve op het gebied van de
Natuurwetenschappen, Wiskunde en Informatica

Proefschrift

ter verkrijging van de graad van doctor
aan de Radboud Universiteit te Nijmegen
op gezag van de Rector Magnificus prof. dr. C.W.P.M. Blom,
volgens besluit van het College van Decanen
in het openbaar te verdedigen op donderdag 21 april 2005
des namiddags om 1.30 uur precies
door

Ben Veihelmann

geboren op 17 augustus 1972
te Werneck, Duitsland

Promotor: prof.dr. Wim J. van der Zande
Copromotor: dr. Ahilleas N. Maurellis, Nationaal Instituut voor
Ruimteonderzoek (SRON), Utrecht, Nederland

Manuscriptcommissie:
dr. Paul Groot, Radboud Universiteit Nijmegen
prof.dr. Jonathan Tennyson, University College London, UK
dr. Oleg Dubovik, NASA Goddard Earth Sciences and Technology
Center, University of Maryland Baltimore County, MD, USA

ISBN 90-6464-866-2

Radboud University
Nijmegen

FOM Institute for
Atomic and Molecular
Physics

National Institute for
Space Research

This work has been carried out at the FOM Institute for Atomic and Molecular Physics (AMOLF), the Radboud University Nijmegen, and the National Institute for Space Research (SRON). The work is part of the research program of the 'Stichting voor Fundamenteel Onderzoek der Materie (FOM)', which is financially supported by the 'Nederlandse Organisatie voor Wetenschappelijk Onderzoek (NWO)' and is supported by the grants EO-023 and EO-046 from the User Support Programme managed by the Programme Bureau of external research of the National Institute for Space Research (PB-SRON).

Für meine Eltern
For Georgiana

Contents

Preface

This thesis reflects my research activities of the last four years in the Atmospheric Photophysics Group at the FOM-Institute for Atomic and Molecular Physics (AMOLF) and in the Earth Oriented Science Group at the National Institute for Space Research (SRON). I worked on two subjects that are very different at first sight, namely on water vapor absorption spectroscopy (Chapters 1-3) and the light scattering properties of mineral dust aerosol (Chapter 4-8). This preface is meant to show the common elements of the two studies and to report briefly how this work has been accomplished. Comprehensive introductions to both topics are given in Chapters 1 and 4.

The Atmospheric Photophysics Group has been active in the research related to atmospheric water vapor, which is one of the most important agents in the Earth's radiation balance [*Kiehl and Trenberth*, 1997]. These activities include the development of algorithms for the detection of atmospheric water vapor using the satellite-borne sensor GOME (Global Ozone Monitoring Experiment) [*Maurellis et al.*, 2000]. The retrieval of water vapor is based on observations of scattered sunlight in the visible and near infrared part of the electro-magnetic spectrum. Spectral sampling techniques were developed for the treatment of the complex absorption spectra of water vapor [*Lang et al.*, 2002]. New water vapor absorption data were obtained from Cavity Ring Down Spectroscopy measurements [*Naus et al.*, 2001] (at the Vrije Universiteit Amsterdam). The retrieval of water vapor depends crucially on the detailed and accurate knowledge of the water vapor absorption as a function of the wavelength. The accurate characterization of this absorption spectrum is challenging from both a theoretical as well as from an experimental point of view [*Bernath*, 2002]. That is why the first part of this thesis is dedicated to the evaluation of spectroscopic data of water vapor.

Our strategy is to validate the spectroscopic data in the context of radiative transfer calculations for the Earth's atmosphere. For this purpose, ground-based measurements of the direct solar radiation with a very high spectral resolution are used [*Smith et al.*, 2001]. Individual absorption lines, which make up the fine structure of the measured spectrum, can be resolved with the spectral resolution of the ground-based spectrometer. We use the sun as light source and measure the absorption of light by atmospheric water vapor under atmospheric conditions. The results of this atmospheric long path absorption experiment are therefore directly relevant for radiative transfer simulations and water vapor retrievals in the Earth's atmosphere. The measurements are evaluated using radiative transfer simulations. In the ideal case, the solar spectrum at the top of the atmosphere as well as the atmospheric profiles of pressure, temperature, and water vapor abundance are known and instrument noise is absent. In this case, differences between simulations and observations could be assigned directly to errors in the spectroscopic data. Naturally, the real measurement is contaminated with noise. The solar spectrum as well as the atmospheric data are known with a limited accuracy. Therefore, it is necessary to examine the limitations of the validation of spectroscopic data based on this kind of ground-based measurement. We establish a general methodology to quantify the information that a ground-based measurement can add to existing spectroscopic data (Chapter 2). This allows an automatic selection of lines, for which the line parameters can be improved based on the ground-based measurement. This methodology is applied in a case study to the validation water vapor spectroscopy in the spectral region close to the wavelength of $\lambda = 720$ nm. Various databases are scanned for line parameter errors. The results of this error detection are validated using independent high-accuracy data. For the spectral region close $\lambda = 600$ nm, the amplitude of line intensity parameters are derived for absorption lines that show little blending with other lines (Chapter 3). A quality estimate is made for various spectroscopic databases. Both wavelength regions are relevant for the retrieval of water vapor from satellite-borne sensors with a moderate spectral resolution such that individual absorption lines are not resolved in the measured spectra. The implications of line intensity errors for such satellite-based observations are discussed.

The second part of this thesis is dedicated to irregular mineral dust aerosol. A significant fraction of the atmospheric aerosol load is mineral dust aerosol [*D'Almeida et al.*, 1991]. Mineral aerosol has a significant impact on the Earth's radiation balance and on the dynamics and the properties of clouds [*Tegen et al.*, 1996; *Haywood and Boucher*, 2000]. Aerosols are monitored using observations of scattered and transmitted sunlight from ground-based and satellite-borne sensors [*Holben et al.*, 1998; *Kaufman et al.*, 2002]. For the retrieval of aerosol parameters such as the amount, the type, and the size distribution from these observations an accurate knowledge of the light scattering properties is required. The light scattering properties of aerosols depend amongst others on the particle shape. The numerical simulations of light scattering by irregularly-shaped particles is very difficult. That is why shape approximations are used for aerosol retrievals and for radiative transfer simulations in planetary atmosphere containing irregularly-shaped mineral aerosol [cf. *Mishchenko et al.*, 1995, 1996]. In this thesis we make the link between measurements and simulations of the light scattering properties of irregular mineral aerosol.

The light scattering experiment, which was moved to the Atmospheric Photophysics Group at AMOLF in 2001, is a unique facility for the measurement of scattering matrices of irregular mineral dust aerosol samples [*Volten et al.*, 2001]. The scattering matrix describes how the intensity and the polarization of light is changed by a single scattering event. The scattering matrices of about 15 different mineral dust samples have been measured with this experimental setup. The goal of the work presented in this thesis is to validate and improve numerical light scattering techniques using the measurements as reference. For this purpose, the mineral samples have to be characterized regarding the refractive index and the size distributions. We present a study dedicated to the measurement of the size distribution of mineral samples using a laser particle sizer (Chapter 5). This laser particle-sizing technique has been developed for particle sizes much larger than the wavelength. The mineral samples that we use as references have a significant fraction of particles with size comparable to the wavelength. The accuracy of the size distributions thus obtained is investigated and the systematic errors of simplifying assumptions are quantified. The refractive index can be determined based on the mineral composition of a sample. The mineral composition of two samples is well-known. These samples originate from ground material of bulk crystals, i.e. quartz and feldspar. The measurements of these two samples are therefore particularly valuable for the validation and testing of light scattering models.

The light scattering model used for monitoring of aerosols from ground-based observations [*Dubovik et al.*, 2002] approximates the particle shapes with spheroids. We examine the consistency of this light scattering model with various measurements including the measurements of feldspar, quartz and two clay samples (Chapter 6). A series of three collaborative studies is based on the feldspar measurement [*Nousiainen et al.*, 2004; *Kahnert et al.*, 2004; *Veihelmann et al.*, 2004]. The first study is dedicated to the validation and testing of a shape approximation using polyhedral prisms and spheroids. The second study has as its objective the impact of the spheroidal and the spherical shape approximations on aerosol climate forcing and radiative flux simulations. The third study is included in this thesis as Chapter 7. Here, a statistical shape model using Gaussian random spheres is tested. In this model, the morphology of the model particles is based on a statistical shape analysis using microscopy images of the true irregular particles. In Chapter 8 we perform radiative transfer calculations for a dust-loaded atmosphere over the ocean. We estimate the impact of shape approximations on polarimetric observations for various scenarios that are typical for satellite observations of reflected sunlight.

Both parts of this thesis are related to the optical properties of important components of the Earth's atmosphere. My objective is to improve the knowledge required to simulate the interaction of these components with sunlight. This knowledge plays a key role in monitoring the atmospheric components from satellite observations. In both cases I exploit experimental data to validate and test existing models used in radiative transfer simulations and retrievals. I address questions such as:

· How accurately do we know the optical properties of an atmospheric component?
· How accurately can we model the radiative transfer?
· How much information can experiments add to this knowledge?
· What is the impact of uncertainties on satellite observations?

Bibliography

D'Almeida, G. A., P. Koepke, and E. P. Shettle, *Atmospheric Aerosol Global Climatology and Radiative Characteristics*, Deepak Publ., 1991.

Bernath, P. F., The spectroscopy of water vapor: Experiment, theory and applications, *Phys. Chem. Chem. Phys., 4*, 1501–1509, 2002.

Dubovik, O., B. N. Holben, T. Lapyonok, A. Sinyuk, M. I. Mishchenko, P. Yang, I. Slutsker, Non-spherical aerosol retrieval method employing light scattering by spheroids, *Geophys. Res. Lett., 29*, doi:10.1029/2001GL014506, 51-1, 2002.

Haywood J. and O. Boucher, Estimates of the direct and indirect radiative forcing due to tropospheric aerosols: a review, *Reviews of Geophysics, 38(4)*, 513–543, 2000.

Holben, B. N. and coautors, A federated instrument network and data archive for aerosol characterization. *Remote Sens. Environ., 66*, 1–16, 1998.

Kahn, R., R. West, D. McDonald, B. Rheingans, and M. I. Mishchenko, Sensitivity of multi-angle remote sensing observations to aerosol sphericity, *J. Geophys. Res., 102*, 16861–16870, 1997.

Kahnert F. M., T. Nousiainen and B. Veihelmann, Spherical and Spheroidal model particles as an error source in aerosol climate forcing and radiation computations: a case study for feldspar aerosols, *J. Geophys. Res.*, accepted

Kaufman, Y., D. Tanré, and O. Bouché, A satellite view of aerosols in the climate system, *Nature, 419*, 215–223, 2002.

Kiehl, J. T., and K. E. Trenberth, Earth's annual mean global energy budget, *Bull. Am. Meteorol. Soc., 78*, 197–208, 1997.

King, M., Y. Kaufman, D. Tanré, and T. Nakajima, Remote sensing of tropospheric aerosols from space: Past, present, future, *Bull. Am. Meteor. Soc., 80*, 2229–2259, 1999.

Lang, R., A. N. Maurellis, W. J. van der Zande, I. Aben, J. Landgraf, and W. Ubachs, Forward modelling and retrieval of water vapor from GOME: Treatment of narrow band absorption spectra, *J. Geophys. Res., 107*, 10.1029/2001JD001453, 2002.

Maurellis, A. N., R. Lang, W. J. Van der Zande, I. Aben, and W. Ubachs, Precipitable Water Column Retrieval from GOME Data, *Geophys. Res. Lett., 27*, 903–906, 2000.

Mishchenko, M. I., A. A. Lacis, B. E. Carlson and L. D. Travis, Nonsphericity of dust-like tropospheric aerosols: implications for aerosol remote sensing and climate modeling, *Geophys. Res. Lett., 22*, 1077–1080, 1995.

Mishchenko, M. I., L. D. Travis, and A. Macke, Light scattering by nonspherical particles: An overview, *Proceedings of the International Radiation Symposium*, edt. W. L. Smith and K. Stamnes, 1996.

Naus, H., W. Ubachs, P. F. Levelt, O. L. Polyansky, N. F. Zobov, and J. Tennyson, Cavity-Ring-Down Spectroscopy on Water Vapor in the Range 555–604 nm, *J. of Molec. Spectroscopy, 205*, 117–121, 2001.

Nousiainen, T., F. M. Kahnert and B. Veihelmann, Light scattering modeling of small feldspar particles using simplified shapes, *JQSRT*, accepted.

Smith, K. M., D. A. Newnham, and R. G. Williams, Collision-induced absorption of solar radiation in the atmosphere by molecular oxygen at 1.27 μm: Field observations and model calculations, *J. Geophys. Res., 106*, 7541–7552, 2001.

Tegen. I., A. A. Lacis, and I. Fung, The influence on climate forcing of mineral aerosols from disturbed soils, *Nature, 380*, 419–422, 1996.

Volten, H., O. Muñoz, E. Rol, J. F. de Haan, W. Vassen , J. W. Hovenier, K. Muinonen, T. Nousiainen, Scattering matrices of mineral particles at 441.6 nm and 632.8 nm, *J. Geophys. Res., 106*, 17375–17401, 2001.

Veihelmann, B., T. Nousiainen, F. M. Kahnert and W. J. van der Zande, Light scattering by small feldspar particles simulated using the discrete dipole approximation for Gaussian random spheres, to be submitted.

Chapter 1

Atmospheric Water Vapor

1.1 Introduction

Water is an atmospheric component with a very pronounced spatial and temporal variability. The largest part of the atmospheric water is present in the form of water vapor. If all the atmospheric water were to be condensed and distributed evenly on the entire Earth surface it would make up a layer of 25 mm liquid water [*Roedel*, 1992]. Water vapor is one of the most important agents in the Earth's radiation balance. It is responsible for 70% of the atmospheric absorption of solar radiation [*Ramanathan and Vogelmann*, 1997]. This absorption takes place mainly in the wavelength region between 700 nm and 2 μm [*Kiehl and Trenberth*, 1997]. The solar radiation reaching the ground is reduced and the lower atmosphere, where most of the water vapor is present, is heated. Also, water vapor acts as a greenhouse gas, accounting for 60% of the atmospheric absorption of the thermal radiation emitted from the Earth surface that otherwise would escape to space. This absorption takes mainly place at wavelengths around 7 μm and 19 μm close to the so-called atmospheric window, where the largest part of the thermal radiation of the Earth surface escapes to space [*Kiehl and Trenberth*, 1997]. Altogether, water vapor is responsible for the fact that the global average of the Earth's surface temperature is approximately 13° C rather than $-17°$ C [*Bernath*, 2002].

Liquid water has a very large heat capacity. Evaporation of liquid water at the Earth surface consumes a large amount of energy. This energy is released during condensation processes in the atmosphere. This so-called latent heat flux is the most efficient non-radiative energy transport controlling the surface energy balance [*Roedel*, 1992]. Clouds are an important agent in the weather and climate system. First of all, clouds reflect both solar radiation as well as terrestrial thermal radiation. Clouds and precipitation control the daily weather. On long time scales, the removal of the greenhouse gas water vapor from the atmosphere by precipitation is of climatic relevance.

The absorption of light by water vapor strongly depends on the wavelength. The absorption as a function of the wavelength is called the absorption spectrum. The absorption spectrum of water vapor comprises thousands of narrow absorption maxima, so-called absorption lines. The intensity, the position, and the shape of the absorption lines are described using spectroscopic parameters. The water vapor absorption spectrum and the spectroscopic parameters used for radiative transfer simulations are introduced in sections 1.2 and 1.3. Due to the complexity of the water molecule, the absorption spectrum of water vapor comprises thousands of absorption lines with intensities that cover many orders of magnitude. The characterization of the water vapor absorption spectrum is very difficult. Numerous measurement campaigns and theoretical works have been dedicated to this problem in the recent decade [e.g. *Partridge and Schwenke*, 1997; *Flaud et al.*, 1997; *Carleer et al.*, 1999; *Coheur et al.*, 2002]. The improvement of the knowledge of the water vapor spectroscopy and the updating of spectral databases such as HITRAN [*Rothman et al.*, 1998, 2003] is an ongoing process.

Accurate knowledge of the absorption spectrum is required for monitoring atmospheric water vapor using remote sensing techniques [*Maurellis et al.*, 2003]. Atmospheric water vapor is monitored using observations of satellite-borne sensors that measure the attenuation of reflected sunlight in the visible and the near infrared. The water vapor column is derived from such observations by sensors like the MODerate Resolution Imaging Spectroradiometer (MODIS), the Global Ozone Monitoring Experiment (GOME), the SCanning Imaging Absorption spectroMeter for Atmospheric CHartographY (SCIAMACHY), and GOME-2 to be launched in 2005 [*Kaufman and Gao*, 1992; *Maurellis et al.*, 2000; *Lang et al.*, 2002]. The radiative transfer simulations used for the retrieval of the water vapor abundance from the measured light intensities are based on the water vapor absorption spectroscopy. Accurate spectroscopic data are therefore a precondition for quantitative remote sensing of atmospheric water vapor. The work presented in this part of the thesis is dedicated to the validation and testing of water vapor spectroscopic data. An overview of the strategy used is given in section 1.4.

1.2 Water vapor absorption spectrum

In this section the water vapor absorption spectrum is introduced and the complexity of the spectrum is explained briefly. Atoms and molecules in the gas phase in general have distinct states with distinct energy levels. A transition from one state to another is associated with the emission or absorption of a photon with the frequency $\tilde{\nu}$ that is related to the energy difference ΔE between the two states by

$$\Delta E = h\tilde{\nu}, \tag{1.1}$$

where h is the Planck constant. The narrow absorption features in the spectrum of light that has passed a volume with a gaseous absorber are called absorption lines. These lines are centered at frequencies defined by the energy levels of the possible energetic states of the molecule via Eq. (1.1). Instead of the frequency $\tilde{\nu}$ we use the wavenumber $\nu = \tilde{\nu}/c$ (the inverse of the wavelength λ) with the units cm^{-1}; c is the speed of light in vacuum.

In order to understand the complexity of the water vapor absorption spectrum it is necessary to consider the structure of the water molecule. The water molecule is a tri-atomic bent molecule consisting of two hydrogen atoms that are bound to one oxygen atom with an angle of 104.5° between the O–H bonds. The molecule has three degrees of vibrational and rotational freedom. The energy differences between rotational states labeled with the rotational quantum number J are small. Light in the infrared region efficiently excites the rotational energy levels due to the permanent dipole moment of the molecule. Purely

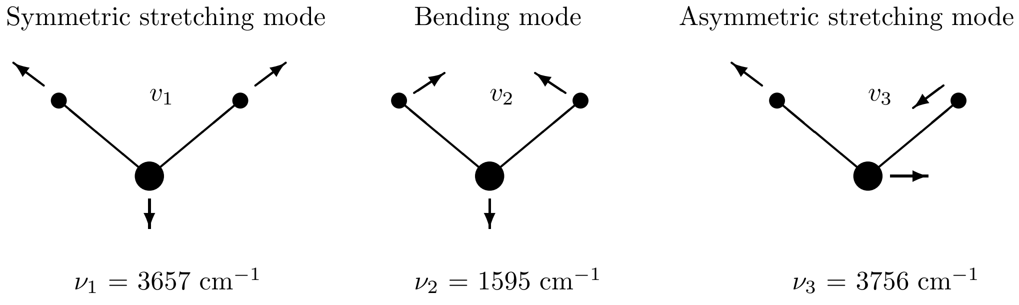

Figure 1.1: Modes of the vibrational excitation of the water molecule. Small dots depict hydrogen atoms, big dots represent oxygen atoms.

rotational transitions are responsible for absorption lines in the infrared at wavelengths $\lambda > 1$ μm.

The water molecule can vibrate in three distinct modes (Fig. 1.1). The vibrationally excited states in the symmetric and the antisymmetric stretch modes are labeled with the quantum numbers v_1 and v_3 respectively. These modes involve stretching of the O–H bonds. The vibrationally excited states in the bending mode are labeled with the quantum number v_2. This mode is related to a change of the angle between the bonds. The absorption lines of transitions from the ground state to the lowest lying excited states in the three modes are located in the near infrared at the wavenumbers ν_1 = 3657 cm^{-1}, ν_2 = 1595 cm^{-1}, and ν_3 = 3756 cm^{-1}.

Vibrational transitions with $\Delta v > 1$ are related to absorption lines at shorter wavelengths in the near infrared, the visible and the ultraviolet. Vibrational transitions are usually accompanied by rotational transitions. The plethora of possible combinations of vibrational and rotational transitions is responsible for the large number of absorption lines. The rotational-vibrational absorption lines are grouped in absorption bands. There are two reasons for this: Firstly, the energy differences between vibrational states are much larger than the energy differences between rotational states. Secondly, the energy difference between states in the vibrational stretch modes are similar and about double as large as the energy difference between states in the vibrational bending mode. The absorption bands are referred to as polyads with the labels ν and δ. The polyad label is related to the change of the vibrational quantum number of the stretch modes and the bending mode. The $4\nu + \delta$ polyad, for example, comprises transitions with $\Delta v_1 + \Delta v_3 = 4$ and $\Delta v_2 = 1$, transitions with $\Delta v_1 + \Delta v_3 = 3$ and $\Delta v_2 = 3$, as well as other combinations of transitions with a similar energy. The δ indicates an odd Δv_2. An absorption band or polyad typically comprises several hundreds of lines that are grouped in a certain wavelength region (Table 1.1). The absorption bands with polyad numbers below 3ν overlap. Absorption bands are

Table 1.1: Spectral region and maximum line intensities of water vapor absorption bands labeled with polyad numbers.

polyad	ν (cm^{-1})	λ (nm)	S (cm/molec)
3ν	9,700–11,000	900–1030	10^{-22}
$3\nu + \delta$	11,600–12,800	780–860	10^{-23}
4ν	13,500–15,000	690–740	10^{-23}
$4\nu + \delta$	15,150–15,900	630–660	10^{-24}
5ν	16,550–17,100	585–605	10^{-24}
$\vdots$			

not well separated for wavelengths $\lambda > 1$ μm. In general, the intensity of absorption lines decreases with increasing value of Δv between the upper and the lower state. That is why the intensity of the absorption bands decreases with increasing polyad number. The atmospheric absorption in weak absorption bands with polyad numbers up to 4ν are relevant for atmospheric absorption of solar light due to the high water vapor abundance in the Earth's atmosphere. Polyads with the numbers up to 5ν are used for atmospheric remote sensing. Absorption bands with higher polyad numbers are known but are so weak that they are considered irrelevant for both radiative transfer and remote sensing in the Earth atmosphere.

The water vapor absorption spectrum is extremely complex. The permanent dipole moment of the water molecule is responsible for the strong coupling of the molecular state with the external radiation field and therefore for the high intensities of many absorption lines. The water molecule has many degrees of freedom of rotation and vibration due to its bent structure. The energy of a rotational state depends on the vibrational state of the molecule and vice versa. This can be understood intuitively using the classically picture of centrifugal and Coriolis forces. The rotational movement is complicated by the fact that the water molecule is an asymmetric top. Altogether, the water molecule has a very pronounced non-linear character. An exact description requires a full quantum mechanical description of both the electronic as well as the nuclear motions. Currently, no complete theoretical model exists that accurately describes the high resolution spectrum of water vapor [*Polyansky et al.*, 2003].

The water molecule can also be electronically excited. Since the electronically excited states are predissociative the corresponding absorption lines are blurred. The related absorption features are located in the ultraviolet where other gases dominate the atmospheric absorption. These absorption features play therefore a minor role for the radiative transfer in the Earth atmosphere and are irrelevant for retrieval purposes.

1.3 Line parameters

In this section the spectroscopic parameters are introduced that are used in the following chapters. The definitions of spectroscopic parameters used here are consistent with the definitions used by *Rothman et al.* [1998].

The probability that a photon with a given frequency will be absorbed by a molecule is expressed in terms of the monochromatic absorption cross section $\sigma_{\eta\eta'}(\nu)$ with the units cm^2/molec. We use the absorption cross section as a function of the wavenumber ν with the units cm^{-1}. Absorption lines are narrow maxima of the molecular absorption cross section that are related to specific molecular transitions.

The line intensity is equivalent to the probability that a molecular transition is induced by the absorption of a photon. This line intensity can be given in various forms with different units [for an educative review see *Hilborn*, 1982]. We use the line intensity $S_{\eta\eta'}$ for a transition between the upper and the lower state η' and η

$$S_{\eta\eta'} = \frac{h\nu_{\eta\eta'}}{c} \frac{n_\eta}{\sum_{\tilde{\eta}} n_{\tilde{\eta}}} \left(1 - \frac{g_\eta n_{\eta'}}{g_{\eta'} n_\eta}\right) B_{\eta\eta'} \tag{1.2}$$

that depends on the populations of the upper and lower states $n_{\eta'}$ and n_η, the statistical weights $g_{\eta'}$ and g_η, the line position $\nu_{\eta\eta'}$, and the Einstein B coefficient $B_{\eta\eta'}$ of induced absorption. The troposphere, which contains the largest part of the atmospheric water vapor, is in local thermodynamic equilibrium. The temperature dependence of the populations are therefore described by the Boltzmann distribution

$$n_\eta = g_\eta \exp(-c_2 E_\eta / T) \frac{\sum_{\tilde{\eta}} n_{\tilde{\eta}}}{\sum_{\tilde{\eta}} g_{\tilde{\eta}} \exp(-c_2 E_{\tilde{\eta}} / T)}, \tag{1.3}$$

where T is the temperature, E_η is the energy of a state η with the units cm^{-1}, and $c_2 = hc/k$ is the second radiation constant $c_2 = 1.4388$ cm K; k is the Boltzmann constant. Using the partition sum $Q(T) = \sum_\eta g_\eta \exp(-c_2 E_\eta / T)$ we can express the line intensity $S_{\eta\eta'}$ as function of the temperature

$$S_{\eta\eta'}(T) = S_{\eta\eta'}(T_{\mathrm{ref}}) \frac{Q(T_{\mathrm{ref}})}{Q(T)} \frac{\exp(-c_2 E_\eta / T)}{\exp(-c_2 E_\eta / T_{\mathrm{ref}})} \frac{[1 - \exp(-c_2 \nu_{\eta\eta'} / T)]}{[1 - \exp(-c_2 \nu_{\eta\eta'} / T_{\mathrm{ref}})]}. \tag{1.4}$$

The line intensity is usually given relative to a line intensity value $S_{\eta\eta'}(T_{\mathrm{ref}})$ at the reference temperature $T_{\mathrm{ref}} = 296$ K. The line intensity $S_{\eta\eta'}$ is the molecular absorption cross section $\sigma_{\eta\eta'}(\nu)$ of one specific absorption line integrated over all wavenumbers ν. The line intensity $S_{\eta\eta'}$ has therefore the unit cm/molec.

Molecular transitions can be associated with the absorption or emission of a photon with a wavenumber ν that deviates from the wavenumber defined by Eq. (1.1). Absorption lines are thus not infinitely narrow. Lines are broadened by a number of mechanisms that have been comprehensively reviewed by *Allard and Kiehlkopf* [1982]. In the following the most important broadening mechanisms are discussed.

Pressure broadening is due to inter-molecular collisions. For isolated molecules, absorbed or emitted photons are wave trains with a defined phase relation. The frequency of absorbed or emitted photons is well defined up to an uncertainty that is inversely proportional to the length of the wave train. Random molecular collisions perturb this phase relation. These collisions occur at any time with the same probability. As a consequence, the length of the segments with a defined phase relation is Poisson distributed. According to the Fourier-transformation the spectrum of this perturbed wave train has a Lorentzian shape and is described by the line shape function

$$f_{\mathrm{L}}(\nu - \nu_{\eta\eta'}) = \frac{1}{\pi} \frac{\gamma_{\mathrm{L}}}{\gamma_{\mathrm{L}}^2 + (\nu - \nu_{\eta\eta'})^2}. \tag{1.5}$$

The line shape function is a spectral distribution function with the units cm (the inverse of the spectral unit cm^{-1}). The width γ_{L} is proportional to the pressure. That is why this broadening mechanism is called pressure broadening. During molecular collisions, the collision partners exert electrical forces on each other. The perturbation of the phase relation can therefore occur during a finite period of time. This reduces the length of the segments with an undisturbed phase relation and broadens the spectrum of the wave train. The line broadening is enhanced significantly especially for molecules with a pronounced dipole moment. The water molecule has, in contrast to N_2 and O_2, the two major components of dry air, a strong dipole moment. Therefore, one distinguishes between the self-broadening due to collisions of two water molecules and the air-broadening (or foreign-broadening) due to collision of water molecules with molecules of the surrounding air. For the pressure broadening of water vapor lines, the width γ_{L} is the sum of the broadening parameters γ_{air} and γ_{self}

$$\gamma_{\mathrm{L}} = (T_{\mathrm{ref}}/T)^a((p - p_w)\gamma_{\mathrm{air}} + p_w\gamma_{\mathrm{self}}) \tag{1.6}$$

weighted with the partial pressures of the surrounding dry air $(p-p_w)$ and the water vapor p_w. The exponent a is a line specific parameter that controls the temperature dependence of γ_{L}. Self-broadening parameters for water are about five times as large as air-broadening parameters.

Temperature broadening is related to the Doppler-shift of the frequency of the light due to the Brownian motion of the molecules. For an ensemble of molecules with translational velocities that are distributed according to the Maxwell-Boltzmann-distribution, one obtains the line shape function

$$f_{\mathrm{D}}(\nu - \nu_{\eta\eta'}) = \frac{1}{\gamma_{\mathrm{D}}\sqrt{\pi}}\, e^{-\left(\frac{\nu - \nu_{\eta\eta'}}{\gamma_{\mathrm{D}}}\right)^2}. \tag{1.7}$$

The Doppler-line width

$$\gamma_{\mathrm{D}} = \nu_{\eta\eta'}\sqrt{2kT/mc^2} \tag{1.8}$$

depends on the temperature T and the molecular mass m.

Light absorption by water vapor takes place mainly in the lower atmosphere, where pressure broadening is more important than temperature broadening. We take both broadening contributions into account by using the Voigt line shape, i.e. the convolution of the both line shape functions

$$f_{\mathrm{Voigt}}(\nu - \nu_{\eta\eta'}) = \int_{-\infty}^{-\infty} f_{\mathrm{L}}(\bar{\nu} - \nu_{\eta\eta'}) f_{\mathrm{D}}(\nu - \bar{\nu}) d\bar{\nu} \tag{1.9}$$

The line shape functions are normalized such that $\int_{-\infty}^{\infty} f(\nu)d\nu = 1$. The monochromatic molecular absorption cross section $\sigma_{\eta\eta'}$ of one particular transition is

$$\sigma_{\eta\eta'}(\nu, p, T) = S_{\eta\eta'}(T) f(\nu - \nu_{\eta\eta'}, p, T) \tag{1.10}$$

with the units cm^2/molec. The monochromatic molecular absorption cross section $\sigma(\nu - \nu_{\eta\eta'}, p, T)$ of water is the sum of the cross sections $\sigma_{\eta\eta'}$ of all transitions.

The internal energy levels can be influenced during the collision by the electric field of the collision partner. Due to their permanent dipole moment, water molecules can form dimers. The formation of dimers influences the internal molecular energy levels and thus the absorption characteristics. The net effect is that the line shape function is enhanced in the wings far away from the center frequency $\nu_{\eta\eta'}$. There is also the far wing contribution of all lines that adds up to the so-called water vapor continuum. The water vapor continuum is responsible for the strong atmospheric absorption in the wavenumber region from 200 cm^{-1} to 1200 cm^{-1}. In the near infrared and the visible, the continuum absorption is weak as compared to the line absorption. It can be described using sophisticated continuum models [e.g. *Clough et al.*, 1989; *Ma and Tipping*, 2002].

The absorption cross section is used for the calculation of the optical thickness τ of a medium with the molecular density ρ along a given path s

$$\tau(\nu) = \int \sum_{\eta\eta'} \sigma_{\eta\eta'}(\nu, p(s), T(s)) \rho(s) ds \tag{1.11}$$

The optical thickness τ relates the intensities of the incident and the transmitted light I_0 and I_{tr} if no internal sources are present

$$\frac{I_{\mathrm{tr}}}{I_0} = e^{-\tau}. \tag{1.12}$$

This equation, well-known as Beer-Lambert's Law, is the basis of the radiative transfer simulations used in the following chapters.

1.4 Outlook

In this work, spectroscopic line parameters in the visible and in the near infrared will be validated under atmospheric conditions by comparing ground-based high resolution observations of the direct solar radiation with simulated spectra. The spectral resolution of the measurement is high enough that individual lines are resolved. The simulation includes radiative transfer calculations in the Earth atmosphere as well as the simulation of the instrument response. A methodology is established for estimating how much information the ground-based measurement adds to the line parameters (Chapter 2). We take into account the *a priori* accuracy of the line parameters, the instrument noise, and the atmospheric profile data of temperature, pressure, and composition including the related uncertainties. This methodology is applied to the validation of water vapor spectroscopy data for the 720 nm absorption band given in a database published by *Coheur et al.* [2002] and in the 2001 release of HITRAN [*Rothman et al.*, 2003]. Requirements for the accuracy of atmospheric profile data are derived. Line parameter errors are identified from the residual, i.e. the difference between measured and simulated spectrum. These results are confirmed by a comparison with independent high-accuracy data. We determine how accurately the atmospheric profile should be known in order to permit the validation and the improvement on the spectroscopy. In Chapter 3 the overall quality of a number of spectral databases is compared regarding the spectroscopic data in the absorption band close to 600 nm (5ν polyad). The amplitude of line intensity errors is derived from the residuals for lines that show little blending. The impact of line intensity errors on satellite observations with moderate spectral resolution (0.2 nm) is derived. Both absorption bands at the wavelengths 720 nm and 600 nm are used for the retrieval of water vapor from such satellite observations. The absorption band close to 600 nm is especially interesting for this purpose due to the absence of saturation effects.

Bibliography

Allard, N. and J. Kiehlkopf, The effect of neutral nonresonant collisions on atomic spectral lines, *Rev. Modern Phys., 54*, 4, 1103–1182, 1982.

Bernath, P. F., The spectroscopy of water vapor: Experiment, theory and applications, *Phys. Chem. Chem. Phys., 4*, 1501–1509, 2002.

Carleer, M., A. Jenouvrier, A. C. Vandaele, P. F. Bernath, M. F. Merienne, R. Colin, N. F. Zobov, O. L. Polyansky, J. Tennyson, and V. A. Savin, The near infrared, visible and near ultraviolet overtone spectrum of water, *J. Chem. Phys.*, *111*, 2444–2450, 1999.

Clough, S. A., F. X. Kneizys, and R. W. Davies, Line shape and the water vapor continuum, *Atmos. Res., 23*, 229–241, 1989.

Coheur, P.-F., S. Fally, M. Carleer, C. Clerbaux, R. Colin, A. Jenouvrier, M.-F. Mérienne, C. Hermans, and A. C. Vandaele, New water vapor line parameters in the 26000-13000 cm^{-1} region, *J. Quant. Spectrosc. Radiat. Transfer, 74*, 493–510, 2002.

Flaud, J.-M., C. Camy-Peyret, A. Bykov, O. Naumenko, T. Petrova, A. Scherbakov, and L. Sinitsa, The High-Resolution Spectrum of Water Vapor between 11 600 and 12 750 cm^{-1}, *J. Molec. Spectrosc., 183*, 300–309, 1997.

Hilborn, R. C., Einstein coefficients, cross sections, f-values, dipole moments and all that, *Am. J. Phys., 50*, 982–986, 1982.

Kaufman, Y. J., and B. C. Gao, Remote sensing of water vapor in the near IR from EOS/MODIS, *IEEE TRANS. Geosci. Remote Sensing, 30*, 871–884, 1992.

Kiehl, J. T., and K. E. Trenberth, Earth's annual mean global energy budget, *Bull. Am. Meteorol. Soc., 78*, 197–208, 1997.

Lang, R., A. N. Maurellis, W. J. van der Zande, I. Aben, J. Landgraf, and W. Ubachs, Forward modelling and retrieval of water vapor from GOME: Treatment of narrow band absorption spectra, *J. Geophys. Res., 107*, doi:10.1029/2001JD001453, 2002.

Lenoble, J., *Atmospheric Radiative Transfer*, Deepak, Hampton, 1993.

Ma, Q., and R. H. Tipping, The averaged density matrix in the coordinate representation: Application to the calculation of the far-wing line shape for H_2O, *JCP, 111* , 5909–5921, 1999.

Maurellis, A. N., R. Lang, W. J. Van der Zande, I. Aben, and W. Ubachs, Precipitable Water Column Retrieval from GOME Data, *Geophys. Res. Lett., 27*, 903–906, 2000.

Maurellis, A. N., R. Lang, J. E. Williams, W. J. van der Zande, K. Smith, D. A. Newnham, J. Tennyson and R. N. Tolchenov, The Impact of New Water Vapor Spectroscopy on Satellite Retrievals, Proceedings of the NATO Advanced Research Workshop "Weakly Interacting Molecular Pairs: Unconventional Absorbers of Radiation in the Atmosphere", eds. C. Camy-Peyret, A. Vigasin, 259–272, 2003.

Naus, H., W. Ubachs, P. F. Levelt, O. L. Polyansky, N. F. Zobov, and J. Tennyson, Cavity-Ring-Down Spectroscopy on Water Vapor in the Range 555-604 nm, *J. Molec. Spectrosc., 205*, 117–121, 2001.

Partridge, H., and D. W. Schwenke, The determination of an accurate isotope dependent potential energy surface for water from extensive ab initio calculations and experimental data, *J. Chem. Phys.*, *106*, 4618–4639, 1997.

Penner, S. S., *Quantitative Molecular Spectroscopy and Gas Emissivities*, Addison-Wesley, Reading, MA, 1959.

Platt, U., Modern Methods of the measurement of atmospheric trace gases, *Phys. Chem. Chem. Phys., 1*, 5409–5415, 1999.

Polyansky, O. L., A. G. Császár, S. V. Shirin, N. F. Zobov, P. Barletta, J. Tennyson, D. W. Schwenke, P. J. Knowles, High-accuracy ab initio rotation-vibration transitions for water, *Science., 299*, 539–542, 2003.

Ramanathan, V. and A. M.Vogelmann, Greenhouse effect, atmospheric solar absorption and the earth's radiation budget: From the Arrhenius/Langley era to the 1990s, *Ambio, 26*, 38–46, 1997.

Roedel, W., *Physik unserer Umwelt: Die Atmosphäre*, Springer Verlag, Berlin, 1992.

Rothman et al., The HITRAN molecular spectroscopic database and HAWKS (HITRAN Atmospheric Workstation) 1996 edition, *J. Quant. Spectrosc. Radiat. Transfer, 60*, 665–710, 1998.

Rothman et al., The HITRAN molecular spectroscopic database: edition of 2000 including updates through 2001, *J. Quant. Spectrosc. Radiat. Transfer, 82*, 5–44, 2003.

Schermaul, R., R. C. M. Learner, D. A. Newnham, R. G. Williams, J. Ballard, N. F. Zobov, D. Belmiloud, and J. Tennyson, The water vapor spectrum in the region 8600–15,000 cm^{-1}: Experimental and theoretical studies for a new spectral line database. I.

laboratory measurements, *J. Mol. Spectrosc., 208*, 32–42, 2001.

Smith, K. M., D. A. Nenwham, and R. G. Williams, Collision induced absorption of solar radiation in the atmsophere by molecular oxygen at 1.2 μm: field observations and model calculations, *J. Geophys. Res., 106*, 7541–7552, 2001

Chapter 2

Capabilities of ground-based solar occultation measurements in the validation of line spectroscopy: water vapor - a case study

Abstract

Water vapor spectroscopy data for the 720 nm absorption band (4ν polyad) given in the ULB-UFR-BIRA database and in HITRAN-2000 are validated under atmospheric conditions. For this purpose, ground-based high resolution observations of the direct solar radiation are compared with simulated spectra. The information content of the measured spectrum about the spectroscopic parameters is quantified on a line specific basis taking into account instrument noise and uncertainties in the atmospheric water vapor profile. This allows an automated selection of line parameters that can be validated using the ground-based measurement. The results of the validation are confirmed using independent high-accuracy data. Furthermore, we derive that water vapor profiles needs to be known to an accuracy of better than 5% in total column or better than 10% at each profile point if errors on the order of 10% or worse in the line parameters are to be discerned from the solar measurements.

2.1 Introduction

An accurate determination of the radiative effects of atmospheric trace gases and their retrieval from routinely-monitoring satellite instruments is needed as an important input for climate and chemical models. The spectroscopic data used in radiative transfer models are therefore a fundamentally important source of information which should be validated, i.e. characterized to a sufficiently high accuracy, in order to minimize the effect of its uncertainty on any model which uses it. Water vapor is an atmospheric trace gas with a significant impact on the global radiation balance and is routinely monitored from satellites. The considerable radiative forcing properties of atmospheric water vapor are well-documented [cf. *Kiehl and Trenberth* , 1997] and are not discussed any further here. A series of satellite instruments exists that uses reflected sunlight in the visible and near infrared to infer water vapor column amounts. The series includes instruments like GOME (Global Ozone Monitoring Experiment) on the ERS-2 satellite, SCIAMACHY (SCanning Imaging Absorption spectroMeter for Atmospheric CHartographY) on EN-

VISAT and GOME-2 on the MetOp satellite to be launched in 2005. The water vapor abundance is retrieved from water vapor absorption signatures in the visible [*Lang et al.*, 2002; *Maurellis et al.*, 2000] and in the infrared [*Noël et al.*, 1999; *Casadio et al.*, 2000; *Wagner et al.*, 2003]. It has been shown that the water vapor column retrievals are strongly dependent on the accuracy of the spectroscopic parameters [*Maurellis et al.*, 2003]. The very complex absorption spectrum of water is perhaps an extreme test for the validation of spectroscopic data of the kind discussed here. We focus in this study on spectroscopic line parameters taken from spectroscopic databases such as HITRAN-2000 [*Rothman et al.*, 2003] and a database released by *Coheur et al.* [2002] referred to as ULB-UFR-BIRA in the following, which has been used to update the recently-released HITRAN-2004 database.

The construction of spectroscopic databases containing line parameters is difficult. The data is usually taken from a variety of experimental sources. This is true especially in the case of water vapor which has line intensities covering many orders of magnitude [*Tolchenov et al.*, 2003]. Long-path absorption cell experiments are required for the weak lines and short-path cells are required for the strong lines. *A priori* data taken from existing databases and from theory are used for the retrieval of line parameters from measured absorption spectra [*Schermaul et al.*, 2001]. Theoretical data is required as well for the line assignment [*Polyansky et al.*, 1998] which is necessary for the determination of the temperature-dependence of line intensities [e.g. *Lenoble et al.*, 1993]. Spectroscopic data in the visible and the near infrared are usually less accurate than at longer wavelengths [*Polyansky et al.*, 2003]. The characterization of water lines in the visible and the near infrared is experimentally more challenging because the line intensities in this part of the spectrum are on average weaker than in the thermal and far infrared. Furthermore, theoretical models used in assigning the lines at the shorter wavelengths are generally less accurate than at longer wavelengths [*Polyansky et al.*, 2003]. The characterization of water vapor spectroscopy using long-path absorption cell experiments can be complicated by condensation inside the absorption cell and by difficulties in determining the absorption path length with sufficient accuracy to name but two of many possible sources of error [*Coheur et al.*, 2002]. The spectroscopic data relevant to atmospheric radiative transfer simulations thus come from a variety of experimental sources and may have different accuracies due to the different experimental setups and the different techniques for line fitting and line matching involved. The accuracy of line parameter typically lies in a range from 1% to 100%. It is vital that models which use these spectroscopic databases are capable of correctly reproducing the radiative effects of the species involved under atmospheric conditions. It is therefore essential to validate these spectroscopic data in the context of atmospheric radiative transfer calculations on real measurements.

It has been shown in a number of past studies that spectroscopic data can be verified in general terms using ground-based observations of direct solar radiation under cloud-free conditions. For water vapor this has been done by *Smith and Newnham* [2001], *Veihelmann et al.* [2002], *Sierk et al.* [2003], *Coheur et al.* [2003] and *Albert et al.* [2004] for a number of bands between 10,000 and 20,000 cm^{-1}. In these studies, ground-based Fourier transform and grating spectrometer measurements are compared with radiative transfer simulations based on the spectroscopic database to be evaluated. The approach thus far has generally been to identify overall scaling problems of band-integrated intensities or to make broad statements about the overall quality of the database under study. What makes our approach here more general is that a full characterization of instrument and trace gas profile uncertainties is used to make specific statements about individual line parameters.

As a case study we evaluate spectroscopic data for the 720 nm absorption band (4ν polyad). The data are taken from two sources: HITRAN-2000 and ULB-UFR-BIRA (section 2.5). These are relevant both for water vapor retrievals from satellite observations and for radiative transfer models [cf. *Bennartz and Lohmann*, 2001; *Smith et al.*, 2004]. The reference spectrum is derived from ground-based Fourier Transform Radiometer (FTR) measurements of direct sunlight. This measurement has been made using a Fourier transform spectrometer with a resolution high enough to resolve individual lines (0.05 cm^{-1}) [*Smith et al.*, 2001]. The measurement and the atmospheric data used for the simulation are discussed in section 2.2.

Our approach is first to estimate accuracy requirements regarding the atmospheric profile information that have to be met for a validation of line intensity parameters S and the air-broadening parameters γ_{air} (section 2.3). For this purpose, the sensitivity of the simulated spectrum with respect to the atmospheric profile data for pressure temperature and water vapor is compared with the sensitivity with respect to the line parameters S and γ_{air}. The sensitivities are determined based on a linearization of the forward model. The next step is to consider that the measurement does not add any information to line parameters known with a precision better than a certain threshold accuracy. We derive an estimate for this threshold as a function of the line intensity, the instrument noise, the atmospheric water vapor abundance and its related uncertainty (section 2.4). The information content of the ground-based measurement with respect to the line parameters S and γ_{air} that could be retrieved from the measured spectrum in an ideal retrieval is then compared with the accuracy of spectroscopic data given in ULB-UFR-BIRA and with differences in line parameters between ULB-UFR-BIRA and HITRAN-2000. From this comparison we derive which line parameters can be validated with the ground-based measurement and the atmospheric data available.

For these lines, errors in the line parameter are detected from the residuals, i.e. the difference between simulated and measured spectra. We specify the error type when the shape of the residuals allows the distinction between errors in the line intensity, the line width, and the line position (section 2.5). The identification of line intensity parameter errors is validated using as reference an independent measurement dedicated to the characterization of weak lines with an exceptionally high signal-to-noise ratio [*Schermaul et al.*, 2002].

2.2 Experiment and Model

In this study we evaluate spectroscopic data from HITRAN-2000 [*Rothman et al.*, 2003] and the ULB-UFR-BIRA databases [*Coheur et al.*, 2002], much of which form the input for the 2004 release of HITRAN. The 2001 update of HITRAN does not affect the water vapor spectroscopy in this wavelength region and is not considered separately. The water vapor spectroscopy data given in HITRAN 2000 for the wavelength region studied here originally comes from laboratory measurements by *Mandin et al.* [1986]. The ULB-UFR-BIRA databases contains line positions, integrated intensities and broadening parameters for more than 9000 lines in the region from 13000 cm^{-1} to 26000 cm^{-1}. In the spectral region studied here, ranging from 13500 cm^{-1} to 14300 cm^{-1}, the database contains about 850 weak lines that are absent in HITRAN-2000.

The field measurement has been made using a Bomem DA3.002 Fourier transform spectrometer that was located at 51.6°N, 1.3°W at an altitude of 135 m above the sea-level. The instrumental setup [*Smith et al.*, 2001] has been used in a series of measurement campaigns that have been conducted over the last 5 years. The instrument is equipped with a telescope with a round field of view pointing at the sun. The radius of the disc viewed by the instrument is about a fifth of the radius of the total solar disc. Multiple scattering can be neglected in this observation geometry. According to a formula derived by *Box and Deepak* [1979], the apparent optical depth differs from the true optical depth by less than 0.003%. The radiation reaching the instrument can thus be simulated by simply applying Beer-Lambert's law, assuming that the atmospheric state is known. The instrument was operated at a maximum unapodized spectral resolution of 0.05 cm^{-1}. Individual lines are resolved in the observed spectra. Appropriate optical band-pass filters are used. The atmospheric spectra used in this study have not been published elsewhere.

A solar spectrum is used for the simulation of the measured spectra that is derived from high resolution measurements made using the McMath-Pierce Telescope at the National Solar Observatory (NSO) on the Kitt Peak, Arizona, USA on 2100 m above sea level. This spectrum has been corrected for atmospheric absorption by water vapor above the telescope [*Wallace et al.*, 1996] using a Langley-plot technique. In spectral regions with strong absorption by water vapor the extrapolation to zero air-mass is unstable and the solar spectrum is not given. This is the case close to lines with intensities larger than 10^{-24} cm/molec. In order to exclude errors due to Fraunhofer lines, we also discard spectral regions where the corrected solar spectrum has an intensity of less than 0.95 times the background intensity. Weak solar lines are not masked out.

The atmosphere is modeled at 25 homogeneous layers with a thickness of 1 km. Atmospheric extinction is accounted for by molecular absorption as well as by Rayleigh scattering. Extinction by aerosol scattering is neglected since this spectrally very broad effect is compensated by the baseline fit discussed below. We include molecular line absorption by water vapor and O_2. According to HITRAN, these are the only species with absorption lines in the spectral region considered. As mentioned earlier, the absorption by water vapor is simulated based on the spectroscopic data given in either of HITRAN-2000 and ULB-UFR-BIRA. The profiles of the molecular abundance as well as pressure and temperature are interpolated over the slant path defined by the line-of-sight of the measurement. The interpolation is based on data from the European Center for Medium-range Weather Forecast (ECMWF) for the nearest four ECMWF-grid points, and on data from a radiosonde measurement at the weather station Larkhill which is 48 km south of the measurement site. According to these data, the atmosphere at 0,1,2 and 3 km altitude (with the pressures of 1020, 909, 806 and 710 hPa) has a temperature of 286, 281, 275 and 272 K and a water vapor density of 1.2 $\times 10^4$, 8.0 $\times 10^3$, 5.3 $\times 10^3$ and 2.3 $\times 10^3$ ppmV. The uncertainty of the water vapor abundance thus obtained is between 10% and 30% according to the source of these data. A comparison of simulated and measured spectra strongly suggests that the true water vapor column density is significantly lower than the a-priori data. Thus an improved estimate for the water vapor abundance is required for the validation of spectroscopic data. To this end, we retrieve the water vapor column from the measured spectra using a non-linear, least squares fitting routine which minimizes the norm of the residuals independently for eight adjacent 100 cm^{-1}-broad spectral regions of one measurement. The columns obtained from these independent retrievals agree well with each other (with a standard deviation of about 4% of the mean values) but differ from the initial data, by approximately 30%. An improved water vapor profile is hence derived by scaling the original ECMWF data combined with radiosonde measurements by the optimized column value. The fitting of the water vapor column compensates for any scaling of the global level of line intensities within the band. As a consequence, line intensity errors derived from the residuals have to be regarded as relative to the overall level of line intensities.

The water vapor continuum is the net far-wing contribution of all absorption lines to the absorption. This continuum can be included in the calculation of the spectral molecular absorption cross section by using a continuum model of *Ma and Tipping* [2002]. The difference between the molecular cross section based on this continuum model and a simulation using a conventional calculation based on Voigt line shape representations is on the order of 10^{-28} cm^2/molec. The largest relative differences are found between line positions with values of 0.5% percent of the cross section.

Instrument effects can be accounted for by convolving the simulated spectra at the bottom of the atmosphere with the instrumental line shape function. We assume a sinc-function, which is the instrumental line shape function of an ideal instrument with a finite optical path difference. We convolve both the measured as well as the simulated spectra with a Norton Beer strong apodization function [*Norton and Beer*, 1976]. This reduces the 'ringing', i.e. the side lobes of lines that appear in the measured spectrum due to the finite optical path difference of the instrument. This facilitates the interpretation of the spectra and the residuals. The unknown instrument gain as well as broad-band absorption contributions that are not modeled are accounted for by a multiplicative baseline that is fitted to the measurement. This baseline is represented by a third order polynomial function of the wavenumber. The coefficients are determined using a non-linear least square fit routine by minimizing the norm of the residuals. The baseline fit is done simultaneously with the water vapor column fit discussed above for 100 cm^{-1} broad spectral regions.

We note that the solar spectrum, the simulated transmission spectrum and the measured spectrum are shifted slightly relative to each other. The measured solar spectrum is in general shifted with respect to the true solar spectrum by two effects. The Doppler-shift caused by the relative motion of the instrument and the sun is 1.35 cm^{-1}. The spectral shift due to the refractive index of the air surrounding the instrument is on the order of -3.8 cm^{-1}. Furthermore, spectral shifts may be introduced by errors in the spectral calibration of the instrument. In order to correct for the spectral shifts, the measured spectrum is shifted such that measured and simulated water vapor line positions match. Then the solar spectrum is shifted such that the Fraunhofer line positions in the measured spectrum and the solar spectrum match.

2.3 Sensitivity analysis

The validation of spectroscopic data, being based on an analysis of the residuals, is limited by uncertainties in the measurement and the simulated spectrum. In this section, the relative importance of the uncertainties of the atmospheric data used in the simulation is estimated and accuracy requirements are derived. More specifically, we determine here the sensitivity of the simulated spectrum with respect to the atmospheric profile data for pressure, temperature and the water vapor abundance. The amplitudes of these sensitivities are interpreted using as a reference the sensitivity of the spectrum with respect to the line intensity and the air-broadening parameters S and γ_{air}. The sensitivities are determined using error propagation calculations that are based on the Jacobian matrix $\mathbf{K}$ of the linearized forward model

$$(\mathbf{I}-\mathbf{I}_0) = \mathbf{K}(\mathbf{x}-\mathbf{x}_0) \quad \text{with} \qquad K_{ij} = \frac{\partial I_i}{\partial x_j}. \tag{2.1}$$

The vector $\mathbf{I}$ denotes the discrete intensity spectrum, while the vector $\mathbf{x}$ represents any of the input vectors, i.e. either a discrete representation of one of the atmospheric profiles, or one of the line parameters for the series of lines considered. The intensity spectrum $\mathbf{I}_0$ and the parameters $\mathbf{x}_0$ denote the reference state of the Taylor-expansion, defined by the conditions of the ground-based measurement. The matrix $\mathbf{K}$ relates the error covariance matrix $\mathbf{C}_{\mathrm{x}}$ of the vector $\mathbf{x}$ with the error covariance matrix $\mathbf{C}_{\mathbf{I}}$ of the simulated discrete intensity spectrum $\mathbf{I}$ by the matrix product

$$\mathbf{C}_{\mathbf{I}} = \mathbf{K}\ \mathbf{C}_{\mathrm{x}}\ \mathbf{K}^{\mathbf{T}}. \tag{2.2}$$

The superscript T denotes the matrix transpose. The diagonal elements of an error covariance matrix are the variances, while the off-diagonal elements are the cross-correlation coefficients. For the sake of clarity, we show only the standard deviation of the measured intensities σ_I, i.e. the square root of the diagonal elements of $\mathbf{C}_{\mathbf{I}}$.

The sensitivity analysis of the simulated spectrum is shown for a 10 cm^{-1} wide window that contains two very strong absorption lines ($S = 3 \times 10^{-23}\,\mathrm{cm/molec}$) that are saturated at the line center as well as weaker lines that show no saturation (Fig. 2.1). The simulated absorption spectrum is depicted in the upper left graph (a). The envelope of the spectrum, i.e. the spectrally smooth background, is normalized to unity. The sensitivity of the spectrum with respect to uncertainties in the line intensities $\sigma_{I,S}$ (solid) and the broadening parameters $\sigma_{I,\gamma}$ (dashed) are shown as function of the wavenumber (b). We chose a relative uncertainty (standard deviation divided by mean value) in all the lines of 10% for both line parameters. This is a realistic estimate for strong lines. The relative

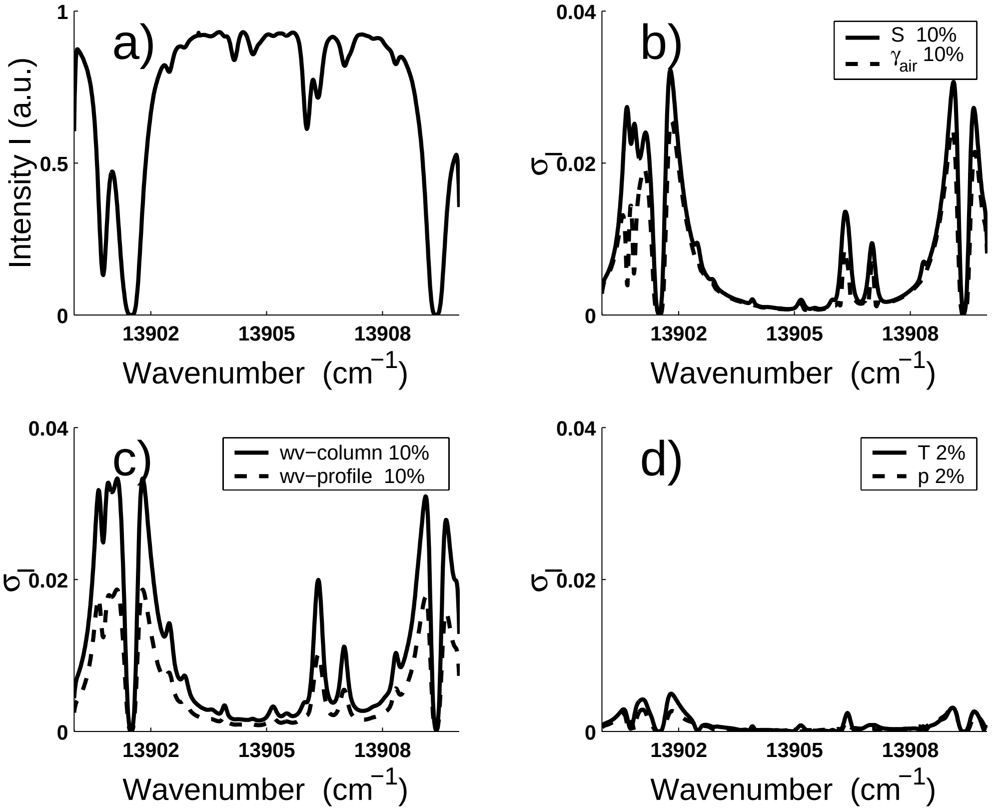

Figure 2.1: The simulated intensity spectrum I (a) and its sensitivity σ_I with respect to various parameters (b, c, d). The amplitudes of the sensitivities with respect to line parameter errors (b) and with respect to errors in the atmospheric water vapor data (c) are comparable. We consider errors of 10% in the line intensity (b, solid) and air broadening (b, dashed) parameters, the water vapor column (c, solid) and the water vapor profile (c, dashed). The sensitivities with respect to errors of 2% in the atmospheric pressure (d, dashed) and temperature data (d, solid) have a lower amplitude.

uncertainty of the line parameters of weak lines can be much larger. The sensitivity $\sigma_{I,S}$ peaks at the line centers of unsaturated lines. For saturated lines the behavior is a bit different: at the rising edges of the saturated lines $\sigma_{I,S}$ reaches a maximum and decreases to a minimum at the line center. We note that, according to Beer-Lambert's Law, the sensitivity of the simulated spectrum with respect to the line intensity is largest where the optical thickness equals unity. The error signature of line broadening parameters $\sigma_{I,\gamma}$

usually has distinct contributions at the line center and in the line wings. This is hardly visible due to the blending of lines. The amplitude of $\sigma_{I,\gamma}$ is about 20% less than the amplitude of $\sigma_{I,S}$ (at line centers).

The intensity error of the simulated spectrum due to uncertainties in atmospheric pressure $\sigma_{I,p}$ (dashed) and temperature data $\sigma_{I,T}$ (solid) are plotted in the lower right graph (d). For the error calculations we chose a relative error of 2% for both the pressure and the temperature values in each height level of the vertical profile representation. This is an estimate for the error of temperature and pressure profiles used. We chose the errors of the different height levels to be statistically-independent. In summary, we note that the magnitudes of the intensity errors $\sigma_{I,p}$ and $\sigma_{I,T}$ are almost an order of magnitude smaller than the sensitivity of the simulated spectrum with respect to the line parameters $\sigma_{I,S}$ and $\sigma_{I,\gamma}$. We conclude that the uncertainty of commonly-available pressure and temperature data is usually sufficient for the validation of line parameters. The intensity errors due to pressure and temperature errors become significant compared to the impact of the line parameters only for errors in the former that are larger than 5% (not shown).

The intensity error of the simulated spectrum due to uncertainties in atmospheric water vapor abundance are plotted in the lower left graph (c). The impact of a profile error σ_{I,w_p} is depicted as a dashed line. For each sub-column, we assume a relative error of 10% of the molecular density that is statistically-independent of the errors of the other sub-columns. This error magnitude is an estimate for the uncertainty of the atmospheric water vapor data used. Profile errors of this magnitude and larger are common to atmospheric water vapor data of many sources including radiosonde measurements. The impact of an error of 10% in the total integrated column density σ_{I,w_c} is shown as a solid line. Column errors of this magnitude are common to ECMWF data. In reality, variations of the column are accompanied by variations of the profile shape. We show the pure column error for demonstrative purposes only. The standard deviation σ_{I,w_c} represents the amplitude of intensity errors both due to statistical as well as due to systematic column errors.

The intensity error of the simulated spectrum due to errors of the water vapor abundance naturally has large values close to the center of unsaturated lines. The signatures of column errors and profile errors have a very similar shape. This is due to the fact that 80% of the total column density is present in the lowest two sub-columns, where similar pressure and temperature conditions cause the shape of the absorption lines to be similar. The ratio of the amplitudes of $\sigma_{I,w_p}/\sigma_{I,w_c}$ depends on the water vapor profile used and the number of subcolumns with statistically-independent errors. For the water vapor profile used in this study this ratio is about 0.56.

The standard deviation σ_{I,w_c} related to a water vapor column error is similar to the standard deviation $\sigma_{I,S}$ related to line intensity errors with the same relative error amplitude. This is generally true because both the column and the line intensity appear as a product in Beer-Lambert's Law. We conclude that the water vapor column has to be known with a relative error of less than 10% for the validation of line intensity parameters that are known with a 10% accuracy. This corresponds to an uncorrelated profile error of about 18%. A comparison of the required accuracy of pressure, temperature, and water vapor data with the accuracy of commonly available atmospheric data indicates that the limiting factor of the validation of line parameters is the accuracy of the water vapor data.

2.4 Accuracy limits and line intensity

The validation of the line parameters using a ground-based FTR spectrum is mainly limited by the uncertainty of the atmospheric water vapor abundance and by instrument noise. In this section the importance of these limitations is quantified as a function of the line intensity. We determine how much information the ground-based measurement can add to the line parameters S and γ_{air} of each individual line. To this end, we determine the sensitivities of the line parameters $\tilde{\sigma}_S$ and $\tilde{\sigma}_{\gamma\mathrm{air}}$ to instrument noise and to uncertainties in the atmospheric water vapor data. These sensitivities are determined using an error propagation technique known from inversion theory: We consider the accuracy of line parameters that could be retrieved from the measured spectrum in an ideal retrieval. Note that we do not perform a real retrieval of line parameters. The sensitivities $\tilde{\sigma}_S$ and $\tilde{\sigma}_{\gamma\mathrm{air}}$ are used to decide, whether the validation of a line parameter that is known *a-priori* with a given accuracy is possible. We consider the ground-based measurement to be a significant test also for line parameters for which the difference of values given in different databases is larger than the related sensitivity.

The sensitivities $\tilde{\sigma}_S$ and $\tilde{\sigma}_{\gamma\mathrm{air}}$ are determined as follows: The error covariance matrix of the line parameters $\mathbf{C}_{\mathrm{p}}$ is derived from the covariance matrix of the measurement $\mathbf{C_I}$ using

$$\mathbf{C}_{\mathrm{p}} = (\mathbf{K}_{\mathrm{p}}^{\mathbf{T}}\mathbf{C_I^{-1}}\mathbf{K}_{\mathrm{p}})^{\mathbf{-1}}. \tag{2.3}$$

The Jacobian matrix $\mathbf{K}_{\mathrm{p}}$ is taken from the linearized forward model [e.g. *Rodgers*, 2000]. The error covariance matrix $\mathbf{C_I}$ represents alternatively the instrument noise or the uncertainty of the simulated spectrum due to errors of the water vapor abundance (see section 2.3). The errors of line intensity and air-broadening parameters are treated together in one combined error covariance matrix $\mathbf{C}_{\mathrm{p}}$ which contains both variance as well as covariance terms. The cross-correlation of errors in S and γ_{air} for each line are thus taken into account. If n lines are considered, the variances of the line parameters S and γ_{air} are the diagonal elements

$$\tilde{\sigma}_S^2(i) = \mathbf{C_p}(i,i) \quad \text{and} \quad \tilde{\sigma}_{\gamma\mathrm{air}}^2(i) = \mathbf{C_p}(n+i, n+i) \tag{2.4}$$

of the matrix $\mathbf{C_p}$ with the dimensions $(2n \times 2n)$.

The relative importance of the limitations of the validation due to instrument noise and due to uncertainties in the atmospheric water vapor profile is investigated as a function of the line intensity S. In Figure 2.2 the sensitivities of the line parameters S (upper graph) and γ_{air} (lower graph) are depicted as relative errors $\tilde{\sigma}_S/S$ and $\tilde{\sigma}_{\gamma\mathrm{air}}/\gamma_{\mathrm{air}}$. The instrument noise is assumed to be constant for the spectral region considered with an amplitude of 0.001 times the baseline intensity of the spectrum. A water vapor profile error of 10% is assumed, which corresponds to a column error of about 5.6%. The relative errors of the line parameters due to instrument noise (dots) show a decreasing trend with

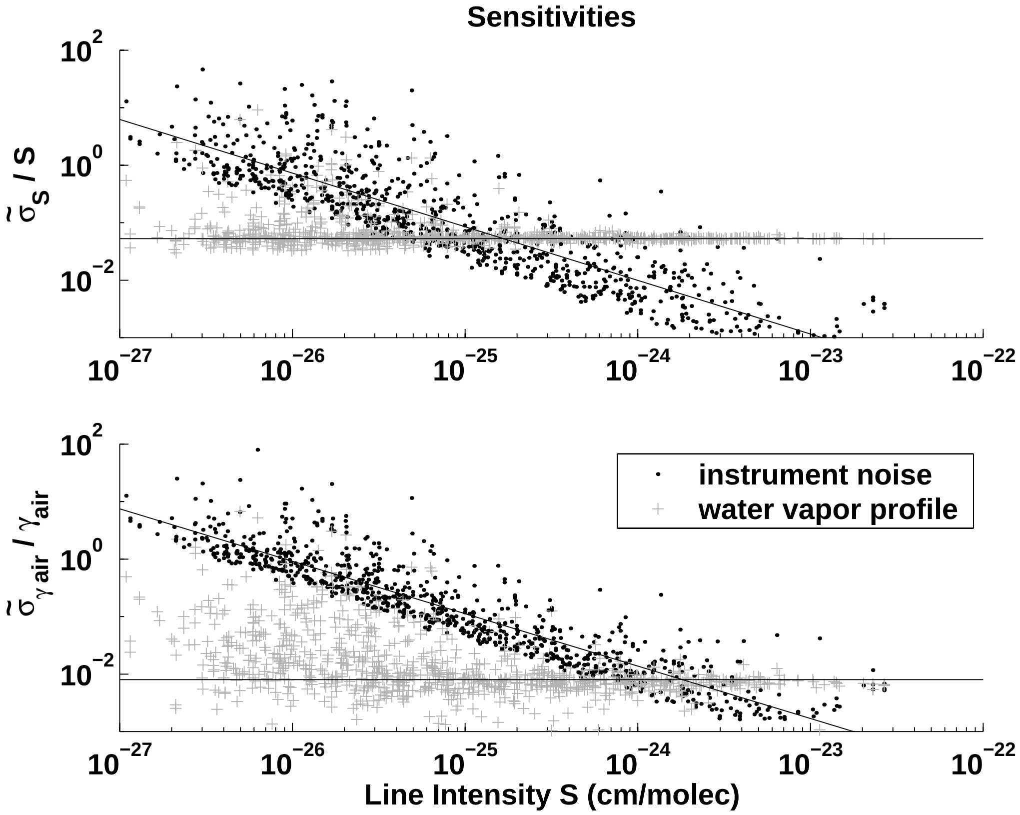

Figure 2.2: The sensitivities of line intensities S (upper graph) and air broadening parameters γ_{air} (lower graph) to instrument noise and to the water vapor profile are shown as relative errors $\tilde{\sigma}_S/S$ and $\tilde{\sigma}_{\gamma\text{air}}/\gamma_{\text{air}}$. Errors due to instrument noise with a signal-to-noise ratio of 1000 are shown as dots (clustered around the slanted line), errors due to an uncertainty of the water vapor profile of 10% are shown as gray crosses (clustered around the horizontal line).

increasing line intensity. This behavior is sketched with the slant line determined from a linear regression made on double-logarithmic scales. The relative errors due to the water vapor profile errors (gray crosses clustered around horizontal line) are largely independent of the line intensities. The large spread of the errors is due to the blending of lines, which can cause large and strongly-correlated errors of line parameters.

For lines with an intensity lower than a threshold intensity $S_{\text{thr}} \approx 2 \times 10^{-25}$ cm/molec the validation of line intensity parameters is mainly limited by noise. For stronger lines it is mainly limited by uncertainties in the water vapor profile (horizontal line). The validation of air-broadening parameters is mainly limited by instrumental noise for lines with an intensity up to $S_{\mathrm{thr}} \approx 2 \times 10^{-24}\,\mathrm{cm/molec}$ (lower plot in Fig. 2.2).

An empirical formula is derived for estimating the limitations of the validation due to instrument noise and uncertainties of the water vapor profile. Based on the fitted lines (in Figure 2.2) we obtain a formula relating $\tilde{\sigma}_S/S$ to the line intensity

$$\frac{\tilde{\sigma}_S}{S} = \begin{cases} 10^{-26.2} \cdot S^{-0.94} & : \quad S < 2 \times 10^{-25}\,\mathrm{cm/molec} \\ 0.053 & : \quad S \geq 2 \times 10^{-25}\,\mathrm{cm/molec} \end{cases} \tag{2.5}$$

This formula is derived from a case with a signal-to-noise ratio of $\xi = 1000$ and a water vapor column $w_c = 5.8 \times 10^{22}\,\mathrm{molec/cm^2}$ with a relative uncertainty $\sigma_{w_c}/w_c = 0.056$. The relative error $\tilde{\sigma}_S/S$ due to noise is inversely proportional to the signal-to-noise ratio ξ and inversely proportional to the integrated water vapor column w_c given in $\mathrm{molec/cm^2}$. The relative error $\tilde{\sigma}_S/S$ due to uncertainties in the water vapor information scales with the relative error of the total water vapor column σ_{w_c}/w_c. Hence, we generalize Eq. 2.5 to the approximation

$$\tilde{\sigma}_S \approx \begin{cases} 0.36 \cdot \frac{1}{\xi w_c} & : \quad S < 2 \times 10^{-25}\,\mathrm{cm/molec} \\ 0.95 \cdot S\frac{\sigma_{w_c}}{w_c} & : \quad S \geq 2 \times 10^{-25}\,\mathrm{cm/molec.} \end{cases} \tag{2.6}$$

For the air broadening parameter we obtain a similar empirical relation

$$\tilde{\sigma}_{\gamma_{\mathrm{air}}} \approx \begin{cases} 0.36 \cdot \frac{1}{\xi w_c} & : \quad S < 2 \times 10^{-24}\,\mathrm{cm/molec} \\ 0.14 \cdot S\frac{\sigma_{w_c}}{w_c} & : \quad S \geq 2 \times 10^{-24}\,\mathrm{cm/molec} \end{cases} \tag{2.7}$$

With these relations a first order estimate for the sensitivities $\tilde{\sigma}_S$ and $\tilde{\sigma}_{\gamma_{\mathrm{air}}}$ as functions of the line intensity can be inferred for experimental conditions that deviate from the conditions of the measurement presented here.

The accuracies of line parameters given in the ULB-UFR-BIRA database for the spectral region from $13500\,\mathrm{cm^{-1}}$ to $14300\,\mathrm{cm^{-1}}$ are depicted as relative errors σ_S/S (upper graph) and $\sigma_{\gamma\mathrm{air}}/\gamma_{\mathrm{air}}$ (lower graph) in Figure 2.3. These accuracies are compared with the sensitivity of line parameters $\tilde{\sigma}_S$ and $\tilde{\sigma}_{\gamma\mathrm{air}}$ to instrument noise and the atmospheric water vapor profile. The trends of the relative errors $\tilde{\sigma}_S/S$ and $\tilde{\sigma}_{\gamma\mathrm{air}}/\gamma_{\mathrm{air}}$ are depicted as the solid lines. This comparison indicates that the ground-based measurement adds information about the line intensity parameters of about 10% of the lines (black dots upper graph). The validation of air broadening parameters of about 50% of the lines (black dots lower graph) is possible. The accuracies of line parameters that cannot be validated are denoted by gray dots. In passing we note that the accuracies of the intensity data from ULB-UFR-BIRA very closely follow the trend that is sketched by the solid lines. This indicates that the limitations of the laboratory experiment used for the creation of the database are of a similar nature as the limitations that we are facing in the evaluation of the ground-based FTR measurement.

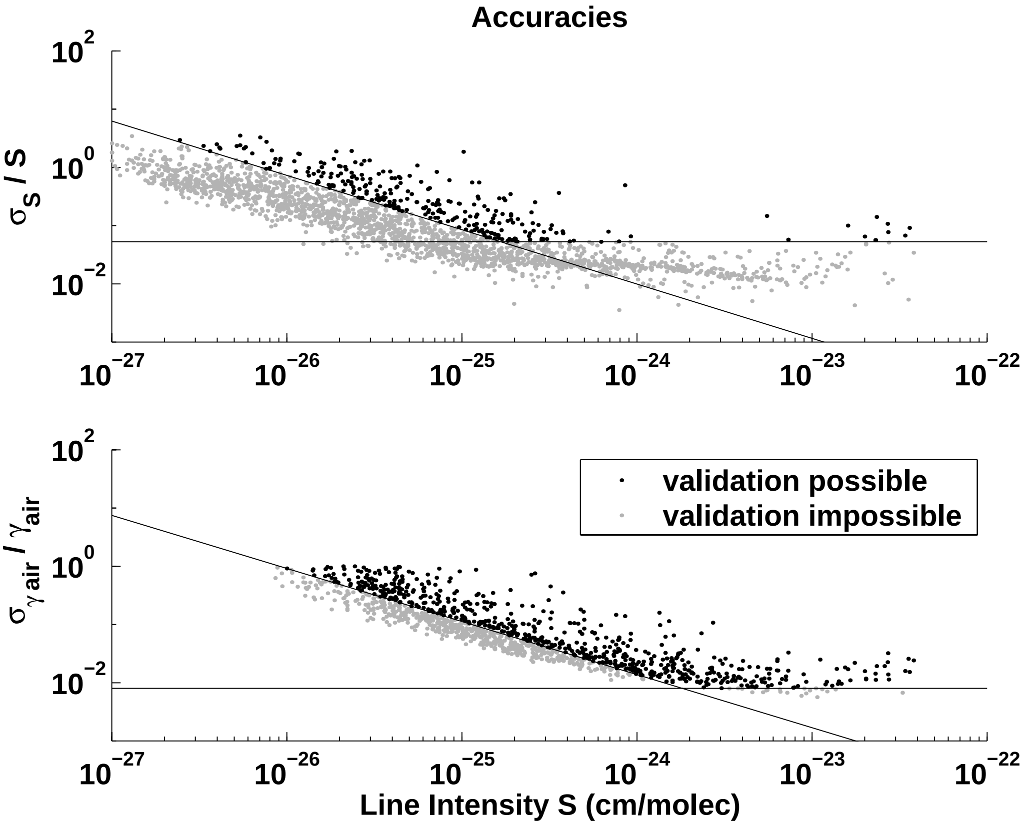

Figure 2.3: Accuracy of line parameters given in the ULB-UFR-BIRA database for the spectral region from 13500 cm^{-1} to 14300 cm^{-1}. The accuracies are shown as relative errors σ_S/S (upper graph) and $\sigma_{\gamma\mathrm{air}}/\gamma_{\mathrm{air}}$ (lower graph). The line parameters that can be validated using the ground-based measurement are shown as black dots. Line parameters shown in gray cannot be validated with the current measurement uncertainties. The solid lines are the same as the ones shown in Fig. 2.2.

In Fig. 2.4 the differences between line parameters given in HITRAN-2000 and the ULB-UFR-BIRA database are shown for the spectral region from 13500 cm^{-1} to 14300 cm^{-1}. The differences are compared to the sensitivity of line parameters $\tilde{\sigma}_S$ and $\tilde{\sigma}_{\gamma\mathrm{air}}$ to instrument noise and the atmospheric water vapor profile. The relative differences in the line intensity S (upper plot) and the air broadening parameters γ_{air} (lower plot) are smaller than the relative errors $\tilde{\sigma}_S/S$ and $\tilde{\sigma}_{\gamma\mathrm{air}}/\gamma_{\mathrm{air}}$ for about 50% of the lines (gray dots). For about 50% of the lines the measurement is thus a significant test (black dots).

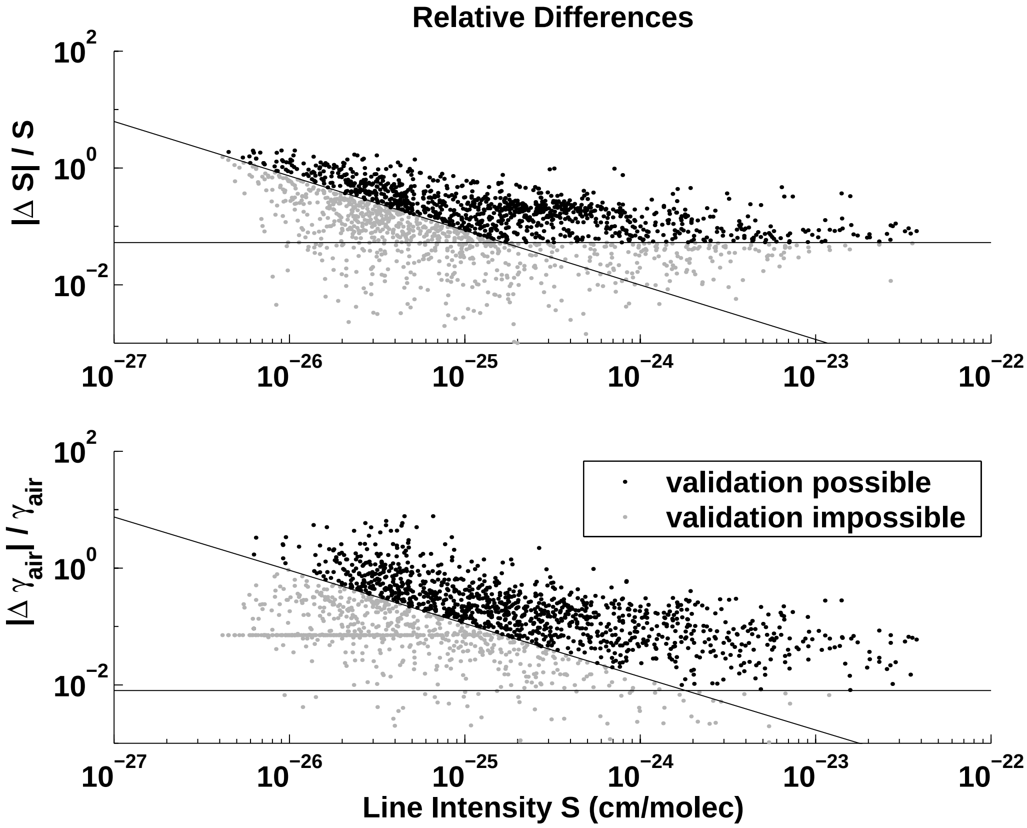

Figure 2.4: The amplitude of relative differences of line parameters $|S_{\mathrm{hit01}} - S_{\mathrm{ulb04}}|/S_{\mathrm{ulb04}}$ (upper graph) and $|\gamma_{\mathrm{air,hit01}} - \gamma_{\mathrm{air,ulb04}}|/\gamma_{\mathrm{air,ulb04}}$ (lower graph) given in HITRAN-2000 and ULB-UFR-BIRA. Line parameter differences that exceed the uncertainty of the ground-based measurement are shown as black dots. The other line parameter differences are shown gray. The solid lines are the same as in Fig. 2.2.

We conclude that the ground-based measurement can add information to about 10% of the line intensity parameters of a state-of-the-art spectroscopic database. These are mostly weak lines with a line intensity lower than 5×10^{-25} cm/molec. The air-broadening parameters of as much as 50% of the lines can be validated. This includes both strong as well as weak lines. For about half of the line parameters it is possible to decide which database of HITRAN-2000 and ULB-UFR-BIRA provides a value that is more consistent with the atmospheric measurement.

2.5 Interpretation of the residuals

The spectroscopic data for the 720 nm band given in HITRAN-2000 and the ULB-UFR-BIRA database are evaluated based on details of the residuals, i.e. the difference between the simulated and measured spectra (Figures 2.5 and 2.6). For the validation of line parameters, lines are selected according to the limitations derived in the previous section. With this we exclude line parameters that are sensitive to errors of the atmospheric water vapor profile derived in Section 2.2. The intensity of the solar spectrum used in this study is not available close to water vapor absorption lines with intensities larger than $S = 10^{-24}$ cm/molec (see section 2.2). This poses an upper limit to the intensity of lines that we validate. Furthermore, we mask out spectral regions where the solar spectrum has a normalized intensity of less than 0.95. With this we exclude errors that are related to Fraunhofer lines (black box). For ULB-UFR-BIRA, we only consider lines where all line parameters are given. With this selection we obtain 786 lines between 13500 cm^{-1} and 14300 cm^{-1} for which we evaluate the residuals. For HITRAN-2000 we include lines lacking a pressure shift parameter, which is missing for all lines in the spectral region studied. The result is that 830 lines are selected in the same spectral range.

Line parameter errors are identified from the amplitude of the residual close to the center of selected lines. The differences between the measurement and the simulation are regarded as significant when the residual exceeds a certain level of uncertainty of the simulated and the measured spectrum. In order to increase the significance of the error detection, we chose a rather high threshold amplitude of the residuals, i.e. the error corresponding to a 20% water vapor column error (gray area). The instrument noise with a signal-to-noise ratio of 1000 is shown as a light gray area.

The residuals of both ULB-UFR-BIRA (dashed) and HITRAN 2000 (solid) show signatures of typical line parameter errors (e.g. at 13571.1 cm^{-1} and 13572.1 cm^{-1}) as well as signatures that we cannot assign to any line parameter error (e.g. at 13570.5 cm^{-1}). These signatures may be due to instrument effects. The solar spectrum used is another possible error source. Unknown weak lines may also contribute to the residuals. In Table 2 (see Appendix) we list 129 corresponding pairs of lines of the two databases where at least one line is flagged as erroneous. 82 lines of ULB-UFR-BIRA and 100 lines of HITRAN-2000 are flagged. The wavenumber, the line intensity S, and the air-broadening parameter γ_{air} of lines are listed together with an error key indicating the type of error. We distinguish line width errors (w), line intensity errors (i) and line position errors (p). Combined errors of the three error types are marked with a 'c', unclassified signatures in the residuals with a significant amplitude are marked with an 'x', and lines with no error signature are marked with a '+'. We observe that many line intensity errors in HITRAN-2000 have been improved in ULB-UFR-BIRA. Nevertheless, we recognize characteristic error signatures in both databases. This number of error flagged lines is too low to reflect the relative quality of the databases with statistical significance. According to the root mean square values of the residuals the ULB-UFR-BIRA (0.0105) database is slightly better than HITRAN (0.0122) in the spectral region from 13500 cm-1 to 14300 cm-1.

The results of the classification of line intensity parameters are compared with in-

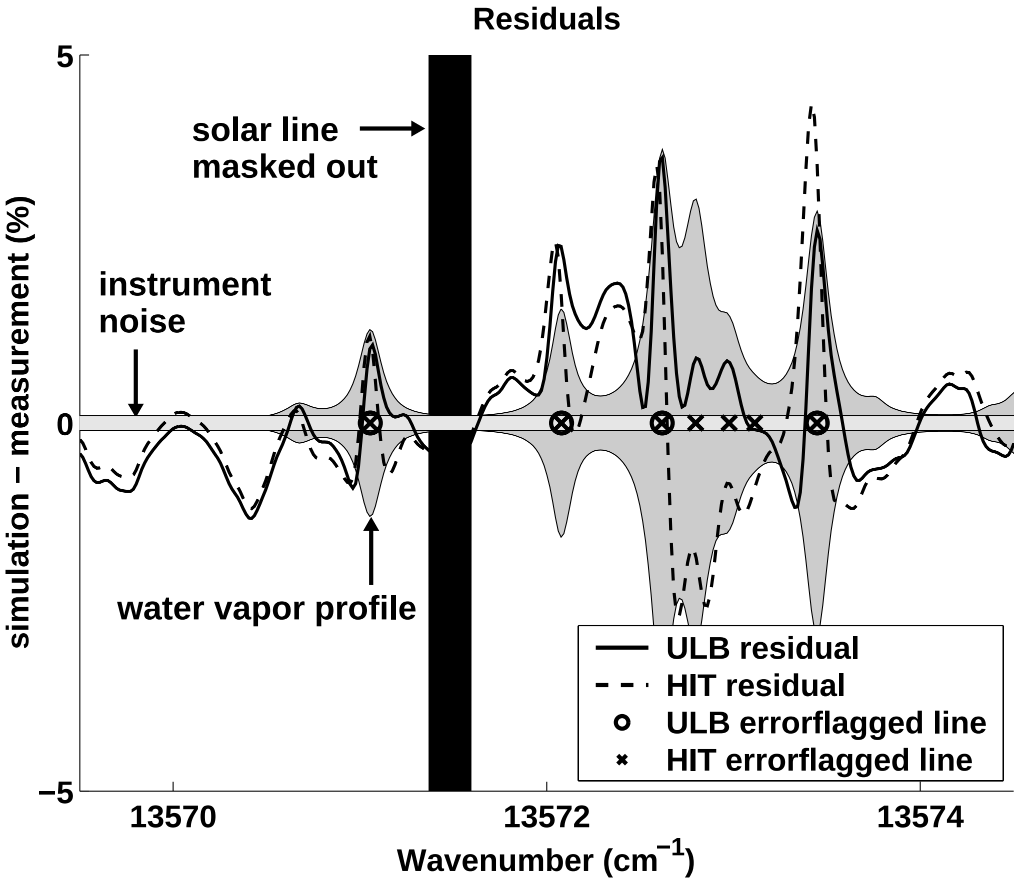

Figure 2.5: Residuals, i.e. differences between measured spectra and simulations based on ULB-UFR-BIRA (solid) and HITRAN-2000 (dashed). Errorflagged lines are marked with a circle (ULB) and a cross (HITRAN-2000). The intensity error due to instrument noise (signal-to-noise ratio 1000, light gray) and due to an uncertainty of a 20% water vapor column error (dark gray) are depicted as 1-σ-environment. Spectral regions that may be affected by errors related to the solar spectrum are masked out (black).

dependent high-accuracy data. *Schermaul et al.* [2002] have measured the line intensity parameters of water vapor in the wavelength region 13200 cm^{-1} to 15000 cm^{-1} using a long-path absorption cell in combination with a FTR. This measurement is dedicated to the characterization of weak lines with an intensity $S \leq 6 \times 10^{-24}$ cm/molec and has an exceptionally high signal-to-noise ratio (3600 as compared to usually 1200). These data do

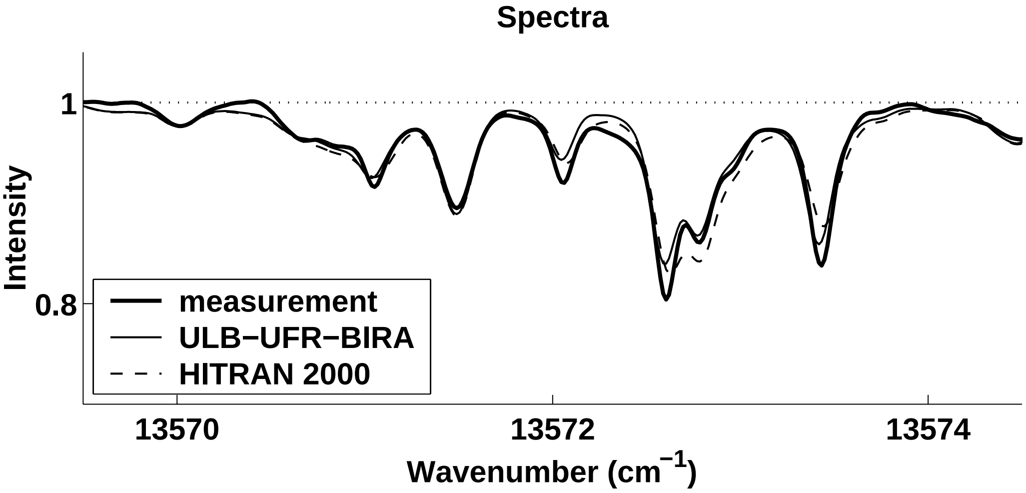

Figure 2.6: Measured spectrum (thick solid) and simulations based on ULB-UFR-BIRA (solid) and HITRAN-2000 (dashed). The background is normalized to unity.

not comprise the line parameters of the strong lines. That is why we do not perform radiative transfer simulations based on these data in the same way as we do for HITRAN-2000 and ULB-UFR-BIRA database. The line positions and intensity parameters are included in the Table 2. The error identification and classification for lines given in HITRAN-2000 and in the ULB-UFR-BIRA database is confirmed in 74% of the cases when a corresponding line occurs in the data given by *Schermaul et al.* [2002].

Accurate derivation of water vapor absorption line parameters from experimental data is in general difficult. For the retrieval of line parameters from laboratory data, advanced and flexible retrieval software is required that allows taking into account various *a-priori* data [cf. *Tolchenov et al.*, 2003, and references therein]. The retrieval of line parameters from the atmospheric measurement is more challenging than the retrieval from laboratory measurement due to the larger uncertainties of the atmospheric conditions. In a validation study for the water vapor absorption band close to 600 nm (Chapter 3), the sign and the amplitude of line intensity errors is derived for lines that show little blending assuming a correct line width. In the spectral region close to 720 nm studied in here, lines in ground-based atmospheric spectra are mostly blended. Furthermore, many of the error signatures of the lines listed in Table 2 indicate a combination of line intensity, line width, and line position errors. Therefore, we decided not to derive an improved list of line parameters. The list of error-flagged line parameters provides an input for future evaluations of long-path absorption cell experiments or theoretical studies.

2.6 Conclusions

We validate spectroscopic data for the water vapor band close to 720 nm given in HITRAN-2000 and the ULB-UFR-BIRA database. Atmospheric profile data from ECMWF and a nearby radiosonde measurement are used for radiative transfer simulations. A ground-based Fourier transform spectrometer measurement was used to obtain the measured spectra. We have performed a full characterization of the inherent uncertainties in the measurement situation on a line specific basis. This includes the trace gas density profile information used for the simulation and the contamination of the measurement by instrument noise.

We have estimated the minimum accuracy of the atmospheric data required for the validation of the line intensity and the air broadening parameters. Assuming that the line parameters are given with an *a priori* accuracy of 10%, we have determined that the atmospheric data for pressure and temperature have to be known with a relative accuracy of better than a few percent. This requirement is usually met for data from atmospheric data assimilation models such as ECMWF. The water vapor profile has to be known with errors lower than 5% of the integrated column density. For a sub-column profile with a 1 km height resolution this corresponds to statistically-independent errors of 10% in each sub-column. The water vapor profile data, however, are often given with a lower accuracy, especially in the case of assimilated model data such as ECMWF. It is thus essential that accurate, colocated radiosonde or lidar observations are made in order to make a conclusive validation of the spectroscopic parameters S and γ_{air} using ground-based observations.

We have shown that the atmospheric validation of line intensity parameters is mainly limited by instrument noise for lines with intensities lower than a threshold intensity $S_{\mathrm{thr}} = 2 \times 10^{-25}$ cm/molec. For lines with larger intensities, the validation is limited by the atmospheric water vapor profile. Assuming an accuracy of about 5% in the water vapor column, line intensities with uncertainties larger than 5% can be validated. The validation of air broadening parameters is limited by instrument noise for lines with intensities lower than $S_{\mathrm{thr}} = 2 \times 10^{-24}$ cm/molec. For lines with larger intensities, air broadening parameters with uncertainties larger than about 1% can be validated. These limitations have been quantified for the intensity and the air broadening parameters in terms of threshold accuracies $\tilde{\sigma}_S$ and $\tilde{\sigma}_{\gamma\mathrm{air}}$. A line parameter that is known *a priori* with an accuracy better than this threshold cannot be validated. We provide simple, empirical functions (for example, eq. 2.6 and 2.7) that relate these threshold accuracies to the line intensity, the signal-to-noise ratio of the measurement, the integrated gas column and the relative accuracy to which it has been measured.

We conclude that ground-based measurement together with accurate atmospheric data can improve the information about line parameters given in spectroscopic databases. For the measurement condition of the case study presented, about 10% of the line intensity parameters and about 50% of the air broadening parameters of lines in the 720 nm band given in the ULB-UFR-BIRA database can be validated.

The spectroscopic data for the 720 nm band given in HITRAN-2000 and the ULB-UFR-BIRA database are evaluated. Lines are selected for the validation based on the limitations mentioned above. We indicate errors in the line parameters of lines with intensities $S \leq 10^{-24}$ cm/molec. The results are confirmed based on independent data from an experiment that is dedicated to the characterization of weak lines. The results of the validation study presented here therefore provide a useful input for future evaluations of laboratory or theoretical data for the improvement of the water vapor spectroscopy and already have facilitated line list compilations used as inputs for HITRAN-2004.

Bibliography

Albert, P., K. M. Smith, R. Bennartz, D. A. Newnham, and J. Fischer, Satellite- and ground-based observations of atmospheric water vapor absorption in the 940 nm region *J. Quant. Spectrosc. Radiat. Transfer, 84*, 181–193, 2004.

Bennartz, R. and U. Lohmann, Impact of improved near infrared water vapor line data on absorption of solar radiation , *Geophys. Res. Lett., 28*, 4591-4594, 2001.

Box, M. A., and A. Deepak, Atmospheric corrections to solar radiometry, *Appl. Opt., 12*, 1941–1949, 1979.

Casadio, S., C. Zehner, G. Piscane, and E. Putz, Empirical Retrieval of Atmospheric Air Mass Factor (ERA) for the Measurement of Water Vapor Vertical Content using GOME Data, *Geophys. Res. Lett., 27,* 1483-1486, 2000.

Coheur, P.-F., S. Fally, M. Carleer, C. Clerbaux, R. Colin, A. Jenouvrier, M.-F. Mérienne, C. Hermans and A. C. Vandaele, New water vapor line parameters in the 26000-13000 cm^{-1} region, *J. Quant. Spectrosc. Radiat. Transfer, 74*, 493–510, 2002.

Coheur, P.-F., C. Clerbaux, M. Carleer, S. Fally, D. Hurtmans, R. Colin, C. Hermans, A. C. Vandaele, B. Barret, M. de Maziere and H. De Backer, Retrieval of atmospheric water vapor columns from FT visible solar absorption spectra and evaluation of spectroscopic databases, *J. Quant. Spectrosc. Radiat. Transfer, 82*, 133–150, 2003.

Kiehl, J. T. and K. E. Trenberth, Earth's Annual Mean Global Energy Budget, *Bull. Amer. Met. Soc., 78*, 197–208, 1997.

Lang, R., A. N. Maurellis, W. J. van der Zande, I. Aben, J. Landgraf, and W. Ubachs, Forward modelling and retrieval of water vapor from GOME: Treatment of narrow band absorption spectra, *JGR, 107*, 10.1029/2001JD001453 , 2002.

Lenoble, J., *Atmospheric Radiative Transfer*, Deepak, Hampton, 1993.

Ma, Q., and R. H. Tipping, The averaged density matrix in the coordinate representation: Application to the calculation of the far-wing line shape for H_2O, *JCP, 111* , 5909–5921, 1999.

Mandin, J. Y., J. P. Chevillard, C. Camy-Peyret, J. Flaud, J. W. Brault, The High-Resolution Spectrum of Water Vapor Between 13,200 and 16,500 cm^{-1}, *J. Mol. Spectr., 116*, 167–190, 1986.

Maurellis, A. N., R. Lang, W. J. Van der Zande, I. Aben, and W. Ubachs, Precipitable Water Column Retrieval from GOME Data, *Geophys. Res. Lett., 27*, 903–906, 2000.

Maurellis, A. N., R. Lang, J. E. Williams, W. J. van der Zande, K. Smith, D. A. Newnham, J. Tennyson and R. N. Tolchenov, The Impact of New Water Vapor Spectroscopy on Satellite Retrievals, Proceedings of the NATO Advanced Research Workshop "Weakly Interacting Molecular Pairs: Unconventional Absorbers of Radiation in the Atmosphere", eds. C. Camy-Peyret, A. Vigasin, 259–272, 2003.

Maurellis, A. N., and J. Tennyson, The climatic effects of water vapor, *Physics World*, May, 2003.

Mérienne, M.-F., A. Jenouvrier, C. Hermans, A. C. Vandaele, M. Carleer, C. Clerbaux, P.-F. Coheur, R. Colin, S. Fally., and M. Bach, Water vapor line parameters in the 13 000-9250 cm^{-1} region, *J. Quant. Spectrosc. Radiat. Transfer, 74*, 493–510, 2002.

Noël, S., M. Buchwitz, H. Bovensmann, R. Hoogen, and J. P. Burrows, *Geophys. Res. Lett., 26*, 1841–1844, 1999.

Norton, R. H. and R. Beer, New apodizing functions for Fourier spectrometry, *J. Opt. Soc. Am., 66*, 259–264, 1976.

Polyansky, O., N. F. Zobov, S. Viti, and J. Tennyson, Water vapor line assignments in the near infrared, *J. Molec. Spectrosc., 189*, 291–300, 1998.

Polyansky, O. L., A. G. Császár, S. V. Shirin, N. F. Zobov, P. Barletta, J. Tennyson, D. W. Schwenke, P. J. Knowles, High-accuracy ab initio rotation-vibration transitions for water, *Science., 299*, 539–542, 2003.

Rodgers, C. D. , *Inverse Methods for Atmospheric Sounding: Theory and Practice*, World Scientific, London, 2000.

Rothman et al., The HITRAN molecular spectroscopic database: edition of 2000 including updates through 2001, *J. Quant. Spectrosc. Radiat. Transfer, 82*, 5–44, 2003.

Schermaul, R., R. C. M. Learner, A. A. D. Canas, J. W. Brault, O. L. Polyansky, D. Belmiloud, N. F. Zobov, and J. Tennyson, Weak line water vapor spectra in the region 13 200-15 000 cm^{-1}, *J. Molec. Spectrosc., 211*, 169–178, 2002.

Schermaul, R., R. C. M. Learner, D. A. Newnham, J. Ballard, N. F. Zobov, D. Belmiloud, and J. Tennyson, The water vapor spectrum in the region 8600-15,000 cm^{-1}: Experimental and theoretical studies for a new spectral line database. II. Linelist construction, *J. Mol. Spectrosc., 208*, 43–50, 2001.

Sierk, B., S. Solomon, J. S. Daniel, R. W. Portmann, S. I. Gutman, A. O. Langford, C. S. Eubank, K. H. Holub, S. V. Florek , Field test of spectral line intensity parameters for tropospheric water vapor, *Journ. Geophys. Res., 108*, D12, 4351, doi:10.1029/2002JD002985, 2003.

Smith, K. M., and D. A. Newnham, High-resolution atmospheric absorption by water vapor in the 830-985 nm region: Evaluation of spectral databases, *Geophys. Res. Lett., 28*, 3115–3118, 2001.

Smith, K. M., D. A. Nenwham, and R. G. Williams, Collision induced absorption of solar radiation in the atmsophere by molecular oxygen at 1.2 μm: field observations and model calculations, *Journ. Geophys. Res., 106*, 7541–7552, 2001.

Smith K. M., I. Ptashnik, D. A. Newnham and K. P. Shine, Absorption by water vapor in the 1 to μm region, *J. Quant. Spectrosc. Radiat. Transfer, 83*, 735–749, 2004.

Tolchenov, R. N., J. Tennyson, V. S. Sergei, N. F. Zobov, O. L. Polyanski, and A. N. Maurellis, Water line parameters for weak lines in the range 9000–12 700 cm^{-1}, *J. Molec. Spectr., 221*, 99–105, 2003.

Veihelmann, B., R. Lang, K. M. Smith, D. A. Newnham, and W. J. van der Zande, Evaluation of spectroscopic databases of water vapor between 585 and 600 nm, *Geophys. Res. Lett., 29*,10.1029/2002GL015330, 2002.

Wagner, T., J. Heland, M. Zöger, and U. PLatt, *Atmos. Chem. Phys., 3*, 651–663, 2003.

Wallace, L., K. Hinkle, and W. Livingston, An atlas of the spectrum of the solar photosphere from 13,500 to 28,000 cm^{-1} (3570 to 7405 Å), *Tech. rep.*, Kitt Peak National Observatory / National Solar Observatory, National Optical Astronomy Observatories, 1996.

Chapter 3

Evaluation of spectroscopic databases of water vapor between 585 and 600 nm

Abstract

The water vapor absorption band between 585 and 600 nm is suitable for atmospheric water vapor column retrieval from satellite data because saturation effects are absent and water is the only significant structured absorber within this region. Accurate knowledge of the absorption spectroscopy is important for the retrieval as well as for assessing radiative forcing. Spectral databases for this wavelength region lack experimental validation by atmospheric observations. By means of a line-by-line radiative transfer model we simulate the direct solar radiation reaching the ground using different spectral databases. We compare simulated spectra with high resolution measurements made using a ground based Fourier transform spectrometer. Instrument effects are considered and residuals are assigned to line intensity errors as far as possible. A quality estimate of four different databases is provided and the consequences for satellite-based instrumentations are discussed.

3.1 Introduction

Satellite-borne instruments allow quantitative study of atmospheric water vapor on a global basis. Water vapor mixing ratios can be retrieved from absorption measurements of solar radiation using the 585-600 nm absorption band. The small optical depth ($<$ 1.4 at the center of strong lines within the band for typical atmospheric conditions at mid-latitudes) is an advantage relative to absorption bands at longer wavelengths, while the stronger atmospheric Rayleigh scattering is a disadvantage. The space borne spectrometers GOME (Global Ozone Monitoring Experiment) and SCIAMACHY (SCanning Imaging Absorption SpectroMeter for Atmospheric CHartographY) measure reflected sunlight with moderate spectral resolution (0.3 nm at 588-600 nm) [*ESA*, 1995; *Bovensmann et al.*, 1999]. In order to accurately derive water vapor mixing ratios from the measured spectra, precise knowledge of the absorption spectroscopy is crucial.

Especially in the short wavelength region there is still need for both further investigation of the water vapor absorption spectrum as well as validation of existing spectral databases. *Learner et al.* [1999] calculate an additional absorption by theoretically predicted weak lines, which are not present in databases, to be on the orderof 1.5 to 2.5 W/m^2 for wavelengths shorter than 758 nm. Many weak lines given in spectral databases are not yet well characterized or assigned to a specific molecular transition. The accuracy of line intensity and air broadening values diminishes with decreasing wavelength since their temperature dependencies are often inferred from theory and from infrared data [*ESA*, 1999]. Databases are further restricted in accuracy due to limitations of the underlying measurements.

Here we report a study of water vapor line absorption in the vibrational overtone band at 585-600 nm (5ν polyad). We evaluate four different spectral databases, which characterize shape and intensity of the absorption lines within the band: HITRAN-96 [*Rothman et al.*, 1998], HITRAN-2000 (a recent update concerning water vapor [*Brown et al.*, 2001]), ESA-WVB [*Schermaul et al.*, 2001a,b] and a database provided by *Carleer et al.* [1999] referred to as ULB-BISA-UFR. The radiative transfer is simulated with a line-by-line forward model. The simulated spectra are compared with a clear sky measurement from a ground based Fourier transform spectrometer (FTS) located at the Rutherford Appleton Laboratory (RAL), that measures relative intensities in spectra of direct solar radiation. We provide a quality estimate for the spectroscopic databases and determine line intensity errors from the residuals of measured and modeled spectra. A similar study has been done by *Smith and Newnham* [2001] for the water vapor bands from 830 to 958 nm.

3.2 Data and model

We simulate the radiative transfer in solar occultation geometry as given by the reference measurement. The model has been described by *Lang et al.* [2002]. The spectrum of the incoming solar radiation at the top of the atmosphere is based on Fourier transform spectrometer measurements taken with the McMath-Pierce Telescope at National Solar Observatory (NSO, 2100 m above sea level). It has been corrected for atmospheric absorption by water vapor above the telescope [*Wallace et al.*, 1996]. The atmospheric absorption spectrum has been obtained from the ratio of two measurements with different air masses. This correction technique is ideal for separating solar and telluric absorption components and is independent of the spectroscopic databases studied. The spectral regions where saturation effects and instrument noise significantly affect the accuracy of this correction technique are masked out.

Atmospheric absorption by water vapor above the RAL spectrometer is calculated line-by-line for a series of layers. Line shapes are calculated as Voigt profiles [e.g. *Goody*, 1995] and depend on pressure and temperature [*Rothman et al.*, 1998]. Line shape and intensity values are taken from either HITRAN-96, HITRAN-2000, ESA-WVB or ULB-BISA-UFR. HITRAN-96 is a benchmark database which is widely-used. The water vapor data for our band region given in HITRAN-2000 is very similar to that in HITRAN-96. No absorption lines are added (both contain 592 lines) but line intensities differ slightly due to the correction described by *Giver et al.* [2000]. HITRAN-2001, the most recent update, does not differ from HITRAN-2000 concerning the water vapor absorption within our band and is not considered separately. The ULB-BISA-UFR database is derived from independent long path length FTS measurements. 939 Lines are assigned using line lists from *Partridge and Schwenke* [1997] and *Polyansky et al.* [1999]. The average intensity of lines that are not included in HITRAN (1.7×10^{-26} cm/molec) is more than one order of magnitude smaller than the average intensity of the lines common to both databases (3.3×10^{-25} cm/molec). The ESA-WVB database is based on both theoretical and existing experimental data. Line positions and intensities are taken from HITRAN and the corresponding line assignments are adopted from *Polyansky et al.* [1998] and *Carleer et al.* [1999]. Frequencies and assignments for (313) additional lines are taken from *Carleer et al.* [1999] and *Naus et al.* [2001]. It is thus not entirely independent of either HITRAN or the ULB-BISA-UFR database.

Additional atmospheric extinction is accounted for as absorption by ozone, the O_2-O_2 collision complex and Rayleigh scattering. Very weak absorption by NO_2 [*Burrows et al.*, 1998] is neglected. Layers are characterized by profile data for pressure, temperature, and volume mixing ratios of water vapor. These data are interpolated to the location of the measurement site from Operational Analysis data supplied by the European Centre for Medium-Range Weather Forecasts (ECMWF). Profile data for ozone, O_2, and N_2 are taken from a standard mid-latitude summer model atmosphere.

Air mass factors are derived taking the spherical geometry of the Earth's atmosphere into account. Here we may neglect single and multiple scattering because of the measurement geometry. In direct occultation measurements with a small field of view, single scattering has no impact on the photon path length. The intensity of multiply scattered light decreases rapidly as the optical path deviates from the direct one, because scattering phase functions are peaked in the forward direction. As a consequence, the effect of multiple scattering on the air mass factor is also small.

The reference spectrum is measured under clear sky conditions using a ground based Fourier transform spectrometer at RAL. Direct solar radiation is measured with an instrumental resolution of 0.05 cm^{-1} (0.0017 nm) and a radiometric accuracy of better than 0.5% of the signal [*Smith et al.*, 2001]. Comparison of the spectra is performed on a resolution of 0.04 cm^{-1} (0.0014 nm). This is sufficient to resolve the line structure of the absorption since air broadened water vapor line widths are typically on the orderof 0.1 to 0.2 cm^{-1} full width at half maximum.

3.3 Results

The upper graph in Figure 3.1 shows part of the observed spectrum revealing the high density of absorption lines as well as the presence of some solar features (indicated by the arrows). The spectrum could be modeled without adapting parameters of the atmospheric profile or the databases. The only free parameters are 5 coefficients of the polynomial fit procedure that was used to adjust the background of measured and modeled spectra. A baseline oscillation with a period of about 0.4 nm was found in the differences between modeled and measured spectra (not shown). It is an artifact due to an interference from the optical setup of the measurement and has therefore been filtered out. At Fraunhofer line positions we find additional systematic errors. Solar lines in the modeled spectrum

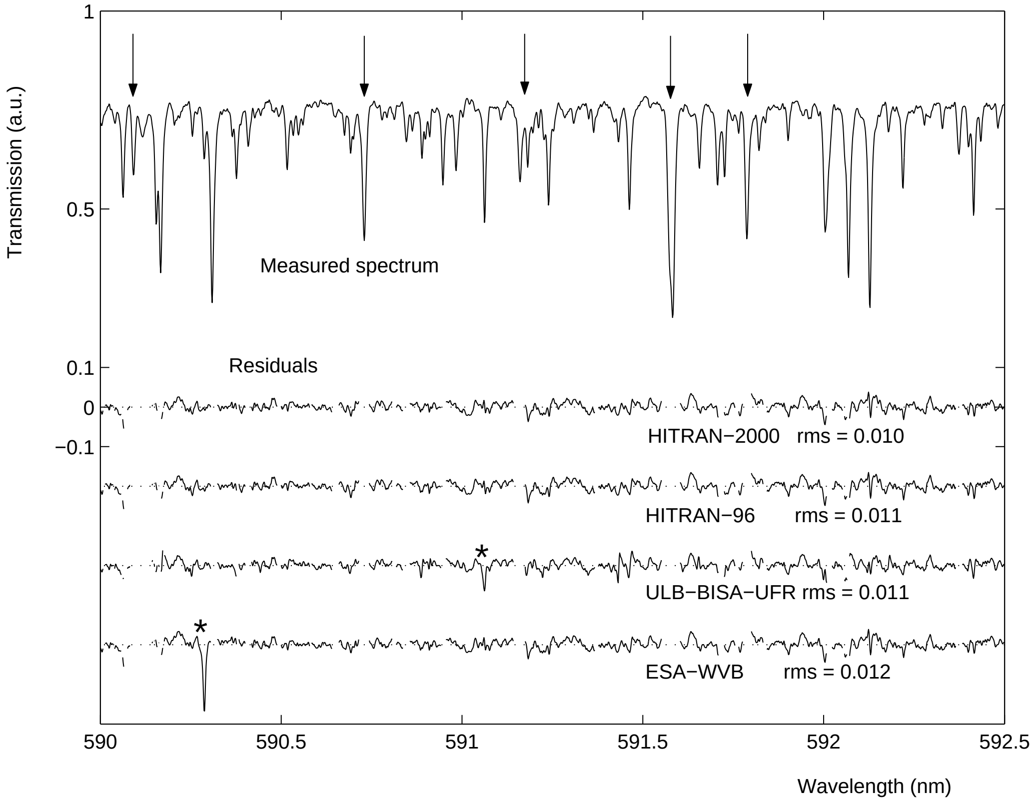

Figure 3.1: Part of the measured RAL spectrum between 590 and 593 nm. The arrows indicate solar Fraunhofer lines. The lower part shows the residuals (modeled-measured) using the four data-bases HITRAN-2000, HITRAN-96, ULB-BISA-UFR and ESA-WVB. The asterisks are explained in the text.

appear narrower than in the measurement. In order to study purely atmospheric effects, we masked out the affected parts of the spectrum. As a result we find residuals to be mostly below 3% of the background and root mean square (RMS) values of about 1% (lower part of Fig. 3.1). This means that relative absorption line intensities given in the databases agree well with observed atmospheric absorption. The RMS of the residuals is a quality estimate for the line intensity and shape information in this spectral region given in the database. HITRAN-2000, ULB-BISA-UFR and the HITRAN-96 database are similar in this regard (RMS = 0.0103, 0.0107 and 0.0108, respectively), while the quality of the ESA-WVB is slightly lower (RMS = 0.0124). The ULB-BISA-UFR database is based on one single independent measurement campaign. The RMS of the difference between the simulated spectra based on ULB-BISA-UFR and HITRAN-2000 is smaller than the

RMS of the residuals mentioned above. This indicates that this database is not entirely independent of HITRAN-2000. Part of the agreement may be due to the fact that line width parameters have a common theoretical source.

The shape of a residual spectrum indicates whether the intensity of a line is over- or underestimated. For example, we identify a very strong overestimation of the line intensity given in ESA-WVB at 590.29 nm and there is a line intensity overestimation in the ULB-BISA-UFR database at 591.06 nm (marked with asterisks in Fig. 1).

The shape of the residual spectrum is dependent on the atmospheric water vapor profile. By modifying the profile the overall agreement between modeled and measured spectra can be slightly increased. An optimum is found at a decrease of the water vapor mixing ratio within the lowest two levels (< 2 km) by 30%, which is a decrease of the total water vapor column by 18%. The magnitude of this decrease lies within the error margins of the atmospheric profile data used, as inferred from differences between ECMWF and radiosonde profiles and related uncertainties.

In general, residuals are larger at line center positions. For a selection of absorption lines that show little blending with neighbouring lines we attribute the residuals to errors in the line intensity S given in HITRAN-2000 and the ULB-BISA-UFR database. The selection is purely based on the criterion of little blending and is a priori independent of the agreement or disagreement of the databases. Nevertheless, the lines selected are common to both databases. From Beer-Lambert's law one can derive:

$$\frac{\Delta S}{S} = \frac{ln(\frac{I_{mod}}{I_{meas}})}{\int S(l)\, V(l)\, n(l)\, dl} \tag{3.1}$$

I_{meas} and I_{mod} here are the intensities of measured and modeled radiation, V is the Voigt line shape function as described by *Goody* [1995], n is the absorber density and l is the optical path length. The equation is evaluated at the line center position implicitly assuming a correct line width. As a consequence, the calculated $\Delta S/S$ is sensitive to the water vapor profile, which is used in the radiative transfer model. The intensity values I_{meas} and I_{mod} at the center of lines in the modeled and the measured spectra are determined using a parabolic fit based on three data points: the local minimum and the two neighbouring points. For both HITRAN-2000 and the ULB-BISA-UFR database the average of $\Delta S/S$ is -10% for the nominal water vapor profile and +2% for the modified water vapor profile that has been optimized as outlined above. This supports the assumption that the modified water vapor profile is closer to reality than the one that was initially assumed. Figure 3.2 shows $\Delta S/S$ for HITRAN-2000 (black symbols) and ULB-BISA-UFR (gray symbols) based on the modified water vapor profile. The error bars indicate the error due to the radiometric accuracy of the measured data. The $\Delta S/S$ values for HITRAN-2000 cover a range from -19% to +35%. *Belmiloud et al.* [2000] find a spread of the same order of magnitude for lines between 893 and 980 nm given in HITRAN-96. The spread of $\Delta S/S$ for ULB-BISA-UFR (ranging from -25% to +20%) is smaller and the RMS is 9% lower than for HITRAN-2000. This means that the line intensities of the selected lines are better described by the ULB-BISA-UFR database. Line intensity correction terms for the two databases are correlated with a correlation coefficient of 0.41. The weak correlation

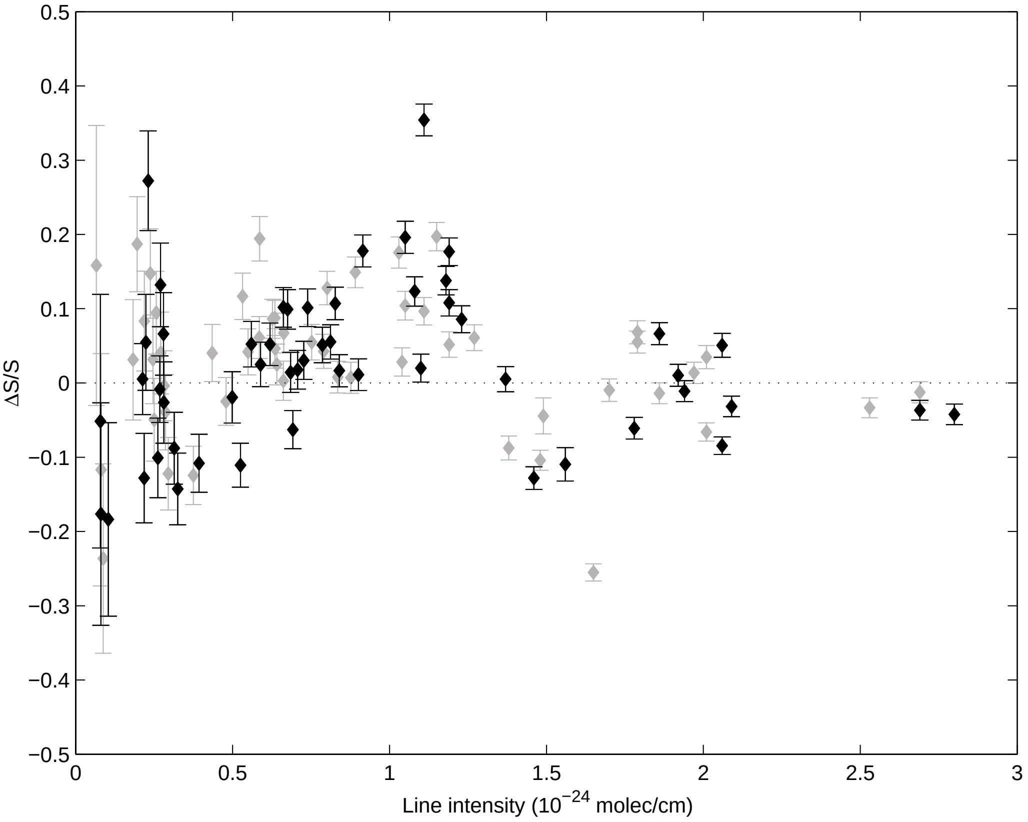

Figure 3.2: Equivalent relative line intensity error ($\Delta S/S$) for HITRAN-2000 (black symbols) and ULB-BISA-UFR (gray symbols). The error bars reflect the uncertainty related to the radiometric measurement error of the RAL spectrum.

confirms that $\Delta S/S$ represents - beyond a common error component that might as well be due to errors in the atmospheric modeling - an estimate for the sign and amplitude of intensity errors of individual lines.

In order to evaluate database errors for the satellite based instrument GOME, we calculate an equivalent relative line intensity error at moderate resolution [c.f. *Lang et al.*, 2002]

$$(\frac{\Delta S}{S})^* = \frac{ln(\frac{\int I_{mod}\, d\lambda}{\int I_{meas}\, d\lambda})}{\frac{1}{\Delta\lambda}\int\int \sigma(l,\lambda)\; n(l)\; dl\; d\lambda}, \tag{3.2}$$

where σ is the absorption cross section and I_{mod} and I_{meas} are modeled and measured intensities at high resolution. The limits of the wavelength integration are defined by the detector spectral sampling of GOME (0.21 nm). The residual contributions from line shape errors average out. Hence the quantity $(\Delta S/S)^*$ reflects line intensity errors and possible systematic errors in the radiative transfer calculation at moderate resolution. The normalization with the optical depth removes the dependence on the optical thickness, i.e. the dependence on the water vapor profile and the geometry of the optical path. We exploit this property in order to quantify the impact of the database errors of HITRAN-2000 on simulated GOME spectra as explained in the following. The GOME instrument measures reflected sunlight. A fraction of the measured light is reflected at the earth surface while other components are scattered within the atmosphere at different heights. For each component we can infer a relative intensity error from $(\Delta S/S)^*$ and the respective optical thickness. Components are then weighted with the transmissions and single scattering albedos (respectively ground albedo) that are taken from radiative transfer simulations in GOME geometry. Assuming that $(\Delta S/S)^*$ represents mainly database errors, we may interpret the inferred error as an estimate of the impact of database errors on simulated GOME spectra. For a water vapor column of 5×10^{22} molec/cm^2 the RMS of the inferred error is of the order of magnitude of the shot noise level of the GOME instrument (0.1% relative error [*DLR*, 1999]).

3.4 Conclusion

The high level of agreement of high resolution FTS measurements and modeled spectra shows that the databases studied accurately characterize a substantial part of the atmospheric water vapor line absorption within the spectral band from 588 to 600 nm. However, residuals verify that there are lines missing in the databases and that there are mismatches in line intensities. Residuals at Fraunhofer line positions suggest that the solar spectrum used for the simulation differs from that measured. Comparing different solar spectra directly we find differences in line shape and relative intensity of Fraunhofer lines. A space-borne high resolution measurement of the solar incoming radiation would provide an important and relevant input for atmospheric modeling. For a selection of lines that show little blending with neighbouring lines, and that are common to both databases, it is found that line intensities are better described by the ULB-BISA-UFR database than by HITRAN-2000. Nevertheless, the overall agreement between model and measurement in the wavelength range studied here is slightly better when using HITRAN-2000. Databases show common systematic errors since they are not entirely independent of each other and measurements that are used for the creation of the databases may have the same restrictions. The impact of database errors on simulated GOME spectra is estimated to be significant if the water vapor column exceeds 5×10^{22} molec/cm^2. Water vapor columns above this critical value are frequently found in mid-latitude atmospheres while the value is usually exceeded in the tropics. Hence, at present database errors are still relevant. In order to increase the reliability of our comparison, coincidental measurements of the ground based FTS, the GOME instrument, and a radiosonde measurement of the atmospheric profile could be carried out. This would ensure that the same air mass is present for all measurements.

Bibliography

Belmiloud, D., R. Schermaul, K. M. Smith, N. F. Zobov, W. Brault, R. C. M. Learner, D. A. Newnham, and J. Tennyson, New studies of the visible and near-infrared absorption by water vapour and some problems with the HITRAN database, *Geophys. Res. Lett.*, *27*, 3703–3706, 2000.

Bovensmann, H., J. P. Burrows, M. Buchwitz, J. Frerick, S. Noel, V. V. Rozanov, K. V. Chance, and A. P. H. Goede, SCIAMACHY: Mission objectives and measurement modes, *J. Atm. Sci.*, *56*, 127–150, 1999.

Burrows, J. P., A. Dehn, B. Deters, S. Himmelmann, A. Richter, S. Voigt, and J. Orphal, Atmospheric remote-sensing reference data from GOME: 1. temperature-dependent absorption cross sections of NO_2 in the 231-794 nm range, *J. Quant. Spectros. Radiat. Transfer*, *60*, 1025–1031, 1998.

Brown, L. R., R. A. Toth, and M. Dulick, Line parameters of water from 9600 to 11,400 cm^{-1} , *J. Mol. Spectrosc.*, submitted, 2001.

Carleer, M., A. Jenouvrier, A. C. Vandaele, P. F. Bernath, M. F. Merienne, R. Colin, N. F. Zobov, O. L. Polyansky, J. Tennyson, and V. A. Savin, The near infrared, visible and near ultraviolet overtone spectrum of water, *J. Chem. Phys.*, *111*, 2444–2450, 1999.

DLR, *GOME Data Processor Extraction Software User's Manual*, DLR/DFD Oberpfaffenhofen, Germany, 1999, doc.no.: ER-SUM-DLR-DLR-GO-0045.

ESA, *The Global Ozone Monitoring Experiment Users Manual*, ESA/ESTEC Noordwijk, The Netherlands, 1995, ESA Publication SP-1182.

ESA, *Measurement of* H_2O *Absorption Cross-Sections for Exploitation of GOME Data*, ESA/ESTEC Noordwijk, The Netherlands, 1999, ESTEC Contract No. 13312/99/NL/SF.

Giver, L. P., C. Chackerian Jr., and P. Varanasi, Visible and near-infrared $H_2^{16}O$ line intensity corrections for HITRAN-96, *J. Quant. Spetrosc. Radiat. Transfer*, *66*, 101–105, 2000.

Goody, R., *Principles of Atmospheric Physics and Chemistry*, Oxford University Press, 1995.

Lang, R., A. N. Maurellis, W. J. van der Zande, I. Aben, J. Landgraf, and W. Ubachs, Forward modelling and retrieval of water vapor from GOME: Treatment of narrow band absorption spectra, *J. Geophys. Res.*, in press, 2002.

Learner, R. C. M., W. Zhong, J. D. Haigh, D. Belmiloud, and J. Clarke, The contribution of unknown weak water vapor lines to the absorption of solar radiation, *Geophys. Res. Lett.*, *26*, 3609–3612, 1999.

Naus, H., W. Ubachs, P. F. Levelt, O. L. Polyansky, N. F. Zobov, and J. Tennyson, Cavity-ring-down spectroscopy on water vapor in the range 555-604 nm, *J. Mol. Spectrosc.*, *205*, 117–121, 2001.

Partridge, H., and D. W. Schwenke, The determination of an accurate isotope dependent potential energy surface for water from extensive ab initio calculations and experimental data, *J. Chem. Phys.*, *106*, 4618–4639, 1997.

Polyansky, O. L., N. F. Zobov, S. Viti, and J. Tennyson, Water vapor line assignments in the near infrared, *J. Mol. Spectrosc.*, *189*, 291–300, 1998.

Polyansky, O. L., J. Tennyson, and N. F. Zobov, Spectroscopy from first principles: a breakthrough in water line assignments, *Spectrochimica Acta(A): Mol. Biomol. Spectrosc.*, *55*, 659–693, 1999.

Rothman et al., The HITRAN molecular spectroscopic database and HAWKS (HITRAN Atmospheric Workstation) 1996 edition, *J. Quant. Spetrosc. Radiat. Transfer*, *60*, 665–710, 1998.

Schermaul, R., R. C. M. Learner, D. A. Newnham, R. G. Williams, J. Ballard, N. F. Zobov, D. Belmiloud, and J. Tennyson, The water vapor spectrum in the region 8600-15,000 cm^{-1}: Experimental and theoretical studies for a new spectral line database. I. laboratory measurements, *J. Mol. Spectrosc.*, *208*, 32–42, 2001a.

Schermaul, R., R. C. M. Learner, D. A. Newnham, J. Ballard, N. F. Zobov, D. Belmiloud, and J. Tennyson, The water vapor spectrum in the region 8600-15,000 cm^{-1}: Experimental and theoretical studies for a new spectral line database. II. linelist construction, *J. Mol. Spectrosc*, *208*, 43–50, 2001b.

Smith, K. M., and D. A. Newnham, High-resolution atmospheric absorption by water vapor in the 830-985 nm region: Evaluation of spectral databases, *Geophys. Res. Lett.*, *28*, 3115–3118, 2001.

Smith, K. M., D. A. Newnham, and R. G. Williams, Collision-induced absorption of solar radiation in the atmosphere by molecular oxygen at 1.27μm: Field observations and model calculations, *J. Geophys. Res.*, *106*, 7541–7552, 2001.

Wallace, L., K. Hinkle, and W. Livingston, An atlas of the spectrum of the solar photoshpere from 13,500 to 28,000 cm^{-1} (3570 to 7405 Å), *Tech. rep.*, Kitt Peak National Observatory / National Solar Observatory, National Optical Astronomy Observatories, 1996.

Chapter 4

Mineral dust aerosol

4.1 Introduction

Apart from gases such as molecular nitrogen and oxygen, the atmosphere contains particles in the solid and the liquid phase. These particles are referred to as aerosols. Liquid water and ice particles are generally excluded from this term. The size of aerosol particles ranges from tens of a nanometer to hundreds of micrometers. The number density typically ranges from a few hundred to more than 10^6 particles per cm^3. Aerosols originate either from condensation from the gas phase or are brought into the atmosphere by dispersion processes. The most efficient removal process for small particles with radii below 10 μm is wet deposition. Aerosol particles seed cloud condensation and are removed by precipitation. For larger particles, sedimentation becomes an important removal process since the viscous drag is proportional to the particle surface, while the gravitational force scales with the volume. Aerosols can be classified according to the chemical composition, phase, refractive index, origin, size and shape etc. We introduce here the most important aerosol types that occur in the Earth atmosphere [cf. *D'Almeida et al.*, 1991].

Condensation aerosols originate mainly from natural and anthropogenic emissions of SO_2, H_2S, NO_x, and carbonaceous components. Sulfate and nitrate aerosols are mainly formed by homogeneous condensation of sulfuric and nitric acid H_2SO_4 and HNO_3, i.e. the oxidation products of these emissions. Primary particles have radii on the order of 10 nm and grow by coagulation with other aerosol particles. The particle radii usually do not exceed 1 μm [*Roedel*, 1992]. Dispersion aerosols are mainly sea spray, mineral soil particles raised by the wind, volcanic debris, and mineral and organic particles raised by forest and bush fires. These particles are much larger than particles formed by condensation from the gas phase and have linear dimensions ranging from about 0.1 μm up to 100 μm.

Sea salt particles originate from ocean water droplets. These droplets are emitted from collapsing bubbles that are formed in breaking waves. This process is efficient when the near surface wind speed exceeds 3 m/s. The released droplets partially dry out and leave behind salt droplets with high salt concentrations or salt particles with radii in the submicrometer regime [*Heintzenberg et al.*, 2000]. Wet deposition is a very efficient removal process due to the hygroscopy of sea salt particles. The vertical mixing in the marine atmosphere is not as pronounced as over land. As a consequence, the vertical distribution of sea salt aerosol is confined to the lower troposphere [*Roedel*, 1992].

Desert dust aerosol originates mainly from dry lakebeds in the Sahara, the East Asian and the Saudi Arabian deserts and other arid regions [*Husar et al.*, 1997]. In many ocean regions, desert dust is the dominant aerosol type. In terms of mass, desert dust aerosol has the largest source strength of all aerosol types, comparable only to the source strength of sea salt. Estimates for the emission rates range from 60 to 3000 Tg/yr (1 Tg = 10^{12} g) [*D'Almeida et al.*, 1991]. The source strength depends critically on the wind speed and the turbulent state of the boundary layer as well as on local soil properties, topography, hydrology etc. [*Zender et al.*, 2003]. Soil particles can be detached from the ground when the shear force of the air exceeds the adhesion force that ties the particles to the surface. Particles that fall back on the ground may pass on some of their impulse to other soil particles and detach them from the ground. If the wind speed exceeds about 0.5 m/s avalanche effects can be triggered and many particles are released into the boundary layer. This process is size selective, since adhesion forces between particle and the ground are important for particles with radii lower than a few tenth of a micrometer. Another size selection results from the fact that particles require a certain mass in order to cross the laminar layer of air and thus enter the turbulent regime where efficient vertical transport is possible. As a consequence most of the mass is released in the size range from 1 μm to 10 μm [*Roedel*, 1992].

The sources of soil derived aerosol are located on the continents, mainly at low latitudes. Here, the pronounced vertical mixing can transport the particles many kilometers high. The largest part of the tropospheric mineral aerosol is usually present in the lowest 5 km. In the marine atmosphere at low latitudes, dust particles govern the free lower troposphere while sea salt particles dominate in the marine boundary layer, which is usually less than 1 km thick [*Garrett et al.*, 2003]. The long-range transport often occurs in distinct layers at a height of a few kilometers [*Colarco et al.*, 2003]. Dust plumes in the lee of deserts stand out as the most prominent features in satellite images [*Garrett et al.*, 2003]. Mineral dust is removed from the atmosphere by gravitational settling followed by dry deposition and is scavenged by seeding cloud condensation and colliding with falling rain drops and snow [*Song-Miao et al.*, 2004]. Dry deposition preferentially removes dust with sizes larger than 7 μm [*Maring et al.*, 2003]. Size distributions of atmospheric dust aerosol derived from observations of ground-based and satellite-borne sensors typically peak at volume-equivalent radii between 1 μm and 5 μm [*Tanré et al.*, 2001].

During volcanic eruptions large quantities of ash can be released into the atmosphere. The volcanic debris are small irregular particles and may have a spongy structure. The linear dimensions are between 0.1 μm and 100 μm [*Muñoz et al.*, 2004]. During the strong eruptions of the volcanoes El Chichon (1982) and Pinatubo (1991) a large amount of volcanic ash was thrown into the stratosphere. The global aerosol load was doubled compared to the 'clean' atmosphere before the outbreak [*Geogdzhayev et al.*, 2004]. The decrease of the global aerosol mass to the usual background level took many months. The long lifetime of stratospheric mineral aerosols is related to the low humidity and the absence of efficient wet deposition processes.

Essentially all liquid-phase aerosol particles are spherical. In contrast, mineral soil and volcanic debris particles have irregular shapes. Tropospheric mineral aerosol may lose its nonspherical character by condensation of water vapor from the surrounding air on the particle surface. The hygroscopic growth is facilitated by chemical alterations of the particle surface induced by industrial emissions. This is unlikely for the material present in dust plumes and dust outflow regions close to the source, and for mineral aerosol surrounded by dry air masses. Model calculations and observations of dust concentrations suggest that Saharan dust aerosol remains largely hygrophobic during its transport, while Asian mineral dust over the Pacific is often hydrophilic [*Song-Miao et al.*, 2004]. Hygroscopic growth measurements on dust aerosol collected on Barbados, West Indies, show that the optical properties of North African dust aerosol are largely insensitive to the relative humidity [*Li-Jones et al.*, 1998]. Stratospheric mineral aerosol from volcanic eruptions is likely to retain its irregularity for a long time due to the low stratospheric water vapor abundance.

4.2 Implications for weather and climate

Atmospheric aerosols influence the Earth's weather and climate system in many ways. Mineral aerosol absorbs and reflects solar light as well as thermal infrared radiation emitted from the Earth surface. This is referred to as the *direct radiative effect*. Tropospheric mineral aerosol has an impact on the optical properties and the lifetime of clouds. This is referred to as the *indirect effect*. Chemical reactions in the atmosphere are catalyzed by virtue of the large particle surface. For example, the tropospheric concentrations of OH, HO_2, O_3 and HNO_3 are reduced in the presence of mineral aerosol [*Bian and Zender*, 2003]. Aerosols in general can cause respiratory diseases in human beings.

The perturbation of the radiative balance due to the direct radiative effect of an aerosol layer is often expressed in terms of radiative forcing ΔF with the units $\mathrm{W/m^2}$. There are various definitions for radiative forcing. Here we would like to refer to a definition given by *Haywood and Boucher* [2000]: Radiative forcing is the change in the net irradiance at the tropopause due to an applied perturbation holding all tropospheric variables fixed, once stratospheric temperatures have been allowed to adjust to equilibrium. Nonabsorbing aerosols increase the reflection of sunlight by the atmosphere (Fig. 4.1). This leads to a net cooling effect (negative values of radiative forcing). Strongly absorbing aerosols such as black carbon heat the troposphere (positive radiative forcing).

The direct radiative forcing caused by mineral dust aerosol can be significant on a global scale and dominant on a regional scale [*Tegen et al.*, 1996; *Sokolik and Toon*, 1996]. The direct radiative effect is strong especially in dust outflow regions such as the tropical and subtropical North Atlantic region or the North Pacific [*Kinne and Pueschel*, 2001]. The perturbation of the shortwave radiation balance at the tropopause can be as large as $\Delta F = -60\ \mathrm{W/m^2}$. This estimation has been derived from air-borne measurements during dust events off the west coast of Africa with broad band radiometers [*Haywood et al.*, 2001]. Satellite and ground-based observations at the Canary Islands during a Sahara dust outbreak event in 1994 indicate that the shortwave radiative forcing at the top of the troposphere was -9.7 $\mathrm{W/m^2}$ over ocean and -4.5 $\mathrm{W/m^2}$ over land. Extending such results to global scale averages values of -1.22 $\mathrm{W/m^2}$ over ocean and -0.57 $\mathrm{W/m^2}$ over land are estimated [*Díaz et al.*, 2001]. A longwave radiative forcing of dust aerosol over

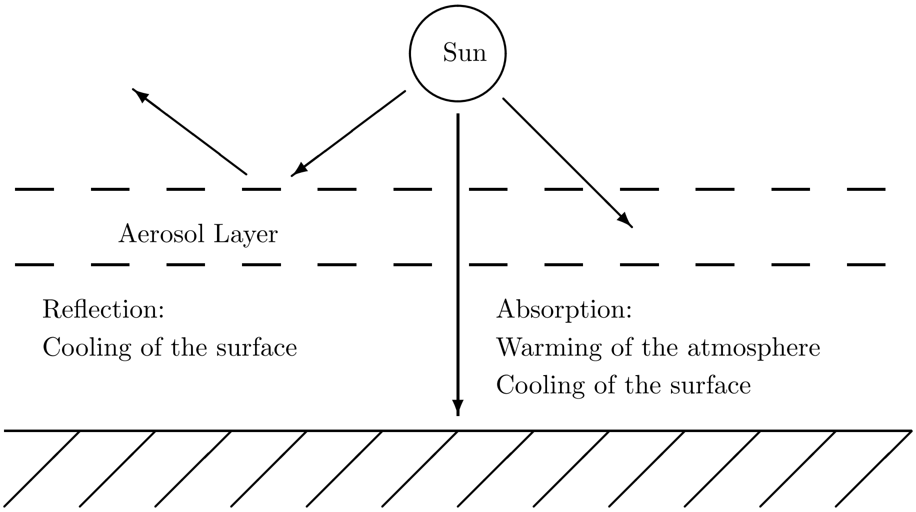

Figure 4.1: Direct radiative effect of an aerosol layer.

deserts of +7 W/m^2 in cloud-free conditions is reported by *Zhang and Christopher* [2003]. Estimating the global average values is very difficult since the direct forcing depends on the vertical distribution of both clouds and aerosols [*Quijano et al.*, 2000]. Estimates of the total radiative forcing due to mineral aerosol including the shortwave as well as the longwave perturbation vary from +0.09 to -0.46 W/m^2. Even the sign of the radiative forcing is not well established due to the competing effects of solar and terrestrial radiative forcing [*Haywood and Boucher*, 2000].

Aerosols serve as cloud condensation and ice nuclei. An increase in the aerosol concentration can therefore cause an increase in the cloud droplet number and a decrease in the mean cloud drop size. As a consequence, the cloud top height, the albedo, and the lifetime of clouds increase and precipitation may be inhibited [*Haywood and Boucher*, 2000]. The aerosol indirect effect depends strongly on the number density, the size, and the chemical composition of the aerosol. Young mineral dust aerosol is usually only weakly hygroscopic. Chemical alterations related to surface reactions with industrial emissions cause mineral aerosol to be efficient seeds for cloud condensation. Being exposed to NO_2 and NH_3 the surface of tropospheric mineral dust can become hygroscopic. Calcium carbonate particles react with gas-phase nitric acid and can even be dissolved [*Krueger et al.*, 2003]. Air-borne lidar observations show that Saharan dust particles are effective ice nuclei in altocumulus clouds [*Sassen et al.*, 2003; *DeMott et al.*, 2003]. A statistical comparison of a long time data record for mineral dust and clouds indicates that mineral dust indeed supresses precipitation from thin low altitude clouds and changes of ice clouds [*Mahowald and Kiehl*, 2003]. Observational evidence for a net cooling effect due to the indirect effect of aerosol is based on radiative flux measurements combined with a cloud parcel model [*Penner et al.*, 2004]. The uncertainty of estimates for the perturbation of the global radiation balance due to the indirect effect are on the orderof 1.5 $\mathrm{W/m^2}$ [*Ghan et al.*, 2001].

4.3 Remote sensing

Aerosols are monitored using observations of reflected and transmitted sunlight from ground-based and satellite-borne sensors [*Kaufman et al.*, 2002]. Many aerosol properties have to be measured in order to quantify the impact of the aerosols on weather and climate. These properties include the amount, the size distribution, the spatial distribution, and the chemical composition. The simultaneous and accurate retrieval of all relevant aerosol parameters is challenging and requires advanced sensors. Ground-based instruments of the global AErosol RObotic NETwork (AERONET) measure the sun and sky radiance in various observation geometries at various wavelengths [*Holben et al.*, 1998]. An advanced retrieval algorithm is used to simultaneously retrieve the optical thickness, the real and the imaginary part of the refractive index, and the size distribution from these observations [*Dubovik and King*, 2000]. The advanced sensor POLarization and Directionality of the Earth's Reflectances (POLDER) measures both the intensity and the polarization of reflected sunlight in various observation geometries at various wavelengths. The impressive capabilities of the POLDER instrument for monitoring aerosols have been demonstrated by *Deuzé et al.* [2000, 2001]. A satellite instrument capable of simultaneously retrieving all relevant aerosol parameters needs to be a high-accuracy photopolarimeter with multi-angle capabilities measuring in a wide spectral range from 0.4 to 2.4 μm [*Mishchenko et al.*, 2004]. The ideal aerosol monitoring instrument is at the same time an imaging sensor with a high spatial resolution (1 km × 1 km). This is important for the distinction between aerosols and clouds. These requirements are not fully satisfied by any of the existing satellite-based sensors. Currently, the quantitative understanding of global aerosol characteristics must still rely on intercomparisons of derived products from different ground-based and satellite-borne sensors [*King et al.*, 1999].

The retrieval of aerosol parameters is complicated by the presence of irregularly-shaped aerosols. A large part of the soil derived aerosol present in the troposphere as well as stratospheric aerosol from volcanic eruptions is irregularly-shaped. Conventional aerosol remote sensing techniques are based on Mie theory, which treats absorption and scattering of light by spherical particles. The particle nonsphericity can cause substantial errors in aerosol retrievals that are based on the spherical shape approximation [*Mishchenko et al.*, 1995].

The retrieval of aerosol parameters requires accurate forward modeling of the measurement. This includes an accurate description of the absorption and the single-scattering properties of the aerosol as function of the particle size and the refractive index. The cross sections of absorption c_{abs} and scattering c_{scat} describe the probability of absorption and single-scattering processes to occur. The scattering matrix $\mathbf{F}$ describes the change of the intensity and the polarization of a light beam caused by a single scattering process. The scattering matrix relates the Stokes vectors of the incoming and the scattered light $\mathbf{I}_{\mathrm{in}}$ and

$\mathbf{I}_{\text{scat}}$, viz.

$$\mathbf{I}_{\text{scat}} \propto \; c_{\text{scat}} \, \mathbf{F} \, \mathbf{I}_{\text{in}}. \tag{4.1}$$

The elements of the Stokes vector **I** represent the total intensity (I) and linearly (Q and U) and circularly (V) polarized components. Light scattering by individual particles is referred to as single-scattering even though many reflection and refraction process may be involved on a microscopic scale. In the following, we use the term *single-scattering* for light scattering by particle ensembles as long as each light component interacts with one particle only. Single scattering by an ensemble of particles is described by Eq. (4.1) using the ensemble-average scattering matrix and the ensemble-average scattering cross sections. The scattering matrix **F** of an ensemble of randomly-oriented irregular particles has the block diagonal form

$$\mathbf{F}(\boldsymbol{\Theta}) = \begin{pmatrix} F_{11}(\Theta) & F_{12}(\Theta) & 0 & 0 \\ F_{12}(\Theta) & F_{22}(\Theta) & 0 & 0 \\ 0 & 0 & F_{33}(\Theta) & F_{34}(\Theta) \\ 0 & 0 & -F_{34}(\Theta) & F_{44}(\Theta) \end{pmatrix}. \tag{4.2}$$

This is generally the case for ensembles of scatterers, where particles and mirror particles are present in equal numbers. The elements F_{ij} are functions of the scattering angle Θ, i.e. the angle between incoming and scattered beam. The scattering angle $\Theta = 0°$ denotes forward scattering. The scattering matrix depends on the refractive index, the size distribution, and the shape of the scattering particles.

For spherical particles the scattering matrix and the cross sections of scattering and absorption can be calculated using Mie theory. For nonspherical particles a number of exact and approximate methods can be used. We shortly introduce a few widely used methods [cf. *Mishchenko et al.*, 2002]. These methods are applicable to different size ranges and are mostly restricted to particle shapes with certain symmetries. The limits of the size ranges are usually given in terms of the size parameter $x = 2\pi r/\lambda$, where r is the radius of a volume-equivalent sphere and λ is the wavelength. The size limits given are estimates and may depend on the refractive index and the particle shape.

Geometric Optics Approximation	This method, also known as the 'ray-optics approximation', is based on the assumption that the scattering particle is much larger than the wavelength. An incident plane wave is represented by a collection of independent rays. The propagation of each ray through the particle is calculated independently. Reflection and refraction at the particle surface as well as absorption in the particle volume are taken into account. Interference effects, however, are neglected. This method is applicable for particles with arbitrary shapes and size parameters $x \geq 60$. A modification of this method is the geometric-optics-integral-equation method [*Young and Liou*, 1996]. Particles with size parameters as small as $x = 30$ can be treated with this method. This model is applied in Chapter 7 for light scattering simulations by large nonspherical particles in combinations with a statistical shape model.
T-matrix method	The T-matrix method is an exact method based on the assumption that both the incident and the scattered light fields can be expanded in spherical vector functions. The T-matrix relates the expansion coefficients of the incoming field with the expansion coefficients of the scattered field and is calculated using the extended boundary condition method. Once the T-matrix is known, the orientation averaging of the scattering properties is very efficient. This is a major advantage as compared to other methods, where the light scattering has to be calculated for each orientation independently. A very efficient T-matrix code for rotationally symmetric targets has been developed by *Mishchenko* [1991]. This method is very efficient for spheroidal particles with size parameters up to $x = 100$ [*Mishchenko and Travis*, 1998]. Light scattering by mineral aerosol is often simulated using T-matrix calculations for an ensemble of spheroids with a distribution of aspect ratios. The aspect ratio ϵ of an oblate (prolate) spheroid is defined as the ratio of the major to the minor (minor to major) axis length. The spheroidal model is used extensively in all following chapters.

Discrete Dipole Approximation

In the Discrete Dipole Approximation (DDA) a particle is represented by an array of dipoles. The electro-magnetic response of each dipole is determined as a function of the external field and the fields scattered by all other dipoles [*Purcell and Pennyacker*, 1973]. The DDA method poses essentially no restrictions to the particle shape. The computation time and the internal memory required for the numerical calculations increases strongly with increasing size parameter. The size limit of this method is on the orderof $x = 15$. This model is applied in Chapter 7 for light scattering simulations by small nonspherical particles in combinations with a statistical shape model.

The T-matrix calculations for spheroidal particles have been used to estimate the impact of the nonsphericity of irregular mineral aerosol on remote sensing and on climate modeling [e.g. *Mishchenko et al.*, 1995; *Kahn et al.*, 1997; *Kahnert and Kylling*, 2004]. Natural mineral aerosol usually comprises particles with volume-equivalent sphere radii ranging from 0.1 to 100 μm, which corresponds to size parameters x from 1 to 1000 at visible wavelengths. It is thus a difficult task to compute the single-scattering properties of mineral dust at visible wavelengths with one method alone. With a combination of the T-matrix method (for particles with $x \leq 40$) and the geometric-optics-integral-equation method (for the larger particles) the relevant range of size parameters can be covered [*Mishchenko et al.*, 1996]. This approach is used for retrieving aerosol parameters from AERONET data [*Dubovik et al.*, 2002]. In these applications the irregular particles present in mineral aerosol are represented by an ensemble of oblate and prolate spheroids.

Radiative transfer simulations become more complex when the nonsphericity of the scattering particles is taken into account. The choice of the model shape used, as well as the choice of the shape distribution, are additional degrees of freedom. In practice these choices may be guided by the limitations of the light-scattering method used, by calculation time issues etc. In this thesis we test and validate various methods to simulate light scattering by irregular mineral aerosol. We confront simulated scattering matrices with measurements and evaluate approximative techniques in the context of remote sensing.

4.4 Impact of laboratory measurements

The scattering matrices $\mathbf{F}$ of various mineral aerosol samples have been measured as a function of the scattering angle [*Volten et al.*, 2001]. The experimental setup depicted in Figure 4.2 is called a nephelometer. The nephelometer used by *Volten et al.* [2001] is unique in the sense that all 16 elements of the scattering matrix are measured accurately. Conventional nephelometers measure only the element F_{11}; in some cases the elements F_{12} and F_{22} are included as well. The value of measuring all elements is that the resulting scattering matrices can be used in vector radiative transfer simulations including both the intensity and the polarization of multiply-scattered light. The matrix elements F_{ij} are measured as a function of the scattering angle Θ in the range from 5° to 173°. A total of about 15 samples with different size distributions and refractive indices have been measured at the wavelengths $\lambda = 632.8$ nm and $\lambda = 441.6$ nm [*Volten et al.*, 2005]. A feldspar and a quartz sample originate from ground material from bulk crystals. Various clay and a loess sample originate from natural sedimentation sites. The measured samples further include various volcanic ash samples etc. The compilation of a purely experimental reference database that could be used in remote sensing is inhibited by the small number of samples measured that cover only a limited range of parameters. Furthermore, the experiment does not include the measurement of the cross sections of scattering and absorption.

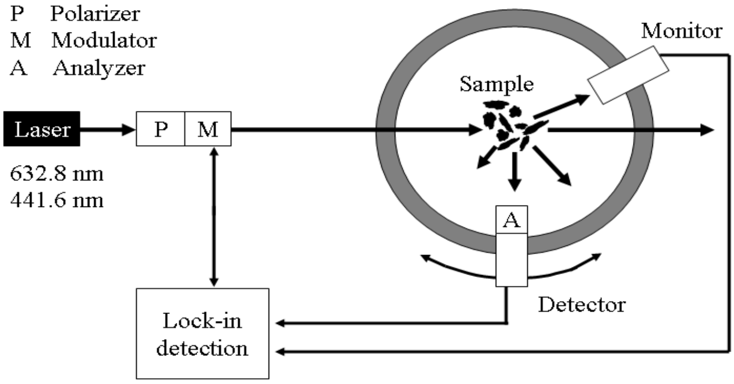

Figure 4.2: Optical setup of the nephelometer.

The aim of the work presented in this thesis is to improve the knowledge of the light scattering properties of atmospheric mineral dust aerosol. In particular we aim at the ability to model the light scattering properties of irregular mineral aerosol as a function of the refractive index, the size distribution, and the particle shape. To this end, we exploit the data from this light scattering experiment. The intended strategy is as follows: Firstly, the measurements are evaluated relative to each other in order to determine the dependence of the measured scattering matrix on the properties of the dust samples. Secondly, techniques used for the simulation of the light scattering properties of irregular mineral dust are tested and evaluated based on the measurements. A model is identified that reflects the measured light scattering characteristics of the irregular dust samples. Finally, this model is applied to atmospheric radiative transfer simulations and remote sensing of mineral dust aerosol. This strategy requires that the properties of three different ensembles of particles match:

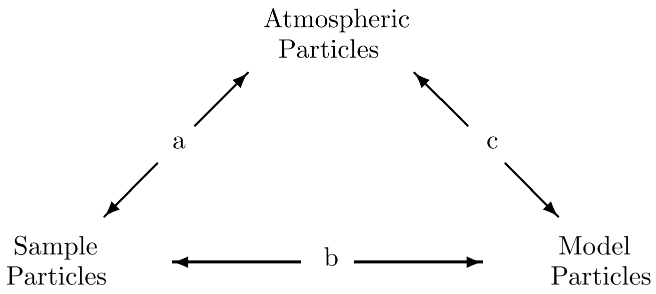

(a) The light scattering measurements provide valuable information about the optical properties of atmospheric mineral aerosol if both the size distribution, and the material properties of the sample particles are representative for those of atmospheric aerosol. The amount of air-borne mineral particles collected in the atmosphere are usually too small for the light scattering measurements. Particle sizes of mineral dust samples from easily accessible sources are often too large. Only a few of the mineral dust samples measured are representative for atmospheric mineral aerosol regarding the size distribution.

In order to apply the measured scattering matrices in radiative transfer simulations the matrix elements $F_{ij}(\Theta)$ have to be extrapolated to the forward and to the backward scattering direction $\Theta = 0°$ and $\Theta = 180°$, which are not included in the measurement. The size distribution has to be known for the extrapolation to the forward scattering direction [*Liu et al.*, 2003]

(b) As discussed in the previous section, most light scattering models for nonspherical particles are only applicable to particles in a limited size range and are restricted to particle shapes with certain symmetries. Currently, one can only cover the full range of particle sizes of mineral dust present in the atmosphere, using a combination of light scattering models under the spheroidal shape approximation. The simulation of light scattering by irregular particles with a large size range is computationally very demanding.

(c) Numerical light scattering models can be validated using measured light scattering properties as reference. Naturally, such a validation can only be achieved if the light scattering model studied is applicable to particles with the properties of the sample particles. Due to the size limitations of light scattering models only a few samples can be used for this kind of validation. For this kind of validation, the size distribution and the refractive index of the mineral samples have to be known.

Category	Method/purpose	used in Ch.
Shape Generation	Gaussian Random Shapes (GRS) [*Muinonen et al.*, 1996]	7
Light scattering properties	Mie code, spherical particles	5, 8
	T-matrix code [*Mishchenko and Travis*, 1998], spheroidal shapes	5, 6, 8
	SScaTT (null-field method) [*Wriedt and Doicu*, 1998], GRS	7
	Discrete Dipole Approximation [*Draine and Flatau*, 1994], GRS	7
	Ray-optics approximation [*Muinonen*, 2000], large GRS	7
	Extension of measured scattering matrices (B. Veihelmann)	8
Inversion	Code for retrieval of aerosol properties derived from the AERONET retrieval code [*Dubovik and King*, 2000]	6
	Linear inversion with regularization retrieval of size distribution (B. Veihelmann)	5
Radiative transfer	Doubling Adding Code [*De Haan et al.*, 1986] incl. polarization and multiple scattering	8

Table 4.1: Numerical codes used in the Chapters 5 to 8.

What can be achieved with the strategy discussed above is therefore confined by the limitations of light scattering models, by the computational resources available, by the properties of the measured samples, and by the accuracy of the knowledge about these properties. We use a variety of advanced and computationally demanding numerical codes for the characterization of the mineral dust samples, for the simulation of the light scattering properties of these samples, and for radiative transfer simulations in an atmosphere containing mineral aerosol. An overview over the numerical codes is given in Table 4.1. A detailed discussion of how these codes are used is given below.

First of all, we characterize the mineral samples as well as possible. The complex refractive indices $m = n - ki$ of the samples are estimated based on the mineral composition. The mineral composition is known exactly only for two mineral samples, which originate from ground bulk crystals, i.e. feldspar and quartz. The samples with a natural origin, like clay and loess, are often mixtures of various minerals with different refractive indices. The imaginary part of the refractive index k is difficult to estimate and may even vary for minerals with the same composition. In many cases we can only judge whether a mineral sample is weakly absorbing (e.g. $k \leq 0.001$) or whether it is strongly absorbing (e.g. $k \geq 0.1$). For most of the samples the real part of the refractive index n is known with an uncertainty of less than 0.1. The estimates for the refractive indices given in Table 4.2 are taken from various sources [*Huffman*, 1977; *Sokolik and Toon*, 1999; *Klein*, 2002].

Table 4.2: Complex refractive indices $m = n - ki$ of mineral dust samples.

	n		k	
Feldspar	1.57	± 0.03	0.0005	± 0.0005
Quartz	1.54	± 0	0.000	± 0
Red clay	1.52	± 0.1	0.001	± 0.001
Green clay	1.52	± 0.1	0.001	± 0.001

The size distributions of the mineral samples are determined from light scattering measurements taken by a laser particle sizer that is located at the Vrije Universiteit Amsterdam. The size distributions have originally been retrieved from intensity measurements of scattered light using diffraction theory. This laser particle-sizing technique has been optimized for the characterization of sediment samples containing particles much larger than the laser wavelength used (632.8 nm). In Chapter 5, we investigate the applicability of this technique for aerosol samples that comprise particles with sizes comparable to the wavelength. We develop linear inversion schemes using either diffraction, Mie theory or T-matrix calculations for spheroidal particles and re-evaluate these light intensity measurements. A smoothness constraint is introduced in order to obtain a stable and meaningful size distribution. Using the concept of the averaging kernel matrix we investigate which part of the solution is determined by the measurement and which part is determined by the smoothness constraint. The size limitation of the particle-sizing technique is determined and the accuracy of the obtained size distributions is evaluated. Furthermore, the systematic errors of simplifying assumptions are quantified.

In Chapter 6, we investigate whether the scattering properties predicted by simulations based on the spheroidal shape approximation are consistent with the measured scattering matrices. A large light scattering database has been generated using a combination of T-matrix and the Geometric Optics calculations for spheroidal particles. This database is used to derive the operational aerosol data product from the global network of ground-based sun and sky radiometers AERONET [*Dubovik et al.*, 2002]. We use this precomputed database for the efficient compilation of scattering matrices of ensembles of spheroidal particles with a given refractive index and a given size and shape distribution. The optimal shape distribution is not known *a priori* and the knowledge of refractive index and the size distribution of the samples may be uncertain. Firstly, we hold constant all parameters, for which *a priori* estimates are available. The aspect ratio distribution is determined using an advanced inversion algorithm that optimizes the agreement between the measured and the simulated scattering matrices [*Dubovik and King*, 2000]. Secondly, we use all parameters as free fit parameters. With this, we give the algorithm the maximum number of degrees of freedom for obtaining an optimal agreement of the measured and the simulated scattering matrices. The agreement of simulated and measured scattering matrices as well as the agreement of retrieved parameters and *a priori* estimates is a measure for the consistency of the spheroidal model with the measurements. This study is done using the measurements of 3 different samples at two different wavelengths. We chose the measured scattering matrices of two mineral samples with a known homogeneous mineral composition and one natural clay sample.

In Chapter 7, a statistical shape model using Gaussian random spheres is tested [*Muinonen et al.*, 1996; *Muinonen*, 2000]. In this model, the morphology of the model particles is based on a statistical shape analysis using SEM images of the true irregular particles. Light scattering by Gaussian random spheres is simulated using the discrete dipole approximation [*Draine and Flatau*, 1994], SScaTT, a light scattering code that is based on the null-field method [*Wriedt and Doicu*, 1998], and the ray optics approximation [*Muinonen*, 2000] for large sizes. We compare the simulated scattering matrices and the simulated cross section with results that are based on the spheroidal shape approximation for individual particle sizes. The Gaussian random sphere model is assessed together with the spheroidal model using a measured scattering matrix of the feldspar sample as reference. This measurement is chosen since the refractive index of feldspar is known quite accurately and the particles in the sample are rather small. This is important due to the size limitations of the light scattering models used. This study is part of a series of three studies dedicated to the validation and testing of shape approximations and their application to atmospheric radiance and flux simulations [*Nousiainen et al.*, 2004; *Kahnert et al.*, 2004].

In Chapter 8, the impact of the shape approximations on polarimetric satellite observations of reflected sunlight over the ocean is investigated using radiative transfer simulations. We focus on the sensitivity of such polarimetric observations to the aerosol optical thickness and the single-scattering albedo. These are the most important aerosol characteristics regarding their climatic relevance. A doubling-adding-code [*De Haan et al.*, 1986] is used for the radiative transfer simulations since it can treat both polarization as well as multiple scattering. Radiative transfer simulations based on the measured scattering matrix of the feldspar sample are used as a reference. To this end, the elements of the measured scattering matrix are extended consistently to the full range of scattering angles. Various spheroidal shape approximations as well as the spherical shape approximation are evaluated in the context of vector radiative transfer simulations and satellite observations.

Bibliography

D'Almeida, G. A., P. Koepke, and E. P. Shettle, *Atmospheric Aerosol Global Climatology and Radiative Characteristics* , Deepak Publ., 1991.

Bian, H., C. S. Zender, Mineral dust and global tropospheric chemistry: Relative roles of photolysis and heterogeneous uptake, *J. Geophys. Res., 108*, ACH 8-1, doi:10.1029/2002JD003143, 2003.

Colarco, P. R., O. B. Toon, J. S. Reid, J. M. Livingstone, P. B. Russell, J. Redemann, B. Schmid, H. B. Maring, D. Savioe, E. J. Welton, J. R. Campbell, B. N. Holben, and R. Levy, Saharan dust transport to the Caribbean Sea during PRIDE: II. Transport, vertical profiles and deposition in simulations of in situ and remote sensing observations, *J. Geophys. Res., 108*, PRD6, 1–16, 2003.

DeMott, P. J., K. Sassen, M. R. Poellot, D. Baumgardner, D. C. Rodgers, S. D. Brooks, A. J. Prenni, and S. M. Kreidenweis, African dust aerosols as atmospheric ice nuclei, *Geophys. Res. Lett., 30*, doi:10.1029/2003GL01740, 2003.

Deuzé, J.-L., F.-M. Bréon, C. Devaux, P. Goloub, M. Herman, B. Lafrance, F. Maignan, A. Marchand, F. Nadal, G. Perry, and D. Tanré, Remote sensing of aerosols over land surfaces from POLDER-ADEOS 1 Polarized measurements *J. Geophys. Res., 106*, 4913–4926, 2001.

Deuzé J.-L., P. Goloub, M. Herman, A. Marchand, G. Perry, D. Tanré, Estimate of the aerosols properties over the ocean with POLDER, *J. Geophys. Res., 105*, 15329–15346, 2000.

Díaz, J. P., F. J. Expósito, C. J. Torres, and F. Herrera, Radiative properties of aerosols in Sahara dust outbreaks using ground-based and satellite data: application to radiative forcing, *J. Geophys. Res., 106* , 18403–18416, 2001.

Dubovik, O., and M. D. King, A flexible algorithm for retrieval of aerosol optical properties from sun and sky radiance measurements, *J. Geophys. Res., 105*, 20673–20696, 2000.

Dubovik, O., B. N. Holben, T. F. Eck, A. Smirnov, Y. J. Kaufman, M. D. King, D. Tanré, and I. Slutsker, Variability of absorption and optical properties of key aerosol types observed in worldwide locations, *J. of the Atmos. Sci., 59*, 590–608, 2002.

Dubovik, O., B. N. Holben, T. Lapyonok, A. Sinyuk, M. I. Mishchenko, P. Yang, I. Slutsker, Non-spherical aerosol retrieval method employing light scattering by spheroids, *Geophys. Res. Lett., 29*, doi:10.1029/2001GL014506, 51-1, 2002.

Draine, B. T., and J. P. Flatau, Discrete-dipole approximation for scattering calculations, *J. Opt. Sc. Am. A, 11*, 1491–1499, 1994.

Garrett, T. J., L. M. Russell, V. Ramaswamy, S. F. Maria, and B. J. Huebert, Microphysical and radiative evolution of aerosol plumes over the tropical North Atlantic Ocean, *J. Geophys. Res., 108*, doi:10.1029/2002JD002228, AAC11, 1-16, 2002.

Geogdzhayev, I. V., M. I. Mishchenko, L. Liu , and L. Remer, Global two-channel AVHRR aerosol climatology: effects of stratospheric aerosols and preliminary comparisons with MODIS and MISR retrievals, *J. Quant. Spectrosc. Radiat. Transfer, 88*, 1-3, 2004.

Ghan, S., R. Easter, J. Hudson, and F.-M. Bréon, Evaluation of aerosol indirect radiative forcing in MIRAGE, *J. Geophys. Res., 106*, 5317-5334, 2001.

Ghan, S., N. Laulainen, R. Easter, R. Wagener, S. Nemesure, E. Chapman, Y. Zhang, and R. Leung, Evaluation of aerosol direct radiative forcing in MIRAGE, *J. Geophys. Res., 106*, 5295-5316, 2001.

De Haan, J. F., P. B. Bosma, and J. W. Hovenier, The adding method for multiple scattering calculations of polarized light, *Astron. Astrophys., 183*, 371–391, 1986.

Haywood, J. M., and O. Boucher, Estimates of the direct and indirect radiative forcing due to tropospheric aerosols: a review, *Reviews of Geophysics, 38(4)*, 513–543, 2000.

Haywood, J. M., P. N. Francis, M. D. Glew, and J. P. Taylor, Optical properties and direct radiative effect of Saharan dust: A case study of two Saharan dust outbreaks using aircraft data, *J. Geophys. Res., 106*, 18417–18430, 2001.

Heintzenberg, J., C. D. Covert, and R. van Dingen, Size distribution and chemical composition of marine aerosols: a compilation and review, *Tellus-Series B, Chem. Phys. Met., 52B(4)*, 1104–1122, 2000.

Holben, B. N. and coautors, A federated instrument network and data archive for aerosol characterization, *Remote Sens. Environ., 66*, 1–16, 1998.

Huffman, D. R., The interaction of light with a small-particle system, *Adv. Phys., 26*, 129-130, 1977.

Husar, R. B., J. M. Prospero, and L. L. Stowe, Characterization of tropospheric aerosol over the ocean with the NOAA Advanced Very High Resolution Radiometer optical thickness operational product, *J. Geophys. Res., 102*, 16889–16909, 1997.

Ichocu, C., Y. J. Kaufman, L. A. Remer, and R. Levy, Global aerosol remote sensing from MODIS, *Adv. in Space Res., 34*, 820–827, 2004.

Kahn, R., R. West, D. McDonald, B. Rheingans, and M. I. Mishchenko, Sensitivity of multi-angle remote sensing observations to aerosol sphericity, *J. Geophys. Res., 102*, 16861–16870, 1997.

Kahnert, F. M., and A. Kylling, Radiance and flux simulations for mineral dust aerosols: Assessing the error due to using spherical or spheroidal model particles, *J. Geophys. Res., 109*, doi:10.1029/2003JD004318, 2004.

Kahnert, F. M., T. Nousiainen and B. Veihelmann, Spherical and Spheroidal model particles as an error source in aerosol climate forcing and radiation computations: a case study for feldspar aerosols, *J. Geophys. Res.*, accepted

Kaufman, Y. J., D. Tanré, and O. Bouché, A satellite view of aerosols in the climate system, *Nature, 419*, 215–223, 2002.

King, M., Y. J. Kaufman, D. Tanré, and T. Nakajima, Remote sensing of tropospheric aerosols from space: Past, present, future, *Bull. Am. Meteor. Soc., 80*, 2229–2259, 1999.

Kinne, S., and R. Pueschel, Aerosol radiative forcing for Asian continental outflow, *Atmos. Environment, 35*, 5019–5028, 2001.

Klein, C., *Manual of Mineral Science, 22nd ed.*, John Wiley, New York, 2002.

Krueger, B. J., V. H. Grassian, A. Laskin, and J. P. Cowin, The transformation of solid atmospheric particles into liquid droplets through heterogeneous chemistry: Laboratory insights into the processing of calcium containing mineral dust aerosol in the troposphere, *Geophys. Res. Lett., 30*, doi:10.1029/2002GL016563, 2003.

Li-Jones, X., H. B. Maring, and J. M. Prospero, Effect of relative humidity on light scattering by mineral dust aerosol as measured in the marine boundary layer over the tropical Atlantic Ocean, *J. Geophys. Res., 103*, 31113-31122, doi:10.1029/98JD01800, 1998.

Liu, L., M. I. Mishchenko, J. W. Hovenier, H. Volten and O. Muñoz, Scattering matrix of quartz aerosols: comparison and synthesis of laboratory and Lorenz-Mie results, *J. Quant. Spectrosc. Radiat. Transfer, 79–80*, 911–920, 2003.

Mahowald, N. M., and L. M. Kiehl, Mineral aerosol and cloud interaction, *Geophys. Res. Lett., 30*, doi:10.1029/2002GL016762, 2003.

Maring, H., D. L. Savoie, M. A. Izaguirre, L. Custals, and J. S. Reid, Mineral dust aerosol size distribution change during atmospheric transport, *J. Geophys. Res., 108*, doi:10.1029/2002JD002536, PRD8 1–6, 2003.

Min, M., J. W. Hovenier, and A. de Koter, Scattering and absorption cross sections for randomly oriented spheroids of arbitrary size, *J. Quant. Spectrosc. Radiat. Transfer, 79*, 939-+, 2003

Mishchenko, M. I., Light scattering by randomly oriented axially symmetric particles, *J. Opt. Am. A, 8*, 871–882, 1991.

Mishchenko, M. I., A. A. Lacis, B. E. Carlson, and L. D. Travis, Nonsphericity of dust-like tropospheric aerosols: implications for aerosol remote sensing and climate modeling, *Geophys. Res. Lett., 22*, 1077–1080, 1995.

Mishchenko, M. I., L. D. Travis, and A. Macke, Light scattering by nonspherical particles: An overview, *Proceedings of the International Radiation Symposium*, edt. W. L. Smith and K. Stamnes, 1996.

Mishchenko, M. I., and L. D. Travis, Capabilities and limitations of a current FORTRAN implementation of the T-matrix method for randomly oriented, rotationally symmetric scatterers, *J. Quant. Spectrosc. Radiat. Transfer, 60*, 309-324, 1998

Mishchenko, M. I., L. D. Travis, and A. A. Lacis, Book, *Scattering, Absorption, and Emission of Light by Small Particles*, NASA Goddard Institute for Space Studies, New York, Cambridge University Press, 2002.

Mishchenko, M. I., B. Cairns, J. E. Hansen, L. D. Travis, R. Burg, Y. J. Kaufman, J. Vanderlei Martins, and E. P. Shettle, Monitoring of aerosol forcing of climate from space: analysis of measurement requirements, *J. Quant. Spectrosc. Radiat. Transfer, 88*, 149–161, 2004.

Muinonen, K., T. Nousiainen, P. Fast, K. Lumme and J. I. Peltoniemi, Light scattering by Gaussian Random Particles: Ray optics approximation, *J. Quant. Spectrosc. Radiat. Transfer, 55*, 577–601, 1996.

Muinonen, K. , Light scattering by stochastically shaped particles, chapter in *Light scattering by Nonspherical Particles*, edited by M. I. Mishchenko, J. W. Hovenier, and L. D. Travis, pp. 323–352, Academic Press, San Diego, 2000.

Muñoz, O., H. Volten, J. F. de Haan, W. Vassen , and J. W. Hovenier, Experimental determination of scattering matrices of randomly-oriented fly ash and clay particles at 442 and 633 nm, *J. Geophys. Res., 106*, 833–844, 2001.

Muñoz, O., H. Volten, J. W. Hovenier, B. Veihelmann, W. J. van der Zande, and L. B. F. M. Waters, Scattering matrices of volcanic ash particles of Mount St. Helens, Redoubt, and Mount Spurr Volcanoes, *J. Geophys. Res., 109*, doi:10.1029/2004JD004684, D16201, 1-16, 2004.

Nousiainen, T., and K. Vermeulen, Comparison of measured single-scattering matrix of feldspar particles with T-matrix simulations using spheroids, *J. Quant. Spectrosc. Radiat. Transfer, 79-80*, 1031–1042, 2003.

Nousiainen, T., F. M. Kahnert, and B. Veihelmann, Light scattering modeling of small feldspar particles using simplified shapes, *J. Quant. Spectrosc. Radiat. Transfer*, accepted.

Penner, P. E., X. Dong, Y. Chen, Observational evidence of a change in radiative forcing due to the indirect aerosol effect, *Nature, 427*, 231–234, 2004.

Penner, J. E., R. E. Dickinson, and C. A. O'Neill, Effects of aerosols from biomass burning on the global radiation budget, *Science, 256*, 1432–1433, 1992.

Penner, J. E., A Comparison of Model- and Satellite-Derived Aerosol Optical Depth and Reflectivity, *J. Atm. Sci., 59*, 441–460, 2002.

Purcell, E. M., and C. R. Pennyacker, Scattering and Absorption of Light by Nonspherical Dielectrical Grains, *Astrophysical J., 186*, 705–714, 1973.

Querol, X., A. Alastuey, A. Lopez-Soler, E. Mantilla, and F. Plana, Mineral composition of atmospheric particulates around a large coal-fired power station *Atmos. Environ., 30*, 3557–3572, 1996.

Quijano, A. L, I. N. Sokolik, O. B. Toon, and O. Brian, Radiative heating rates and direct radiative forcing by mineral dust in cloudy atmospheric conditions *J. Geophys. Res., 105*, 12207–12220, 2000.

Roedel, W., *Physik unserer Umwelt: Die Atmosphäre*, Springer Verlag, Berlin, 1992.

Sassen, K., P. J. DeMott, J. M. Prospero, and M. R. Poellot, Saharan dust storms and indirect aerosol effects on clouds: CRYSTAL-FACE results, *Geophys. Res. Lett., 30*, doi:10.1029/2003GL017371, 35, 1–4, 2003.

Seinfeld, J. H., and S. N. Pandis, *Atmospheric chemistry and physics*, John Wiley, New York, 1998.

Sokolik, I. N., and O. B. Toon, Direct radiative forcing by anthropogenic airborne mineral aerosols, *Nature, 381*, 681–683, 1996.

Sokolik, I. N., and O. B. Toon, Incorporation of mineralogical composition into models of the radiative properties of mineral aerosol from UV to IR wavelengths, *J. Geophys. Res., 104*, 9423–9444, 1999.

Song-Miao, F., L. W. Horowitz, H. L. II, and W. J. Moxim, Impact of air pollution on wet deposition of mineral dust aerosols, *Geophys. Res. Lett., 31*, doi:10.1029/2003GL018501, L02104, 1–4, 2004.

Tanré, D., Y. J. Kaufman, M. Herman, and S. Mattoo, Remote sensing of aerosol properties over oceans using the MODIS/EOS spectral radiances, *J. Geophys. Res., 102*, 16971–16988, doi:10.1029/96JD03437, 1997.

Tanré, D., Y. J. Kaufman, B. N. Holben, B. Chatenet, A. Karnieli, F. Lavenu, L. Blarel, O. Dubovik, L. A. Remer, and A. Smirnov, Climatology of dust aerosol size distribution and optical properties derived from remotely sensed data on the solar spectrum, *J. Geophys. Res., 106*, 18205–18217, 2001.

Tegen, I., A. A. Lacis, and I. Fung, The influence on climate forcing of mineral aerosols from disturbed soils, *Nature, 380*, 419–422, 1996.

Tegen, I., and A. A. Lacis, Modeling of particle size distribution and its influence on the radiative properties of mineral dust aerosol, *J. Geophys. Res., 101*, 19237–19244, 1996.

Twomey, S., The Influence of Pollution on the short-wave albedo of clouds, *J. Atmos. Sci., 34*, 1149–1152, 1977.

Volten, H., O. Muñoz, E. Rol, J. F. de Haan, W. Vassen, J. W. Hovenier, K. Muinonen, and T. Nousiainen, Scattering matrices of mineral particles at 441.6 nm and 632.8 nm., *J. Geophys. Res., 106*, 17375–17401, 2001.

Volten, H., O. Muñoz, J. W. Hovenier, J. F. de Haan, W. Vassen, W. J. van der Zande, and L. B. F. M. Waters, WWW scattering matrix database for small mineral particles at 441.6 nm and 632.8 nm, *J. Quant. Spectrosc. Radiat. Transfer, 90*, 191-206, 2005.

Wriedt, T., and A. Doicu, Formulation of the extended boundary condition method for three-dimensional scattering using the method of discrete sources, *J. Modern Optics, 45*, 199–214, 1998.

Young, P., and K. N. Liou, Geometric-optics-integral-equation method for nonspherical ice crystals, *Appl. Opt., 35*, 6568–6584, 1996.

Zender, C. S., D. Newman, and O. Torres, Spatial heterogeneity in aeolian erodibility, uniform, topographic, geomorphic and hydrologic hypothesises, *J. Geophys. Res., 108*, AAC2, 1–15, doi:10.1029/2002JD003039, 2003.

Zhang, J., and S. A. Christopher, Longwave radiative forcing of Saharan dust estimated from MODIS, MISR, and CERES observations on TERRA, *Geophys. Res. Lett., 30*, ASC2, 1–4, doi:10.1029/2003GL018479, 2003.

Chapter 5

Size distribution of mineral aerosol

Abstract

A widely-used approach to determine the size distribution of small particles is to measure the intensity of singly-scattered light at various scattering angles. An accurate light scattering model is required for retrieving the size distribution from the measured intensities. We derive the size distribution of semi-transparent and irregularly-shaped mineral aerosol samples using the light scattering measurements of a laser particle sizer. We compare the results based on diffraction theory, Mie calculations for spheres with various refractive indices, and T-matrix calculations for spheroidal particles. We identify systematic errors of the retrieved size distribution when the semi-transparent and non-spherical properties of the particles are neglected. A variety of synthetic measurements is generated based on light scattering simulations for parameterized size distributions of spherical or spheroidal model shapes. With this we investigate the impact of the simplifying approximations that are implied when the effective radius and the variance of a parameterized size distribution are retrieved using the diffraction model or Mie theory.

5.1 Introduction

The size distribution of mineral aerosol plays a central role in this thesis. The size distribution of an ensemble of particles gives the number of particles as a function of the particle size. As discussed in the previous chapter, many aerosol properties depend on the sizes of the particles. Numerical models are used to simulate light scattering by irregular particles. These light scattering models can be validated using the light scattering measurements introduced in the previous chapter. This kind of validation requires that the size distribution of the reference samples is known. The size distribution of the samples has to be known as well in order to interpret differences in the light scattering measurements of different samples. In order to apply the measured scattering matrices in radiative transfer simulations, the measured matrix elements $F_{ij}(\Theta)$ have to be extrapolated to the forward and to the backward scattering direction $\Theta = 0°$ and $\Theta = 180°$, which are not included in the measurement. For the extrapolation to the forward scattering direction the size distribution has to be known [*Liu et al.*, 2003].

The size distribution of an ensemble of particles can be determined with various methods. Particles can be measured and counted directly, e.g. using a scanning electron microscope (SEM). However, the number of observed objects is usually too small to obtain statistical significance, especially when the size distribution is broad and many different magnifications have to be used. Aerodynamic and hydrodynamic methods are based on the fact that the mass is proportional to the cube and the viscous drag is proportional to the square of the linear dimensions of a particle. In this chapter we focus on a commonly-used and powerful particle-sizing technique using intensity measurements of singly-scattered light. This technique is based on the fact that light scattering close to the forward-scattering direction is sensitive to size but insensitive to refractive index and particle shape. The same principle is used for the measurement of the size distribution of atmospheric aerosol using ground-based sky radiance measurements in the aureole, i.e. in viewing geometries close to the sun.

The size distributions of the samples studied by *Volten et al.* [2001] have been measured using a laser particle sizer (*Fritsch Analysette 22-E*) located at the Vrije Universiteit Amsterdam, with the so-called diffraction method. This method, which has been developed for the characterization of sediment samples containing particles much larger than the wavelength, assumes that light scattering can be described by Fraunhofer diffraction from round non-transparent discs. The diffraction method is a commonly-used approach [e.g. *Kocifaj and Držík*, 1996; *Santer and Herman*, 1983]. Nevertheless, the light scattering properties of real particles differ from the predictions of the diffraction theory. This is especially true for weakly-absorbing irregularly-shaped particles with sizes comparable to the wavelength, which are present in the mineral aerosol samples measured. We determine the impact of the low absorption and the non-sphericity on the retrieved size distributions.

The size distribution and its discrete representation used in this study are introduced in Section 5.2. The concept of laser particle-sizing is discussed next (5.3). The optical setup of a typical laser particle sizer is sketched briefly. A forward model is developed that links the size distribution of a sample to the measured intensity signal. We discuss various forward models and the inversion schemes that are used to derive the size distribution from the measured intensities. In Section 5.4 we compare the size distribution of various samples that are retrieved based on diffraction theory, Mie calculations for spheres with various refractive indices, and on T-matrix calculations for spheroidal particles. The discrepancies of the size distributions are discussed and systematic errors are identified. The effective radius and the variance of a parameterized log-normal size distribution can be retrieved directly for the measurement using a non-linear least-squares fit routine. Naturally, this is appropriate only if the true size distribution is mono-modal. Based on a range of synthetic measurements, systematic errors are determined that are encountered when the diffraction method is applied to strongly absorbing and non-absorbing spherical particles. In a similar way, we quantify the systematic errors that are encountered when Mie theory is applied to non-spherical particles.

5.2 Size distribution

The shapes of mineral dust particles are usually irregular. This poses a general problem for particle-sizing. Sizing techniques that are applicable to particle ensembles are always based on simplifying assumptions concerning the particle shape. One obvious reason is that the exact shape of all particles in a very large ensemble cannot be taken into account explicitly. Furthermore, the laser particle-sizing method discussed here is based on numerical light scattering models that require a simplified shape description. In the following, we will refer to the size of a particle as the radius r of a sphere with the same volume. Often it is convenient to use the size parameter $x = 2\pi r/\lambda$, which stresses the fact that the optical properties of small particles depend strongly on the ratio of the particle size and the wavelength λ.

The size distribution of an ensemble of spherical particles can be described by the distribution function $\nu(r) = dN/dr$ defining the number of particles N with radii r between r_1 and r_2

$$N = \int_{r_1}^{r_2} \nu(r)\ dr \tag{5.1}$$

The effective radius

$$r_{\text{eff}} = \frac{1}{G} \int_0^\infty r\pi r^2 \nu(r)\ dr \tag{5.2}$$

and the effective variance

$$v_{\text{eff}} = \sigma^2_{\text{eff}} = \frac{1}{G\ r^2_{\text{eff}}} \int_0^\infty (r - r_{\text{eff}})^2 \pi r^2 \nu(r)\ dr \tag{5.3}$$

with

$$G = \int_0^\infty \pi r^2 \nu(r)\ dr. \tag{5.4}$$

are the first and second moments of the size distribution $\nu(r)$ [*Hansen and Travis*, 1974]. Since the size distributions considered in this study are rather broad, it is convenient to use the logarithmic number distribution $\tilde{\nu}(R)$ as a function of the the log-radius $R = \log_{10}(r)$

$$\tilde{\nu}(R) = \frac{dN}{d\log_{10}(r)} = r\ \log(10)\ \nu(r). \tag{5.5}$$

We introduce the vector **n**, which defines the normalized and discrete form of the logarithmic number distribution. The elements of **n** are

$$n_i = \frac{1}{\int_{-\infty}^{+\infty} \tilde{\nu}\ dR} \int_{R_i}^{R_{i+1}} \tilde{\nu}(R)\ dR. \tag{5.6}$$

The surface distribution **s** with

$$s_i = \frac{1}{\int_{-\infty}^{+\infty} \pi r^2 \tilde{\nu}\ dR} \int_{R_i}^{R_{i+1}} \pi r^2 \tilde{\nu}(R)\ dR. \tag{5.7}$$

describes the fraction of the ensemble surface that is present in the size range from R_i to R_{i+1}. The surface distributions $\mathbf{s}$ is convenient for laser particle sizing since the light scattering cross section of small particles (with size parameters $x \geq 10$) scales with the particle surface. In natural ensembles of mineral particles, small particles occur much more frequently than larger ones. Natural size distributions of dust aerosol [see e.g. *Dubovik et al.*, 2002] are thus very steep and may cover many orders of magnitude when being expressed in terms of a number distribution. This can cause problems in the numerical representation of the number distribution $\nu(r)$ or $\tilde{\nu}(R)$. The surface distribution is less steep and is therefore preferred.

5.3 Laser particle-sizing

The size distributions of the feldspar, the quartz and the red clay sample introduced in the previous chapter (Chapter 4) have been determined using a laser particle sizer. The optical setup of this kind of apparatus is sketched in Figure 5.1. A widened He-Ne laser with a wavelength of $\lambda = 632.8$ nm is focused on a detector screen. The laser light is directed through a dilute cloud of particles that are suspended in water. The suspension in water rather than air facilitates the control of the amount of dust in the beam. The scattered light is focused on a screen and detected by a series of concentric ring shaped detectors. The radii of the detector rings are chosen to be equidistant on a logarithmic grid. The logarithm of the detector area increases with a constant increment. This choice facilitates the size retrieval as will be discussed later in this section.

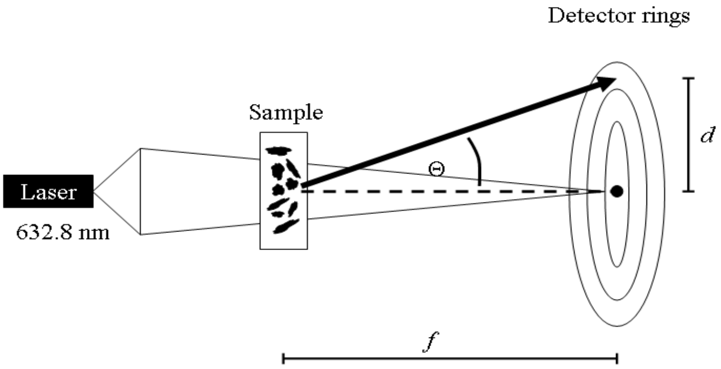

Figure 5.1: Optical setup of the laser particle sizer.

The detectors cover a range of scattering angles from a fraction of a degree to more than 60°. The cloud of particles is optically thin, so that multiple scattering is negligible. Since the laser beam is narrow the radius on the screen d is related to the scattering angle by $\tan(\Theta) = d/f$. The variable f represents the distance between scatterer and screen. The series of measured intensity values will in the following be referred to as the observation vector $\mathbf{y}$. In order to retrieve the size distribution, a model is needed that relates the observation $\mathbf{y}$ with the surface distribution $\mathbf{s}$.

5.3.1 Forward model

In this section we develop a forward model for the simulation of the measured intensity as a function of the size distribution of the sample. The measured intensity of one detector pixel depends on the pixel size and the amount of light scattered into the direction of the detector. The intensity of light that is singly-scattered by an ensemble of randomly oriented particles depends only on the scattering angle Θ. The scattering angle $\Theta = 0$ denotes forward scattering. The directionality of singly-scattered light is described by the phase function $P(\Theta)$. The scattering cross section c describes the probability of a single-scattering process. Both the phase function and the scattering cross section depend on the particle size.

The intensity y_i measured by the i-th detector is calculated by an integration of the phase function $P(\Theta)$ over the solid angle Ω_i of the i-th detector. The contributions of all j sizes to this intensity are weighted with the scattering cross section c_j and the relative weight n_j of the size distribution defined by Eq. (5.6). The scattering efficiency Q is defined as the ratio of the scattering cross section and the geometrical cross section. When the scattering efficiency $Q_j = c_j/(\pi r_j^2)$ and the surface distribution $\mathbf{s} = \pi r^2 \mathbf{n}$ (Eq. (5.7)) are used the forward model can be written as

$$y_i = \sum_j Q_j \; s_j \int_{\Omega_i} P_j(\Theta) d\Omega \quad \cdot const. \tag{5.8}$$

The forward model is linear and can be written in matrix notation as

$$\mathbf{y} = \mathbf{K}\mathbf{s} \cdot const. \tag{5.9}$$

The constant factor in Eq. (5.8) and (5.9) depends on the total amount of mineral dust measured, the light intensity of the laser, the absolute size of the detectors, the detector gain etc. We may drop this factor since only the normalized size distributions $\mathbf{s}$ are needed in what follows. The elements $K_{ij} = \partial y_i / \partial s_j$ represent the sensitivity of the measured intensity of the i-th detector with respect to the j-th value of the surface distribution. The j-th column of $\mathbf{K}$ is proportional to the measured intensity vector $\mathbf{y}$ for a narrow size distribution that peaks at the j-th size only. The phase function $P(\Theta)$ and the scattering cross section c depends on the light scattering model used. As a consequence, the Jacobian matrix $\mathbf{K}$ of the forward model as well as the retrieved size distribution depend on the choice of the model describing the light scattering. In the following we highlight differences between various light scattering models.

The phase function and the scattering cross section can be calculated in various ways. Mie theory can be applied to spherical particles. We test models based on Mie scattering for spheres with various refractive indices. We use a refractive index of $1.57-0.5$i for strongly-absorbing spheres, 1.57-0i for non-absorbing spheres. Furthermore we consider spheres with the refractive indices $1.57-0.0005$i, $1.54-0$i, and $1.52-0.001$i as estimates for the feldspar, the quartz, and the red clay sample respectively. These estimates of the refractive indices in vacuum are based on data from various sources [*Huffman*, 1977; *Sokolik and Toon*, 1999; *Klein*, 2002]. Note that the surrounding medium in the particle sizer is water, for which the real part of the refractive index is 1.33. The light scattering calculations used in the forward model are therefore based on relative values of the real part of the refractive index. T-matrix calculations can be used for spheroidal particles [*Mishchenko et al.*, 2000]. We consider an ensemble of non-absorbing prolate and oblate spheroids including aspect ratios ranging from 0.5 to 2. Due to limitations of the numerical light scattering code we are restricted to particles with volume equivalent radii $r < 10$ μm at a wavelength of 632.8 nm [*Mishchenko and Travis*, 1998]. This light scattering model will be referred to as the spheroidal model. In laser particle-sizing techniques, light scattering is often approximated by Fraunhofer diffraction from round non-transparent discs with the radius r. The phase function $P(\Theta)$ can be derived from the well-known intensity distribution of Fraunhofer interference $I_{\mathrm{Fr}}(x,\Theta)$, measured on a screen in the far field [e.g. *Born and Wolf*, 1999]

$$I_{\mathrm{Fr}}(x,\Theta) \propto x^2 \left(\frac{J_1(x\sin(\Theta))}{x\sin(\Theta)}\right)^2 . \tag{5.10}$$

The function J_1 denotes the first order Bessel function of the first kind, x is the size parameter $2\pi r/\lambda$. The diffraction cross section is identical to the geometrical cross section of the disc $c = \pi r^2$. This approximation will be referred to, in the following, as the diffraction model.

In Figure 5.2, the phase functions of discs with various sizes ($x = 1, 10$ and 100) are shown. For demonstrative purposes, the phase functions are normalized to 1 at $\Theta = 0$. We compare the phase functions based on diffraction (solid), Mie scattering by strongly-absorbing (dashed) and non-absorbing spheres (dotted). For these calculations a refractive index of 1.18 is assumed. This a typical value for the relative refractive index of minerals like feldspar or quartz in water. The phase functions of these models are similar and have an important property in common: The width of the intensity peak centered at $\Theta = 0°$ is inversely proportional to the linear dimensions of the scattering particles. Due to this property it is possible to distinguish particles with different sizes in light scattering experiments. We note differences between the phase functions derived from diffraction theory and from Mie theory, especially for small particles with $x = 1$.

The scattering efficiency Q of strongly-absorbing spheres (solid circles), of non-absorbing spheres (empty circles) and of non-absorbing spheroids (dots) are shown as a function of the particle size (Fig. 5.3). The cross section of diffraction is identical to the geometrical cross section of the discs. The scattering efficiency that is attributed to the diffraction model (+) takes therefore the constant value unity. In contrast to two-dimensional discs,

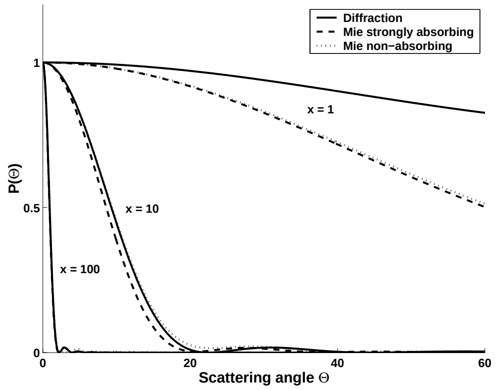

Figure 5.2: Phase function $P(\Theta)$ for diffraction (solid) and Mie scattering by strongly-absorbing (dashed) and non-absorbing spheres (dotted). The intensity is normalized to 1 at $\Theta = 0°$. The sizes of the spheres are given in terms of the size parameter $x = 2\pi r/\lambda$.

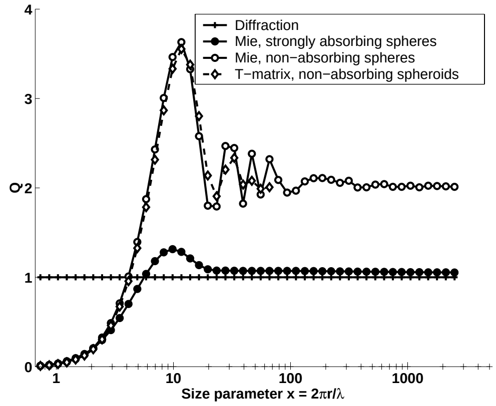

Figure 5.3: Scattering efficiency Q for diffraction (crosses), from Mie caclulations for strongly absorbing spheres (solid circles) and non-absorbing spheres (empty circles), and from T-matrix calculations for non-absorbing spheriods (empty diamonds).

the scattering efficiency of spherical and non-spherical particles is clearly size-dependent. The scattering efficiency has very small values ($Q \ll 1$) at $x = 1$, increases to a maximum at $x \approx 10$, and after some oscillations, drops to a constant value. For non-absorbing spheres and spheroids the maximum scattering efficiency has a value of about 3.6 and the oscillations are very pronounced. A maximum of this amplitude is found as well in the scattering efficiency of particles with other shapes such as the weakly-absorbing Gaussian random spheres presented in Chapter 7 (not shown). A value of about 2 is reached for size parameters $x \geq 200$ in the geometric optics domain (see Chapter 4). For strongly-absorbing particles the maximum scattering efficiency is lower ($Q \approx 1.4$) and a constant value of $Q \approx 1$ is reached for size parameters $x \geq 2$. Measurements of the extinction efficiency of quartz and diamond dust samples as well as other powdery substances indicate that the scattering efficiency of natural irregular particles exhibit the characteristic first maximum shown by the spherical model and the spheroidal model [*Bohren and Huffmann*, 1983, sec. 11.7.3 and references therein].

The Jacobian matrix $\mathbf{K}$ of the forward model is constructed from the scattering efficiencies and the phase functions. In Figure 5.4 we show the Jacobian matrix of (a) the diffraction model $\mathbf{K}_\mathrm{a}$, and the models for (b) strongly-absorbing spheres $\mathbf{K}_\mathrm{b}$, (c) non-

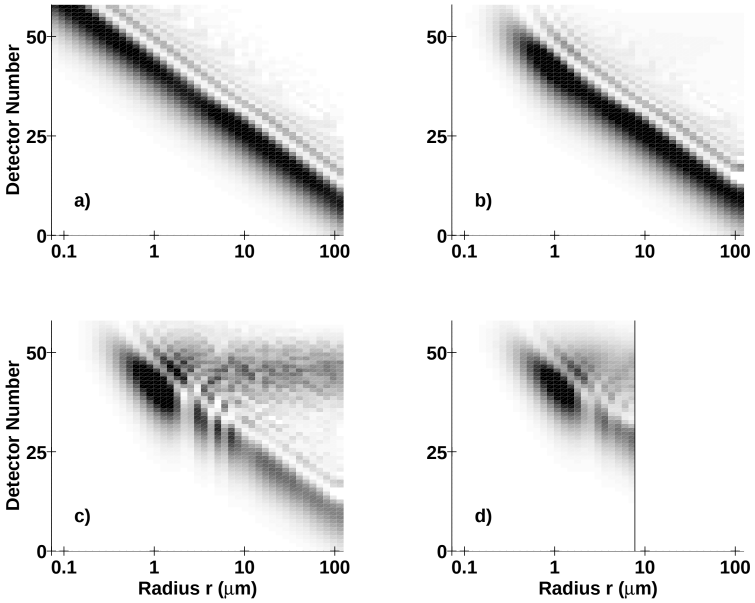

Figure 5.4: Representation of the Jacobian matrix of the linearized forward model based on (a) diffraction theory, (b) Mie theory for strongly absorbing spheres, (c) non-absorbing spheres, and (d) T-matrix calculations for a mixture of non-absorbing oblate and prolate spheroids. High values of the matrix elements K_{ij} are depicted as dark gray, low values are depicted as light gray levels. Further explanations are given in the text.

absorbing spheres $\mathbf{K}_\mathrm{c}$, and (d) non-absorbing spheroids $\mathbf{K}_\mathrm{d}$. The element (0,0) of the matrices is depicted at the lower left corner of each graph. This element $K_{00} = \partial y_0 / \partial s_0$ represents the sensitivity of the innermost detector ring with respect to the surface distribution at the smallest particle size. Matrix elements with a large amplitude are depicted in dark gray. The gray scales used in (a-d) are not identical. Note that the measured intensity vectors, i.e. the column vectors $K_{i1}, K_{i2}, ...$ have low values at the inner detector rings even though the phase function generally has the largest values close to $\Theta = 0°$. This is due to the fact that the detector areas increase logarithmically with increasing detector number i.

The Jacobian matrix of the diffraction model $\mathbf{K}_\mathrm{a}$ has a very simple structure. First of all, we note that the inner detectors are sensitive to large particles, while the outer detectors are more sensitive to small particles. This is because the phase function becomes more forward-peaked with increasing particle size. We note as well, that the columns vectors $K_{i1}, K_{i2}, ...$ have a very similar shape with one global maximum and a few smaller local maxima. The column vectors of different particle sizes are simply shifted with respect to each other. This can be explained as follows. Both the particles sizes of the size distribution $\mathbf{n}$ as well as the detector areas are chosen to be equidistant on a logarithmic grid. Since the width of the diffraction pattern is proportional to r^{-1}, the slope of the line connecting the maxima of all columns is constant. The range of scattering angles used for the retrieval is chosen such that the matrix is nearly diagonal. The geometry of the detector rings thus facilitates the inversion of the matrix and thus the retrieval of the size distribution. The Jacobian matrix of the model for strongly-absorbing spheres $\mathbf{K}_\mathrm{b}$ is similar to the Jacobian matrix of the diffraction model $\mathbf{K}_\mathrm{a}$ for particle sizes with $x > 10$. For smaller particle sizes, the amplitudes of the column vectors of $\mathbf{K}_\mathrm{b}$ decrease with decreasing particle size, which is not the case for $\mathbf{K}_\mathrm{a}$. This difference is due to the discrepancy in the scattering efficiency of the models shown in Fig. 5.3. The pronounced size-dependence of the scattering efficiency of the model for non-absorbing spheres is reflected in the amplitudes of the column vectors of $\mathbf{K}_\mathrm{c}$. As compared to $\mathbf{K}_\mathrm{b}$, the elements of $\mathbf{K}_\mathrm{c}$ (non-absorbing spheres) that are related to the detectors 40 to 50 have large values. This is related to the more pronounced sidewards scattering of non-absorbing spheres. The spheroidal model is limited in particle size due to the convergence limit of the T-matrix code. In the size range $x = 1$ to 100 the Jacobian matrices for non-absorbing spheroids $\mathbf{K}_\mathrm{d}$ and non-absorbing spheres $\mathbf{K}_\mathrm{c}$ are similar. Note the similarity in the resonant structures that are revealed by the wavy nature of the graphs.

5.3.2 Inversion

The forward model $\mathbf{y} = \mathbf{K}\mathbf{s}$, derived in the previous section, is clearly linear. The retrieval of the size distribution is equivalent to finding an inverse matrix $\mathbf{D}$ to the matrix $\mathbf{K}$ that relates a size distribution to a given measurement

$$\mathbf{s} = \mathbf{D}\mathbf{y}. \tag{5.11}$$

The number of sizes (n) is usually chosen to be smaller than the number of detectors (m). In this case, the matrix $\mathbf{K}$ is not square and the simple inverse matrix $\mathbf{K^{-1}}$ is not defined. A least-squares solution can be derived using the maximum likelihood method. This approach is based on the assumption that errors are Gaussian distributed which can be supported by minimum entropy considerations [e.g. *Rodgers*, 2000]. The generalized inverse matrix $\mathbf{D}$ is then

$$\mathbf{D} = (\mathbf{K^T S_y^{-1} K})^{-1} \mathbf{K^T S y^{-1}}. \tag{5.12}$$

The superscripts ^{T} and $^{-1}$ denote the transpose and the inverse of the matrix, respectively. The matrix $\mathbf{S_y}$ is the error covariance matrix

$$\mathbf{S_y} = \quad \langle \mathbf{\Delta y \Delta y^T} \rangle \tag{5.13}$$

of the measurement y. The brackets $\langle\rangle$ denote the expected value operator. The diagonal elements S_{yii} are the variances ($\sigma_{y_i}^2$) and the off-diagonal elements S_{yij} are the covariances ($\sigma_{y_i y_j}$). The solution $\mathbf{s} = \mathbf{D}\mathbf{y}$ is called the least-squares solution since the quadratic expression

$$\Psi = (\mathbf{Ks} - \mathbf{y})^{\mathbf{T}} \mathbf{S_y^{-1}} (\mathbf{Ks} - \mathbf{y})^{\mathbf{T}}, \tag{5.14}$$

is minimized. The error covariance matrix of the measurement is not known. We assume the detector errors to be uncorrelated and constant for all detectors. The amplitude of the intensity errors σ_{y_i} of the measurement is assumed to be 2% of the largest intensity measured.

For the forward model defined by Eq. (5.8 - 5.10) the matrix ($\mathbf{K^T S_y^{-1} K}$) is close to being singular and the solutions $\mathbf{s}$ are very unstable. In order to obtain a stable and physically meaningful result we include *a priori* information about the solution. This can be done by applying the Phillips-Tikhonov regularization [*Phillips*,1962; *Tikhonov*, 1963], which is based on minimizing a quadratic expression of the form

$$\Psi = (\mathbf{Ks} - \mathbf{y})^{\mathbf{T}} \mathbf{S_y^{-1}} (\mathbf{Ks} - \mathbf{y}) + \gamma (\mathbf{Ls})^{\mathbf{T}} (\mathbf{Ls}). \tag{5.15}$$

This leads to the generalized inverse matrix

$$\mathbf{D} = (\mathbf{K^T S_y^{-1} K} + \gamma (\mathbf{L})^{\mathbf{T}} (\mathbf{L}))^{-\mathbf{1}} \mathbf{K^T S_y^{-1}}. \tag{5.16}$$

Both terms are minimized simultaneously, while the Lagrange-multiplier γ controls the relative weight of the terms. In many applications, the matrix $\mathbf{L}$ is chosen to be the $(n \times n)$ unity matrix

$$\mathbf{L_0} = \begin{pmatrix} 1 & 0 & \cdots & 0 \\ 0 & 1 & & \vdots \\ \vdots & & \ddots & 0 \\ 0 & \cdots & 0 & 1 \end{pmatrix}. \tag{5.17}$$

In this case, the second term of Eq. (5.15) is the norm of solution. This constrains the amplitude of the solution in a least-squares sense. In order to constrain the smoothness of the solution $\mathbf{s}$ we use the discrete difference matrix $\mathbf{L} = \mathbf{L_1}$ defined by

$$\mathbf{L_1} = \begin{pmatrix} 1 & -1 & 0 & \cdots & 0 \\ 0 & 1 & -1 & & \vdots \\ \vdots & & \ddots & \ddots & 0 \\ 0 & \cdots & 0 & 1 & -1 \end{pmatrix} \tag{5.18}$$

with the dimensions $(n-1) \times n$. With this choice of $\mathbf{L}$ the second term of Eq. (5.15) is the norm of the derivative of the solution. One can also use the matrix $\mathbf{L} = \mathbf{L_2}$ with

$$\mathbf{L_2} = \begin{pmatrix} 1 & -2 & 1 & 0 & \cdots & 0 \\ 0 & 1 & -2 & 1 & & \vdots \\ \vdots & & \ddots & \ddots & \ddots & 0 \\ 0 & \cdots & 0 & 1 & -2 & 1 \end{pmatrix} \tag{5.19}$$

with the dimensions $(n-2)\times n$. In this case the norm of the second derivative of the solution is minimized. The regularizations with the matrices $\mathbf{L_1}$ and $\mathbf{L_2}$ have both a smoothing effect on the solution. In the following we show the results using $\mathbf{L} = \mathbf{L_1}$. For an optimal choice of γ we consider the number of degrees of freedom N_f of the solution that are determined by the measurement. The number of degrees of freedom indicates how many independent pieces of information are present in the solution $\mathbf{s}$. The number N_f is identical to the length of the solution vector $\mathbf{s}$ if γ equals zero. For non-zero values of γ, the values of the size distribution at different size bins are not independent. N_f decreases with an increasing value of γ since the number of degrees of freedom is imposed by the smoothness constraint. The number of degrees of freedom is determined based on the averaging kernel $\mathbf{A}$ [*Rodgers*, 2000]. The averaging kernel is the product of the Jacobian matrix $\mathbf{K}$ of the forward model with the generalized inverse matrix $\mathbf{D}$

$$\mathbf{A} = \mathbf{DK}. \tag{5.20}$$

This matrix represents the sensitivity of the retrieved size distribution with respect to the true (unknown) size distribution [*Rodgers*, 1990]. The trace of the matrix $\mathbf{A}$ is a measure for the number of degrees of freedom of the solution N_f. We use one value for the Lagrange-parameter γ for all retrievals such that the solutions are stable and smooth. The solutions based on Mie and diffraction theory have 41 bins with about 10 degrees of freedom. The solutions based upon using T-matrix calculations have 27 bins with about 6 degrees of freedom.

The surface distributions retrieved using diffraction theory are shown in Figure 5.5. The surface distributions of the feldspar, the quartz, and the red clay sample are shown as solid black curves. In order to quantify the accuracy of the measurement we determine the sensitivity of the retrieved size distribution with respect to instrument noise. For a given error covariance matrix of the measurement $\mathbf{S_y}$ the error covariance matrix of the resulting size distribution $\mathbf{S_s}$ is

$$\mathbf{S_s} = \quad \langle \mathbf{\Delta s \Delta s^T} \rangle = \langle (\mathbf{D\Delta y})(\mathbf{D\Delta y})^\mathbf{T} \rangle \quad = \mathbf{DS_yD^T}. \tag{5.21}$$

The error bars in Figure 5.5 depict the standard deviation of the error due to detector noise. The retrieval scheme used in combination with the particle sizer instrument has been developed in the group of M. Konert at the Vrije Universiteit Amsterdam. This retrieval scheme is based on diffraction theory [*Santer and Herman*, 1983]. The results of

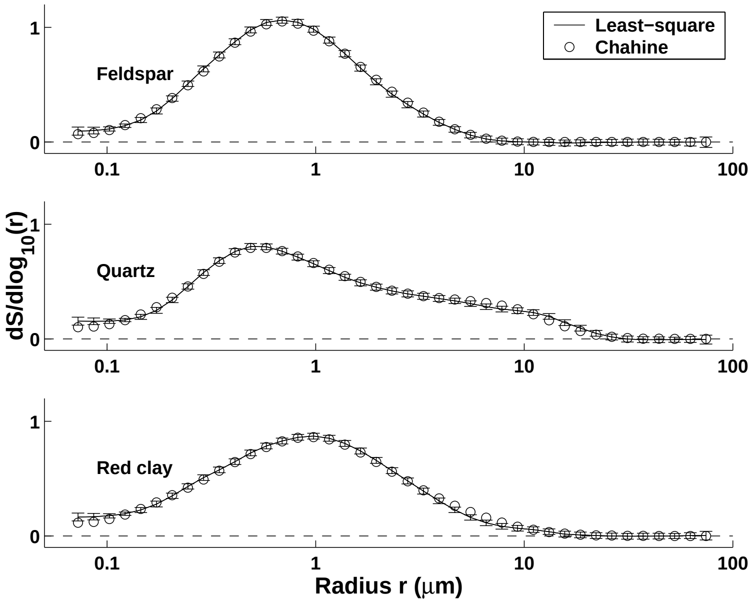

Figure 5.5: Surface distributions for the feldspar, the quartz and the red clay sample retrieved using diffraction theory. The results of the regularized linear inversion scheme are shown as solid lines. The error bars depict the uncertainty due to detector noise. The results are compared with the surface distributions derived using the Chahine iteration method (circles) which is nominally used in combination with the laser particle sizer.

the regularized linear inversion scheme and the Chahine iteration scheme (circles) agree very well for all three samples. The differences are on the orderof magnitude of the errors due to the assumed noise. The equivalence of the linear inversion schemes and the Chahine inversion scheme applied with an appropriate initial guess, has been shown by *Dubovik and King* [2000].

5.4 Results

The refraction of light is neglected implicitly when the diffraction method is applied to retrieve the size distribution of mineral particles. That means that light components that pass through the particle volume are not taken into account. Furthermore, the size-dependence of the scattering efficiency as well as shape effects are not taken into account. In order to quantify the impact of these approximations, the spherical and the spheroidal models are applied to the retieval of size distributions of three mineral aerosol samples (Section 5.4.1). The results are compared with the size distributions obtained using the diffraction model and the discrepancies are discussed. Furthermore, the diffraction model is used for the retrieval of parameterized size distributions of spherical particles (Section 5.4.2). With this, we investigate the systematic errors of the diffraction model for a range of size distributions. In a similar way, we determine the systematic errors of the spherical model applied to the retrieval of size distributions of non-spherical particles.

5.4.1 Feldspar, quartz and red clay

In Figure 5.6, we show the size distributions of the feldspar, the quartz, and the red clay sample that are retrieved from the intensity measurements using Mie calculations for strongly-absorbing spheres (black dots), Mie calculations for non-absorbing spheres (empty circles), and T-matrix calculations for non-absorbing spheroids (empty diamonds). The results deviate significantly from the results obtained using diffraction theory (+). The size distribution based on Mie scattering by non-absorbing spheres has a very pronounced minimum at the particle radii between 0.5 μm and 1 μm. This minimum is less pronounced for the size distribution based on Mie scattering by strongly-absorbing spheres. The size distributions based on the diffraction model do not exhibit this minimum at all. This discrepancy is observed for all three samples and can be explained by the difference in the scattering efficiency Q and the phase function $P(\Theta)$ of the various light scattering models (see Fig. 5.3). At the particles sizes where the diffraction model underestimates the scattering efficiency, it overestimates the size distribution. This is the case at particle sizes close to 1 μm. The diffraction model underestimates the light scattering in the sideward scattering directions in a characteristic way. As shown in Fig 5.4 weakly absorbing particles larger than 1 μm cause a light scattering signal with a maximum between the detectors 40 and 50. This light scattering signal is assigned to particles in the size range between 0.5 μm and 1 μm if the diffraction model is applied.

In order to show that this discrepancy is a systematic feature due to the different nature of the models used, we consider retrievals from synthetic measurements that are forward simulated based on Mie theory. In Fig. 5.7, we show the results of simulations for log-normal size distributions of spheres with a refractive index of $1.52 - 0.001i$. A log-normal size distribution is a parameterized mono-modal size distribution (for definition see Section 5.4). A log-normal size distribution with an effective radius $r_{\text{eff}} = 3$ μm and an effective variance $v_{\text{eff}} = 3$ is assumed. We note that the retrieval scheme based on diffraction(+) indeed overestimates the size distribution at radii between 0.5 μm and 1 μm. As a consistency check, we compare the initial size distribution as well with a retrieval based on Mie calculations for spheres with the same refractive index. The initial size distribution is reproduced for spheres with radii $r \geq 0.3$ μm, but not for smaller particles. At particle radii smaller than about 0.3 μm, the size distribution based on Mie

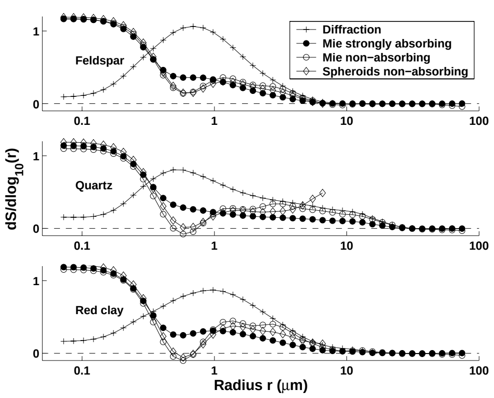

Figure 5.6: Surface distributions retrieved using diffraction theory (crosses), Mie theory for strongly absorbing spheres (black dots), Mie theory for non-absorbing spheres (empty circles), and *T*-matrix calculations for non-absorbing spheroids. We show results based on the intensity measurements from the feldspar, the quartz and the red clay samples.

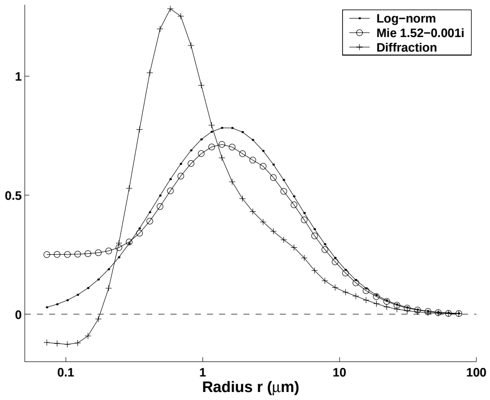

Figure 5.7: Surface distributions retrieved from a synthetic measurement simulated using Mie theory for a log-normal size distribution with an effective radius $r_{\text{eff}} = 3$ and an effective variance $v_{\text{eff}} = 3$. The retrieval scheme based on diffraction(+) overestimates the size distribution in the size range between 0.5 μm and 1 μm. The retrieval scheme based on Mie theory (empty circles) overestimates the size distribution for size parameter $x \leq 3$. A refractive index of 1.52-0.001i is assumed for the Mie calculations.

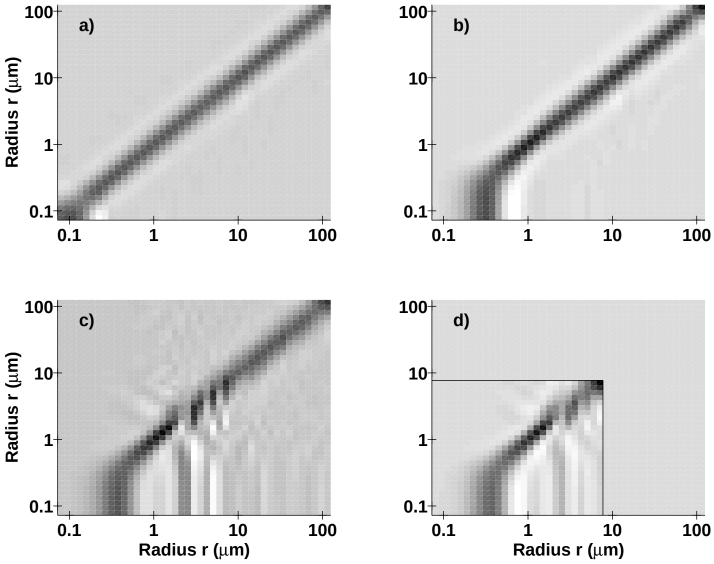

Figure 5.8: Averaging kernels for the diffraction model (a), the model based on Mie scattering by strongly-absorbing (b) and non-absorbing spheres (c), and the spheroidal model (d). Matrix elements with a high value are shown in dark gray.

theory is larger than the size distribution based on diffraction theory. The large values of the Mie results at these sizes are not meaningful. The failure of the retrieval at these small particle sizes is discussed in detail in the following.

The stability of the solution is tested. Firstly, we determine how the noise of the measurement maps onto the retrieved size distribution using Eq. (5.21). The errors of the size distributions determined using the Mie-theory (not shown) have a similar amplitude as the errors of the results from the diffraction theory (Fig. 5.5). The low noise amplitude of the solution is partly due to the smoothness constraint used to increase the stability of the solution. Secondly, we quantify to which extent an element of the retrieved size distribution is determined by the constraints or by the measurement. To this end, the averaging kernel matrix (Eq. 5.20) is considered. The averaging kernels based on the three different models discussed are depicted in Figure 5.8. The horizontal axis represents the particle sizes of the true size distribution. The vertical axis shows the particle radii of the retrieved size distribution.

The high values of the diagonal elements $\mathbf{A}_{ii}$ (dark gray) indicate that an inversion based on diffraction theory (a) produces a reliable size distribution on the full range of sizes considered, provided that the light scattering is accurately modeled by the diffraction model. The averaging kernel shown in Figure 5.8 (d) indicates that particles with radii smaller than $r = 0.3\ \mu$m can be distinguished using the diffraction model. The diffraction model predicts that the phase function approaches $P(\Theta) = const.$ with decreasing particle size. This is not physical and does not reflect the behavior of real particles discussed in the previous paragraph. The diffraction model is therefore not appropriate for small particle sizes. A comparison of the phase functions of the different models shows that this is true especially for the particles sizes with $r < 0.3\ \mu$m.

The averaging kernel matrices of the spherical (b, c) and spheroidal (d) models show that a meaningful size distribution can be retrieved for particle radii larger than about 0.3 μm. The size distributions retrieved based on Mie theory or the spheroidal model are not sensitive with respect to the true size distribution for particle radii smaller than about 0.3 μm. This can be explained as follows: With decreasing particle size, the phase function approaches the phase function $P_{\text{Ray}}(\Theta) \propto \cos^2(\Theta)$ of Rayleigh-scattering. That is why the phase functions of Mie scattering and of the spheroidal model do not change significantly with the particle size for particles with radii smaller than about 0.3 μm. The column vectors of the Jacobian matrices of the spherical and the spheroidal models are close to being linearly dependent. Hence, particles with different sizes in this size range cannot be distinguished. We conclude that the large values of the size distributions for $r < 0.3\ \mu$m determined using Mie theory or the spheroidal model are not meaningful. The shape of the size distribution is dominated by the smoothness constraint which causes the increasing trend at $r = 0.3\ \mu$m to continue.

These (not meaningful) high values of the size distributions at the smallest sizes can be reduced by an additional constraint that minimizes the norm of the solution [see *Dubovik and King*, 2000]. This can be achieved by minimizing the quadratic expression

$$\Psi = (\mathbf{Ks} - \mathbf{y})^{\mathbf{T}} \mathbf{S}_{\mathbf{y}}^{-1} (\mathbf{Ks} - \mathbf{y}) + \gamma_{\mathbf{0}} (\mathbf{L_0 s})^{\mathbf{T}} \mathbf{L_0 s} + \gamma_{\mathbf{1}} (\mathbf{L_1 s})^{\mathbf{T}} \mathbf{L_1 s}, \tag{5.22}$$

which leads to the generalized inverse matrix D

$$\mathbf{D} = \left[\mathbf{K}^{\mathbf{T}} \mathbf{S}_{\mathbf{y}}^{-1} \mathbf{K} + \gamma_{\mathbf{0}} \mathbf{L_0}^{\mathbf{T}} \mathbf{L_0} + \gamma_{\mathbf{1}} \mathbf{L_1}^{\mathbf{T}} \mathbf{L_1} \right]^{-\mathbf{1}} \mathbf{K}^{\mathbf{T}} \mathbf{S}_{\mathbf{y}}^{-\mathbf{1}}. \tag{5.23}$$

We chose Lagrange-multipliers γ_0 and γ_1 of the same order of magnitude as recommended by *Dubovik and King* [2000]. The amplitude of the Lagrange-multipliers is chosen such that the number of degrees of freedom is about 7. The resulting size distributions (Fig 5.10) may look more physical. However, the information added to the solution by using this constraint is not based on the measurement. We note that, according to the averaging kernel, the the values of the size distribution at radii between 0.3 μm and 0.6 μm are meaningful. In this size range the size distribution increases with decreasing radius. Therefore, we regard the presence of a small particle mode in the size distribution to be real. The shape of the resulting size distributions agrees well with the shape of size distributions retrieved from sun and sky radiometer measurements at desert sites [*Tanré*, 2001; *Dubovik et al.*, 2002]. These retrievals are based on a retrieval strategy similar to the one used here.

The refractive indices of feldspar, quartz and red clay are estimated to be 1.57−0.0005i,

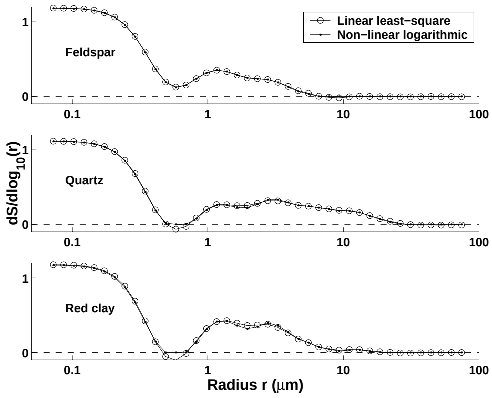

Figure 5.9: Surface distributions for the feldspar, the quartz and the red clay sample retrieved using Mie scattering by weakly-absorbing spheres (empty circles) assuming refractive indices of 1.57 − 0.0005i (feldspar), 1.54 − 0i (quartz), and 1.52 − 0.001i (red clay). A non-linear fit with a non-negativity constraint is tested for the inversion based on Mie scattering by non-absorbing spheres (crosses).

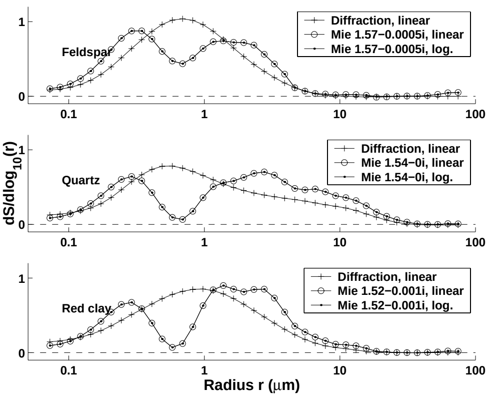

Figure 5.10: Surface distributions for the feldspar, the quartz and the red clay sample retrieved using constraints for both the amplitude and for the smoothness of the solution. We show results of a linear inversion scheme based on diffraction theory (+) and Mie theory (empty circles). We include as well the results of a logarithmic inversion scheme based on Mie theory (small dots). The refractive indices of 1.57 − 0.0005i (feldspar), 1.54 − 0i (quartz), and 1.52 − 0.001i (red clay) are used.

1.54 − 0i, and 1.52 − 0.001i respectively (see Chapter 4). The size distributions that are retrieved based on Mie theory using these estimates for the refractive indices are shown in Figure 5.9. The resulting size distributions do not differ significantly from the results obtained based on Mie scattering by non-absorbing spheres with a refractive index of 1.57 − 0i (circles in Fig. 5.6). The retrieved size distributions are thus insensitive with respect to variations of the refractive index in the range from 1.52 to 1.57 (real part) and from 0 to 0.001 (imaginary part).

When Mie theory for non-absorbing or weakly-absorbing spheres is used, we obtain negative values at a few particle sizes. This is the case, e.g. for the size distributions of

Table 5.1: Effective radius r_{eff} (μm) and effective variance v_{eff} of the size distributions based on the diffraction model and the spherical model. The right column refers to a size distribution that is truncated at the size parameter $x = 3$.

		Diffraction		Mie		Mie truncated	
		r_{eff}	v_{eff}	r_{eff}	v_{eff}	r_{eff}	v_{eff}
Feldspar	m = 1.57-0.0005i	1.0	0.9	0.5	2.5	1.4	0.6
Quartz	m = 1.54-0i	2.3	2.4	1.6	4.1	4.4	1.0
Red clay	m = 1.52-0.001i	1.5	2.3	0.9	3.4	2.4	0.8

quartz and red clay at the particle radius $r = 0.6$ μm shown in Fig 5.9. This contradicts the nature of number or surface distributions, which can only have positive values. That is why we present as well the results of a non-linear retrieval scheme, where the logarithm of the size distribution $\tilde{\mathbf{s}}$ with $\tilde{s_i} = \ln(s_i)$ are fitted. With this approach negative solutions are excluded *a-priori* [*Dubovik and King*, 2000]. The resulting size distribution (dots in Fig. 5.9 and 5.10) is very similar to the results from the linear inversion scheme (circles). This shows that the non-linear retrieval scheme based on fitting logarithms is a useful technique for laser particle-sizing.

The effective radii and the effective variances of the retrieved size distributions for the three mineral samples are listed in Table 5.1. We compare the result based on the diffraction model with results that are based on the spherical model using estimates for the refractive indices of the mineral samples. For the spherical model we include both the size distribution shown in Figure 5.9 as well as a size distribution that is truncated at the radius 0.3 μm. Below this size, the measurement is not sensitive to the particle abundance. With the latter two size distributions we include two extreme cases that are consistent with the measurement. The range of effective radii and effective variances defined by these two extreme cases includes the effective radius and the effective variance of the size distributions derived using the diffraction model.

5.4.2 Retrieval of parameterized size distributions

In many applications only the effective radius and the effective variance of a size distribution are taken into account. This is a commonly-used approach especially if the true size distribution is expected to be mono-modal. The effective radius and the effective variance of a size distribution can be retrieved directly using a parameterized size distribution. If the true size distribution is mono-modal, reducing the number of degrees of freedom makes the results more stable as compared to the retrieval of a size distribution with ten degrees of freedom as discussed in the previous section.

In this section, we investigate how the retrieved parameters depend on the choice of the light scattering model used for the retrieval. For this purpose we use synthetic measurements that are simulated based on a log-normal size distribution

$$\nu(r) = \frac{1}{\sqrt{2\pi}\,\ln(\sigma_g)}\,\frac{1}{r}\exp\left(\frac{-\left[\ln(r)-\ln(r_g)\right]^2}{\ln(\sigma_g)^2}\right) \tag{5.24}$$

with

$$r_g = \frac{r_{\mathrm{eff}}}{(1+v_{\mathrm{eff}})^{2.5}} \quad \text{and} \quad \ln(\sigma_{\mathrm{g}}) = \sqrt{\ln(1+\mathrm{v}_{\mathrm{eff}})}.$$

This describes a mono-modal size distribution with the effective radius r_{eff} and the effective variance v_{eff} as parameters [see e.g. *Hansen and Travis*, 1974].

We investigate the systematic errors that are introduced when diffraction theory is used for spherical particles. We consider a range of synthetic measurements that are simulated using log-normal size distributions of strongly-absorbing or non-absorbing spheres. The parameters r_{ret} and v_{ret} are retrieved from the synthetic measurements based on the diffraction model. The fit parameters are determined using an advanced non-linear fit routine that is based on a large-scale trust region method [*Coleman and Li*, 1996]. The two-dimensional parameter space of the retrieved parameters is mapped onto the two-dimensional input parameter space. This mapping provides estimates for the systematic errors that are introduced by using the diffraction model for mono-modal size distributions of spherical particles.

In Figure 5.11 we show the differences between the retrieved and the initial effective radii $\Delta r_{\mathrm{reff}} = r_{\mathrm{ret}} - r_{\mathrm{true}}$ (a and c) and the differences between retrieved and initial effective variances $\Delta v_{\mathrm{reff}} = v_{\mathrm{ret}} - v_{\mathrm{true}}$ (b and d). The differences are plotted in gray values as a function of the input parameters r_{true} and v_{true} of the forward calculation.

If strongly-absorbing spheres are present (a, b), the diffraction model provides realistic values for the effective radius and the variance for narrow size distributions with $v_{\mathrm{eff}} < 1$. For broader size distributions, systematic errors are encountered for both r_{eff} and v_{eff}: The variance is underestimated while the effective radius is underestimated for $r_{\mathrm{eff}} > 2.5$ μm and overestimated for $r_{\mathrm{eff}} < 2.5$ μm. The difference between the initial and the retrieved effective variance is nearly proportional to v_{true}.

If non-absorbing spheres are present (c, d), the diffraction model provides realistic values for the effective radius and the variance only for narrow size distributions with $v_{\mathrm{eff}} < 1$ with a low effective radius $r_{\mathrm{eff}} < 2$ μm. For broader size distributions with a larger effective radius, both parameters are underestimated. The difference between the initial and the retrieved effective radius is nearly proportional to r_{true}. The difference between the initial and the retrieved effective variance is nearly proportional to v_{true}.

When the size distributions of mineral samples are retrieved using Mie theory, the irregular shape of the mineral particles is neglected. We investigate the systematic errors due to the spherical approximations using synthetic measurements that are simulated based on the spheroidal model (see Section 5.3.1). We use a parameterized size distribution as outlined above. In the lower graphs of Figure 5.11, we show the differences between the retrieved and the initial effective radii $r_{\mathrm{ret}} - r_{\mathrm{true}}$ (e) and the differences between retrieved and initial effective variances $v_{\mathrm{ret}} - v_{\mathrm{true}}$ (f). The agreement of the spherical model and the

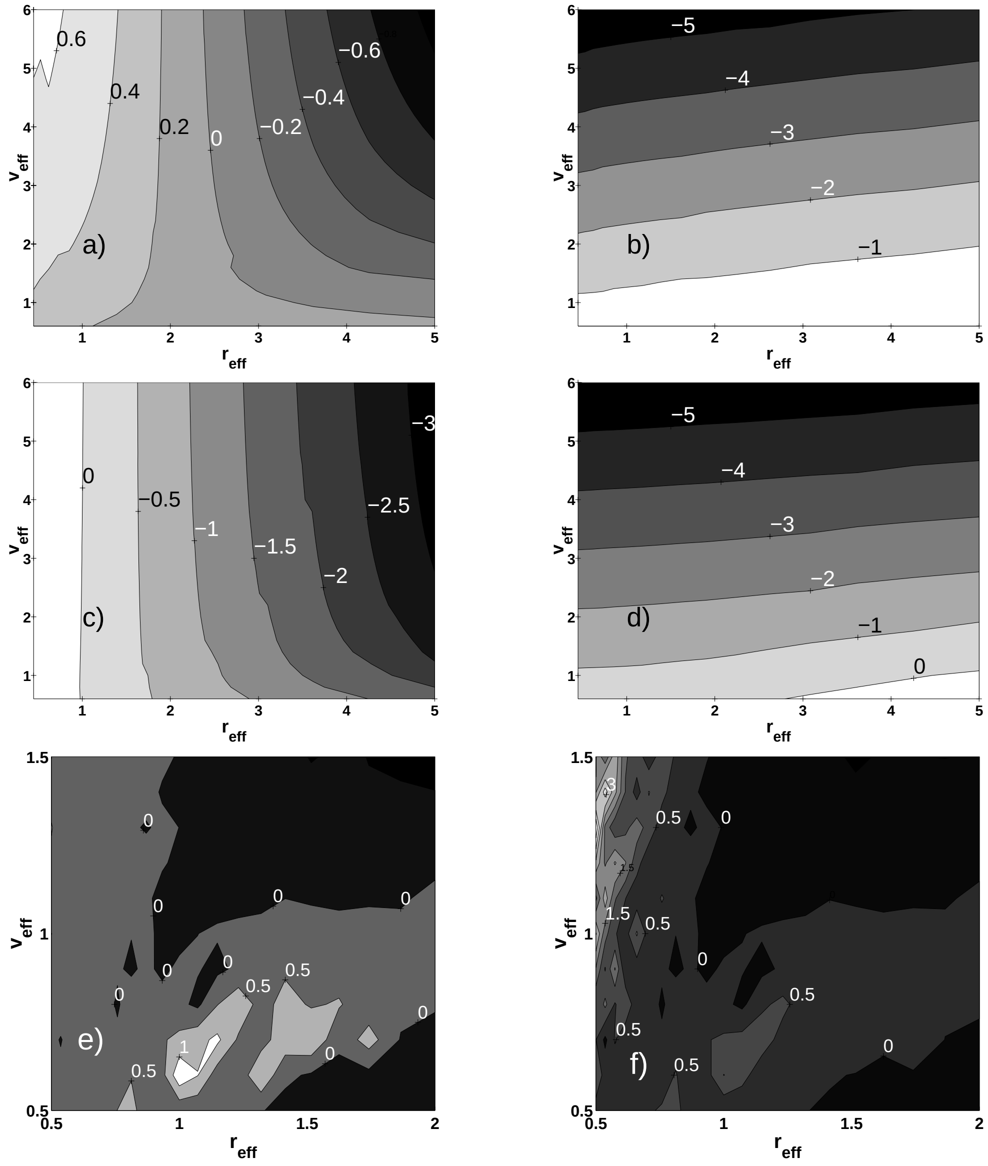

Figure 5.11: Difference between the retrieved and the true effective radius $\Delta r_{\text{reff}} = (r_{\text{ret}} - r_{\text{true}})$ (a, c, e) and the difference between the retrieved and the true effective variance $\Delta v_{\text{reff}} = (v_{\text{ret}} - v_{\text{true}})$ (b, d, f). The upper 4 graphs show the results of retrievals based on diffraction theory. The forward model is based on Mie scattering by strongly-absorbing (a, b) and by non-absorbing spheres (c, d). The lower two graphs (e, f) show the results of retrievals based on Mie theory. The forward model is based on light scattering by a mixture of oblate and prolate spheroids.

spheroidal model for non-absorbing particles is very good except for two regimes. These regimes include narrow size distributions with particle radii in the range from 1 μm to 1.5 μm and size distributions with r_{eff} close to 0.5 μm and $v_{\mathrm{eff}} > 1$. In the size range with radii from 1 μm to 1.5 μm Mie scattering has pronounced resonance features in the scattering efficiency (Fig. 5.3) as well as in the phase function that have an impact on the Jacobian matrix (Fig. 5.4, c). These features are less pronounced for scattering by spheroidal particles. This causes errors of the retrieved parameters for narrow size distributions. For broader size distributions, these discrepancies average out.

5.5 Conclusions

The laser particle-sizing technique presented in this study allows the measurement of the size distribution for particles with volume-equivalent radii $r \geq 0.3$ μm. This limit is largely determined by the wavelength of the laser light (632.8 nm). Smaller particles sizes can be measured using shorter wavelengths.

The surface distributions of mineral aerosol samples inculding feldspar, quartz, and red clay are retrieved using various light scattering models including diffraction theory, Mie theory for spherical particles with various refractive indices, and T-matrix calculations for non-absorbing spheroidal particles. The obtained size distributions depend on the light scattering model used for the interpretation of the light intensity measurements. The differences between the diffraction model and the spherical model are larger than the differences between the spherical model and the spheroidal within the applicable size range. The size distributions retrieved based on Mie theory are insensitive with respect to uncertainties of the refractive index in the range from 1.52 to 1.57 (real part) and from 0 to -0.001i (imaginary part). These uncertainties are typical for natural mineral samples.

The retrieval based on diffraction theory systematically overestimates the size distribution at radii between $r = 0.5$ μm and $r = 1$ μm as compared to retrievals based on Mie theory or the spheroidal model. This systematic error is largely caused by a prominent maximum of the scattering efficiency close to $r = 1$ μm, which is neglected when diffraction theory is used. This maximum is pronounced especially for weakly-absorbing and non-absorbing particles with both spherical as well as spheroidal shapes. Light scattering simulations for Gaussian random shapes (see Chapter 7) show that this maximum is pronounced as well for nonspherical particles that have no rotational symmetry. Experimental evidence for the presence of such a maximum in the extinction efficiency of irregular particles has been given for quartz and diamond dust samples as well as for other powdery substances [*Bohren and Huffmann*, 1983, Sec. 11.7.3 and references therein]. This suggests that the size distribution of natural irregular dust containing particles with sizes comparable to the wavelength should be retrieved using the spherical model rather than the diffraction model. A quantification of the systematic errors of the retrieved size distributions of truly irregular particles with internal inhomogeneities, as they are present in natural mineral dust, is not possible due to the lack of an efficient light scattering model that can handle such model particles.

The shape of the size distributions obtained using Mie theory and the spheroidal model agree well with the shape of size distributions that have been retrieved from sun and sky radiometer measurements at desert sites [*Tanré*, 2001; *Dubovik et al.*, 2002]. These retrievals are based on Mie theory or a spheroidal model.

The effective radius and the variance of a parameterized log-normal size distribution can be retrieved directly from the measurement. This is appropriate if the true size distribution is mono-modal. The diffraction model provides accurate values for the effective radius and the effective variance for narrow size distributions of strongly-absorbing spheres with an effective radius larger than 0.2 μm. For ensembles of non-absorbing spheres, the effective radius and the effective variance are retrieved correctly only for narrow size distributions with an effective radius of $r_{\mathrm{eff}} < 2$ μm. The analysis of systematic errors introduced by the spherical shape approximation when non-spherical particles are present is restricted to small particles with volume equivalent radii smaller than 10 μm. In the range of size distributions studied, the systematic errors are significant only for narrow size distributions with effective radii close to $r_{\mathrm{eff}} = 1$ μm.

Simulations using model shapes have been exploited to evaluate light scattering models in the context of laser particle sizing. The observed trends allow an extrapolation of the results to ensembles of truly irregular particles. An efficient light scattering model that can handle truly irregular particles including internal inhomogeneities is still lacking as reliable reference. Therefore, we would like to encourage nephelometer measurements of size resolved irregular particle samples.

Bibliography

Bohren, C.F., and D. R. Huffman, *Absorption and Scattering of Light by Small Particles*, John Wiley, New York, 1983.

Born, M., and E. Wolf, *Principles of Optics 7-th ed.*, Cambridge University Press, 1999.

Chahine, M. T., Inverse problems in radiative transfer: determination of atmospheric parameters, *J. Atm. Sci., 27*, 960–967, 1970.

Coleman, T. F., and Y. Li, An interior, trust region approach for non-linear minimization subject to bounds, *SIAM J. on Optimization, 27*, 960–967, 1970.

Dubovik, O., and M. D. King, A flexible inversion algorithm fro retrieval of aerosol optical properties from Sun and sky radiance measurements, *J. Geophys. Res., 105*, 20673-20696, 2000.

Dubovik, O., B. N. Holben, T. F. Eck, A. Smirnov, Y. J. Kaufman, M. D. King, D. Tanré, and I. Slutsker, Variability of absorption and optical properties of key aerosol types observed in worldwide locations, *J. of the Atmos. Sci., 59*, 590–608, 2002.

Hansen, J. E., and L. D. Travis, Light scattering in planetary atmospheres, *Space Sci. Rev., 16*, 527–610, 1974.

Huffman, D. R., The interaction of light with a small-particle system, *Adv. Phys., 26*, 129–130, 1977.

Klein, C., *Manual of Mineral Science, 22-nd ed.*, John Wiley, New York, 2002.

Mishchenko, M. I., and L. D. Travis, Capabilities and limitations of a current FORTRAN implementation of the T-matrix method for randomly oriented, rotationally symmetric scatterers, *J. Quant. Spectrosc. Radiat. Transfer, 60*, 309–324, 1998.

Mishchenko, M. I. , J. W. Hovenier, and L. D. Travis, T-matrix method and its applications, in *Light Scattering by Nonspherical Particles*, edt. M. I. Mishchenko, J. W. Hovenier, and L. D. Travis, Academic Press, San Diego, 147–172, 2000.

Kocifaj, M., and M. Držík, Retrieveing the size distribution of microparticles by scanning the diffraction halo with a mobile ring gap detector, *J. Aerosol Sci., 28*, 797–804, 1996.

Liu, L., M. I. Mishchenko, J. W. Hovenier, H. Volten, and O. Muñoz, Scattering matrix of quartz aerosols: comparison and synthesis of laboratory and Lorenz-Mie results, *J. Quant. Spectrosc. Radiat. Transfer, 79-80*, 911–920, 2003.

Phillips, D. L., A Technique for the numerical solution of certain integral equations of the first kind, *J. Assoc. Comput. Math., 9*, 84–97, 1962.

Rodgers, C. D., Characterization and error analysis of profiles retrieved from remote sounding measurements, *J. Geophys. Res., 95*, 5587–5595, 1990.

Rodgers, C. D., *Inverse Methods for Atmospheric Sounding: Theory and Practice*, World Scientific, London, 2000.

Santer, R., and M. Herman , Particle size distributions from forward scattered light using the Chahine inversion scheme, *Appl. Opt., 22*, 2294–2301, 1983.

Sokolik, I. N., and O. B. Toon, Incorporation of mineralogical composition into models of the radiative properties of mineral aerosol from UV to IR wavelengths, *J. Geophys. Res., 104*, 9423–9444, 1999.

Tikhonov, A. N., On the solution of incorrectly stated problems and a method of regularization, *Dokl. Acad. Nauk. SSSR, 151*, 501–504, 1963.

Tanré, D., Y. J. Kaufman, B. N. Holben, B. Chatenet, A. Karnieli, F. Lavenu, L. Blarel, O. Dubovik, L. A. Remer, and A. Smirnov, Climatology of dust aerosl size distribution and optical properties derived from remotely sensed data on the solar spectrum, *J. Geophys. Res., 106*, 18205–18217, 2001.

Veihelmann, B., H. Volten, and W. J. van der Zande, Light reflected by an atmosphere containing irregular mineral dust aerosol, *Geophys. Res. Lett., 31*, doi:10.1029/2003GL018229, 2004.

Volten, H., O. Muñoz, E. Rol, J. F. de Haan, W. Vassen , J. W. Hovenier, K. Muinonen, and T. Nousiainen, Scattering matrices of mineral particles at 441.6 nm and 632.8 nm, *J. Geophys. Res., 106*, 17375–17401, 2001.

Chapter 6

Spheroidal shape approximation

Abstract

Light scattering by irregular mineral aerosol particles is simulated using light scattering calculations for ensembles of spheroidal model shapes. Measured scattering matrices of a variety of mineral dust samples are used to investigate the consistency of these simulations with measured light scattering properties of truly irregular particles. The entire range of particle sizes relevant for the mineral samples is accounted for in the simulations by combining T-matrix calculations for small particles and geometric optics calculations for large particles. Scattering matrices are simulated using a pre-computed light scattering database. This light scattering database was generated for the retrieval of the properties of mineral aerosol from ground-based sun and sky photometer measurements from the AERONET network. Estimates of the refractive indices and the size distribution are used as input parameters for the simulations. The distribution of aspect ratios of the spheroidal model shapes is fitted using a nonlinear inversion algorithm. Scattering matrices are simulated as well using the refractive index and the size distribution as free fit parameters. The agreement of the simulated and the measured scattering matrices as well as the agreement of estimated and retrieved parameters is the basis for estimating the consistency of the predictions of the spheroidal shape approximation and light scattering by irregular particles. When the spheroidal shape approximation is used to retrieve the properties of irregular mineral aerosol from measured scattering matrices the imaginary part of the refractive index tends to be overestimated. The results presented are relevant for aerosol retrievals from scattered sunlight observations.

6.1 Introduction

Light scattering by nonspherical aerosols can be simulated efficiently using shape approximations. A variety of light scattering models using shape approximations has been discussed in Chapter 4. In the spheroidal shape approximation, irregular particles are represented by an ensemble of randomly oriented oblate and prolate spheroids. The shape of a spheroid is characterized by the aspect ratio $\epsilon = b/a$, defined as the ratio of the semi-major axes a and b shown in Figure 6.1. An ensemble of model particles contains spheroids with a distribution of sizes and aspect ratios. The spheroidal shape approximation is applied in simulations of absorption and scattering of solar light by mineral dust aerosol in planetary atmospheres. This shape approximation has been used to estimate the

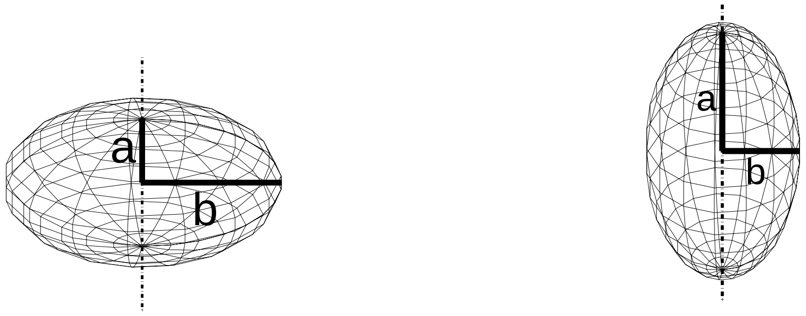

Figure 6.1: Oblate (left) and prolate (right) spheroids with the semi-major axes a and b.

impact of the nonsphericity of irregular mineral aerosol on remote sensing and on climate modeling [e.g. *Mishchenko et al.*, 1995; *Kahn et al.*, 1997; *Kahnert and Kylling*, 2004]. In these studies, the scattering and absorption properties of spheroidal particles is calculated using the T-matrix method (see Ch. 4).

Atmospheric aerosols are monitored using ground based sun and sky radiometer measurements from the AErosol RObotik NETwork (AERONET). These observations include measurements of the extinction of the direct solar radiation as well as measurements of scattered sunlight at wavelengths ranging from 0.34 to 1.6 μm. The scattered sunlight is measured in the almucantar with azimuth angles ranging from $2°$ to $180°$ relative to the sun [*Holben et al.*, 1998]. *Dubovik and King* [2000] have developed an inversion algorithm for the simultaneous retrieval of the refractive index, the size distribution, and the shape distribution. AERONET retrievals are sensitive to the particle shape. If mineral aerosols are present, the spheroidal shape approximation is used in order to take the nonsphericity of the scatterers into account. Light scattering simulations for spheroidal particles are made based on a combination of T-matrix calculations and Geometric-Optics-integral-equation calculations (Tm-GO) for spheriodal model shapes [*Dubovik et al.*, 2002] (see Ch. 4). With this combination of light scattering models the full size range relevant for atmospheric mineral aerosols is treated. Simulated light scattering properties of spheroidal model particles with a variety of sizes, refractive indices, and shapes are stored in a database. Using this database the light scattering properties of ensembles of spheroids with a distribution of shapes and sizes can be generated very quickly which is a precondition for the feasibility of the aerosol retrievals. In the following this database is referred to as the AERONET light scattering database. The spheroidal shape approximation in combination with T-matrix and geometric optics calculations is currently the only technique that can efficiently handle very broad size distributions of nonspherical aerosol particles. It is therefore important to validate the predictions of the spheroidal shape approximation with independent light scattering data.

In this chapter we investigate to which extent the scattering properties predicted by the spheroidal shape approximation using Tm-GO simulations are consistent with measured scattering properties of truly irregular mineral dust samples. The elements of the scattering matrix (see Ch. 4 for definition) have been measured by *Volten et al.* [2001] as a function of the scattering angle Θ in a nephelometer experiment. The scattering matrix is measured in the range of scattering angles from 5° to 173° at the wavelengths $\lambda = 441.6$ nm and $\lambda = 632.8$ nm. The consistency of a measured scattering matrix with T-matrix simulations using the spheroidal shape approximation has been tested by *Nousiainen and Vermeulen* [2003], *Veihelmann et al.* [2004], and *Nousiainen et al.* [2004] using the nephelometer measurement of a feldspar sample. In this study, we address this issue for various samples including the feldspar sample, a quartz sample, and two natural clay samples.

The measured scattering matrices of these four mineral dust samples are compared with Tm-GO simulations for ensembles of spheroidal model shapes. These simulations are made based on the AERONET light scattering database that is introduced in Section 6.2. For this study, the database has been extended to larger particle sizes in order to account for the full size range that is relevant for the mineral dust samples. The simulations depend on the complex refractive index, the size distribution, and the aspect ratio distribution which are only partly known *a priori*:

The measurements of the feldspar and the quartz samples are chosen for the validation since their mineral composition is known and the refractive index can therefore be estimated quite accurately (feldspar) or is known (quartz). The refractive index of the natural clay sample is uncertain due to uncertainties in the mineral composition. The mineral compositions of the samples chosen are typical for atmospheric desert dust aerosol. The size distributions of the samples have been measured using a laser diffraction particle sizer. The accuracy and the systematic errors of this technique have been discussed thoroughly in Chapter 5. The quartz and the clay samples comprise larger particle sizes than the feldspar sample. The two clay samples are chosen since their size distributions are similar. Using the AERONET light scattering database all four samples can be treated without cutting off a significant part of the size distribution. It is *a priori* not known which aspect ratio distribution is optimal for the simulations. Some of the input parameters that are required for the simulations are unknown or are not known accurately. Therefore, we chose the following strategy for the validation of the spheroidal shape approximation.

We consider simulations where *a priori* estimates for the refractive index and for the size distribution are used as input parameters and the shape distribution is optimized (case A). An optimal shape distribution is determined using an inversion scheme that minimizes the differences between simulation and measured scattering matrix (Section 6.3). The observed differences may either be due to a general discrepancy between light scattering by spheroidal and by irregular particles, or to erroneous *a priori* estimates for the size distribution and the refractive index. Therefore, we perform light scattering simulations as well using the refractive index and the values of the size distribution as free fit parameters (case B). With this, an optimal agreement of simulations and measurements is achieved. Furthermore, we consider simulations where the size distribution is fixed and all other parameters are optimized (case C).

Differences in the simulated scattering matrices as well as differences between retrieved parameters and *a priori* estimates are used to estimate the consistency of the spheroidal shape approximations with measured light scattering properties of truly irregular particles (Section 6.4). For all optimizations an advanced inversion algorithm is applied that allows the simultaneous retrieval of the aspect ratio distribution, the size distribution, and the refractive index. This algorithm is derived from the inversion algorithm used for monitoring mineral dust aerosols using measurements of the global network of ground-based sun and sky radiometers AERONET [*Dubovik and King*, 2000]. This validation is relevant for aerosol retrievals from scattered sunlight observations using the spheroidal shape approximation. The results of this study may be directly applicable to cases for which direct extinction observations are not available. This is the case for aerosol retrievals from satellite observations of reflected sunlight.

6.2 Forward simulation of the scattering matrix

The scattering matrix $F_{ij}(\Theta)$ of an ensemble of model particles is calculated as the weighted average of scattering matrices $\tilde{F}_{ij}(\Theta, r, \epsilon)$ of spheroidal particles. The simulated scattering matrix depends on the volume-equivalent sphere radius r, the aspect ratio ϵ and the scattering angle Θ (for definitions, see Ch. 4)

$$F_{ij}(\Theta) = \int_{\ln r_{\min}}^{\ln r_{\max}} \int_{\epsilon_{\min}}^{\epsilon_{\min}} \frac{\tilde{F}_{ij}(\Theta, r, \epsilon)}{V(r)} \frac{dV(r)}{d\ln(r)}\, w(\epsilon)\;\; d\epsilon\, d\ln(r). \tag{6.1}$$

The contributions $\tilde{F}$ are weighted with the normalized shape distribution $w(\epsilon)$ and the size distribution given in terms of the volume distribution $dV/d\ln(r)$. In order to speed up the light scattering simulations, *Dubovik et al.* [2002] have precomputed scattering matrices of spheroidal particles for a large range of sizes, aspect ratios and refractive indices. Scattering matrices are simulated by averaging the precomputed kernels $\mathbf{K}_{kl}$ that are weighted with the discrete size distribution v_k and the discrete shape distribution w_l

$$F_{ij}(\Theta) \approx \sum_k \sum_l \mathbf{K}_{kl} v_k w_l. \tag{6.2}$$

The kernels $\mathbf{K}_{kl}$ are the size integrated volume-specific elements of the scattering matrix

$$\mathbf{K}_{kl} = \int_{\ln(r_k)-d/2}^{\ln(r_k)+d/2} \frac{\tilde{F}_{ij}(\Theta, r_k, \epsilon_l)}{V(r_k)}\, d\ln(r) \tag{6.3}$$

and are stored in a database. The size distribution is given in terms of the volume distribution v_k

$$v_k = \int_{\ln(r_k)-d/2}^{\ln(r_k)+d/2} \frac{dV(r)}{d\ln(r)}\;\; d\ln(r) = \int_{\ln(r_k)-d/2}^{\ln(r_k)+d/2} \frac{4}{3}\pi r^3 \frac{dN(r)}{d\ln(r)}\;\; d\ln(r) \tag{6.4}$$

The radii r_k are chosen to be equidistant on a logarithmic grid with $\ln(r_{k+1}) - \ln(r_k) = d$. Note that the size distributions $dN/d\log_{10}(r)$ used in the previous chapters differs from the size distribution $dN/d\ln(r)$ by a factor $\ln(10)$.

This kernel database has been generated using a combination of T-matrix calculations for spheroidal particles with volume-equivalent radii smaller than $x \sim 30 - 40$ and geometric-optics-integral-equation calculations for the larger particles. This kernel database, which is used for AERONET retrievals, will be referred to in the following as the AERONET light scattering database. The original kernel database comprises 22 radii r_k ranging from 0.05 μm to 15 μm (at a wavelength of λ=441.6 nm). In order to account for the full size range that is relevant for the mineral samples, the database has been extended by 10 size classes including radii up to 40 μm (at a wavelength of λ=441.6 nm). The database comprises calculations for axis ratios ϵ_l ranging from 0.42 to 2.49, and for refractive indices ranging from 1.33 to 1.6 for the real part and from 0.0005 to 0.5 for the imaginary part. This range of values of the imaginary part covers the refractive indices of very strongly absorbing particles and almost non-absorbing particles. *Dubovik et al.* [2002] have invested more than one year of calculation time for the generation of this database.

For the simulations of the scattering matrix of an ensemble of model particles the kernels are first interpolated to the refractive index and the sizes and aspect ratios of the size and shape grid and are then averaged using Eq. 6.2. Even for an ensemble of model particles with a broad size and shape distribution, the scattering matrix can be generated from the kernel database within a few seconds once the database is read (which takes about 1 minute). With this strategy, efficient inversion calculations are feasible that would not be possible using direct light scattering simulations.

6.3 Inversion

Simulated scattering matrices depend on the size distribution, the shape distribution, and the complex refractive index. Optimal values for all input parameters can be retrieved from the non-zero elements of the measured scattering matrices using an advanced inversion algorithm developed by *Dubovik and King* [2000]. The differences between the measured and the simulated values of the relative matrix elements F_{11}, $-F_{12}/F_{11}$, F_{22}/F_{11}, F_{33}/F_{11}, F_{34}/F_{11}, F_{44}/F_{11} are minimized. The inversion algorithm is based on forward simulations with the spheroidal shape approximation using the AERONET light scattering database introduced in the previous section.

All input parameters or any subset of input parameters can be retrieved simultaneously from the measurements by minimizing the differences between the simulated and the measured scattering matrix in a least-squares sense. *A priori* values for any of the input parameters can be taken into account. The weight of the *a priori* values is controlled by so-called Lagrange-multipliers. If a parameter is used as a free fit parameter the related Lagrange-multiplier is set to zero. Parameters can be fixed to an *a priori* estimate by choosing a large value for the Lagrange-multiplier. In the following, various combinations of *a priori* estimates are used.

Of all elements of the scattering matrix, F_{11} and $-F_{12}/F_{11}$ are the most important matrix elements for AERONET retrievals and for other aerosol retrievals using passive remote sensing observations in the visible. This is the case since solar light is unpolarized and since the largest component of light observed at visible wavelengths (under cloud-free conditions) is singly-scattered. That is why the elements F_{11} and $-F_{12}/F_{11}$ are weighted more strongly than the other elements of the scattering matrix. In the inversion scheme the weight of a measurement is proportional to the inverse of the variance of the measurement error. A relative error of 5% is assumed for the phase function. An absolute error of 0.01 is assumed for the elements $-F_{12}/F_{11}$ and an absolute error of 0.1 is assumed for the other (relative) elements F_{ij}/F_{11}.

Fit parameters are optimized using a non-linear inversion scheme. The logarithms of the parameters are fitted instead of the parameters themselves. With this approach, negative values of naturally nonnegative parameters are excluded. This inversion scheme is discussed in detail in *Dubovik and King* [2000]. The inversion algorithm applied in this study is taken from the inversion algorithm used for retrieving aerosol parameters from AERONET data [*Dubovik and King*, 2000].

6.4 Results

The simulated scattering matrices of four mineral dust samples are compared with measurements. Firstly, the refractive index and the size distribution (which can be treated as well as free fit parameters) are fixed to *a priori* estimates (case A). Estimates for the complex refractive indices $m = n - ik$ are taken from various sources [*Huffman*, 1977; *Sokolik and Toon*, 1999; *Klein*, 2002] and are listed in Table 6.1. The imaginary part of the refractive index of quartz is known to be smaller than 0.0005. The value $k = 0.0005$ is chosen for all simulations for the quartz measurement since it is the smallest value that is included in the light scattering database. This overestimation of the imaginary part has a minor impact on the light scattering behavior. Many weakly absorbing minerals have a real part of the refractive index n that decreases with increasing wavelength. The typical differences between the values of n at $\lambda = 632.8$ nm and $\lambda = 441.6$ nm are on the order of magnitude of the uncertainty of the estimated values for n and are therefore not taken

	441.6 nm		632.8 nm		size	distribution
	n	k	n	k	r_{eff}	v_{eff}
Feldspar	1.57	0.0005	1.57	0.0005	1.0	1.0
Quartz	1.54	0.0005	1.54	0.0005	2.3	2.5
Red Clay	1.52	0.0010	1.52	0.0010	1.5	1.7
Green Clay	1.52	0.0010	1.52	0.0010	1.5	1.7

Table 6.1: *A priori* estimates for the complex refractive index $m = n - ik$, the effective radius r_{eff}, and the effective variance v_{eff} of the size distribution.

into account in the input values listed in Table 6.1. The right column shows estimates for the effective radius r_{eff} and the effective variance v_{eff} of the size distributions that are derived from laser particle sizing measurements (Chapter 5). In case A, the only free parameter used in the optimization is the aspect ratio distribution. An optimal aspect ratio distribution is determined using the inversion algorithm described in Section 6.3.

Secondly, all input parameters required for generating the scattering matrix from the kernel database are used as free fit parameters (case B). The inversion algorithm has thus the maximum number of degrees of freedom for finding the optimal agreement of measurement and simulation. If there is a general discrepancy between the predictions of the spheroidal shape approximation and the light scattering properties of truly irregular particles, we expect that the agreement of the simulations with the measurements improves at the cost of a deviation of the size distribution and the refractive indices from the true values. The retrieved parameters are therefore compared to *a priori* estimates.

Thirdly, the scattering matrix is simulated by using both the shape distribution and the complex refractive index as fit parameter while *a priori* data for the size distribution is used (case C). This approach accounts for the fact that the size distribution of a mineral dust sample should be the same for both wavelengths.

The results for the scattering matrices are discussed in Section 6.4.1. The results for the refractive index, the aspect ratio distribution and the size distribution are discussed in the Sections 6.4.2, 6.4.3, and 6.4.4.

6.4.1 Scattering matrix

In Figure 6.2 the simulated scattering matrices are shown for the case that *a priori* estimates are used for the refractive index and the size distribution (case A). The simulations (solid lines) are compared with measurements (dots) at the wavelengths 441.6 nm (black) and 632.8 nm (gray). This comparison is made for the feldspar sample (upper left), the quartz sample (upper right), the red clay sample (lower left), and the green clay sample (lower right). A χ^2-test using the standard deviations of the measurement errors shows that the differences between simulations and measurements are larger than the statistical measurement error.

The measured phase functions $F_{11}(\Theta)$ are very smooth and run rather flat in the range of scattering angles between $\Theta = 100^\circ$ and $\Theta = 170^\circ$. In order to remove the large dynamic range in the phase functions, we also plot the ratio of the simulated and the measured values (Fig. 6.3). This ratio shows characteristic differences in the shape of the phase functions. Both phase functions are normalized to unity at $\Theta = 30^\circ$. The simulated and the measured phase function differ by up to 60%. Since both over- and underestimations are found, the overall agreement of measurement and simulation cannot be improved significantly by applying a different scaling. The simulations tend to overestimate the phase function in the range of scattering angles from 60° to 90° and tend to underestimate it in the range from 120° to 150°.

The wavelength-dependence of the phase functions is depicted in Figure 6.4 as the ratio of the phase functions $F_{11}(441.6\text{ nm})/\mathrm{F}_{11}(632.8\text{ nm})$. The phase functions for a

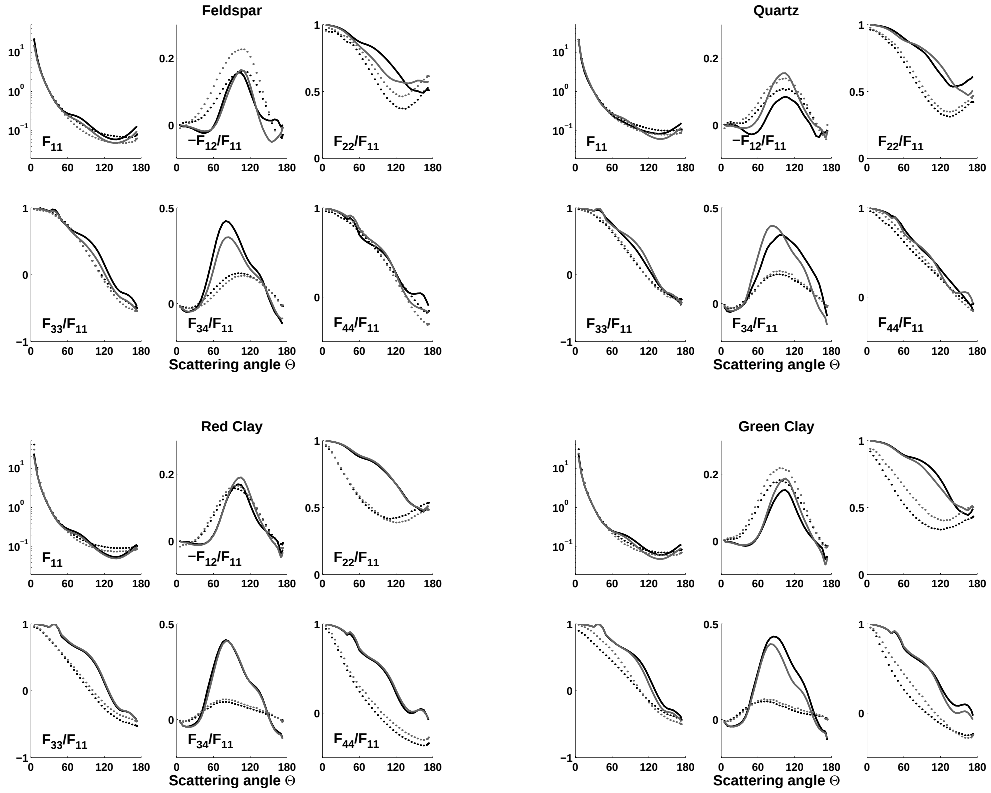

Figure 6.2: Case A: Measured scattering matrices (dots) and simulations (solid lines) for the wavelengths 441.6 nm (black) and 632.8 nm (gray). *A priori* data for the size distribution and the complex refractive index are used as input data. The shape distribution is fitted in order to optimize the agreement between measurement and simulation.

wavelength of 441.6 nm are usually steeper and have larger values close to the scattering angle $\Theta = 5°$ than the phase functions for a wavelength of 632.8 nm. The simulations reproduce this behavior consistently with the measurements for the feldspar sample. For the other samples, this behavior appears to be more pronounced in the simulations than in the measurements. Measurement and simulations of the quartz sample show the largest discrepancies regarding the wavelength-dependence of the phase function.

The simulations tend to underestimate the element $-F_{12}/F_{11}$ in the sideward scattering direction as compared to the measurements. This is especially pronounced for the scattering angles between 30° and 70°. The measurements of all mineral samples show negative values in $-F_{12}/F_{11}$ in a range of scattering angles between 160° and 180°. This

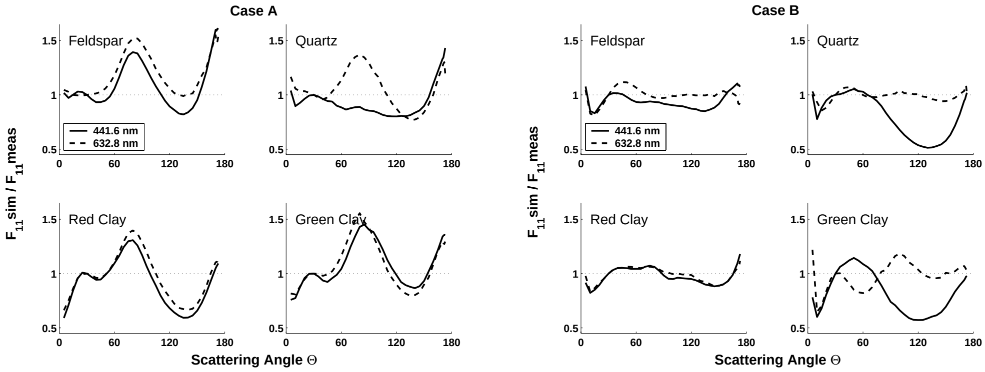

Figure 6.3: Ratio of the simulated and the measured phase functions for the wavelengths λ = 441.6 nm (solid) and λ = 632.8 nm (dashed). The simulations using *a priori* estimates for the refractive index and the size distribution (case A, left) are compared to simulations where all parameters are retrieved simultaneously (case B, right).

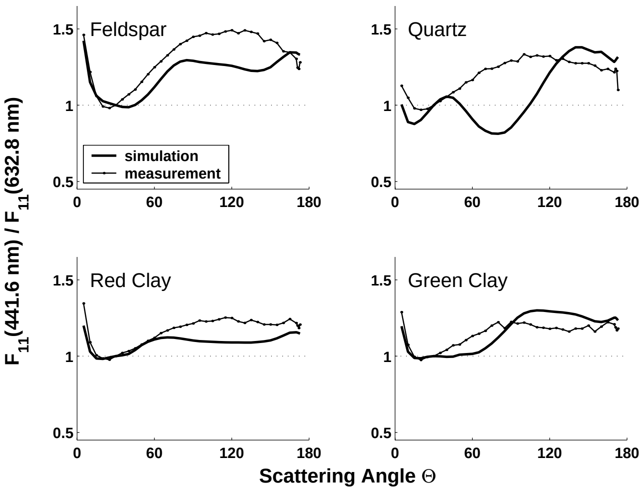

Figure 6.4: Ratio of the phase functions $F_{11}(\Theta)$ at $\lambda = 441.6$ nm and $F_{11}(\Theta)$ at $\lambda = 632.8$ nm. The ratio of phase functions is shown for measurements and simulations for various mineral dust samples. *A priori* estimates are used for the refractive index and the size distribution (case A).

negative branch is shown as well by the simulations.

The other elements of the scattering matrix will be discussed only very briefly since their weight in the inversion is small compared to the elements F_{11} and $-F_{12}/F_{11}$. The deviation of these other elements from the measured values has therefore a lower significance. The element F_{22}/F_{11} is overestimated by the simulations especially in the range of scattering angles between $\Theta = 100°$ and $\Theta = 170°$. The agreement of simulations and measurement is best for the feldspar sample and worst for the clay samples. Simulations and measurements of the element F_{33}/F_{11} and F_{44}/F_{11} are very similar for the feldspar sample and the quartz sample while significant discrepancies are found for the clay samples. The simulations tend to overestimate these elements for all samples especially in the range of scattering angles between 60° and 120°. Simulations strongly overestimate the element F_{34}/F_{11} between $\Theta = 60°$ and $\Theta = 150°$. The retrieved aspect ratio distribution is discussed in section 6.4.3.

Case B: The matching of measurements and simulations can be improved by using the size distribution as well as the refractive index as free fit parameters (Figure 6.5). A χ^2-test shows that the remaining differences between simulations and measurements still exceed the level that can be explained by the measurement errors. The inversion algorithm used is strong at finding the global minimum in the multi-dimensional parameter space. Therefore, we assume that the remaining discrepancies cannot be reduced significantly by modifying the input parameters of the simulation.

A very good agreement of measurements and simulations is achieved for the matrix elements F_{11} and $-F_{12}/F_{11}$ (Fig. 6.5). An exception are the scattering matrices of the quartz sample (upper right, black) and the green clay sample (lower right, black) at a wavelength of 441.6 nm. The ratio of the simulated and the measured phase functions is depicted in the right graph of Figure 6.3 in order to illustrate this behavior. We note that in these two simulations the imaginary part of the retrieved refractive indices (see Section 6.4.2) is not overestimated as it the case for the other simulations. Apparently, an artificially increased value of the imaginary part of the refractive index k helps to produce the smooth run of the phase function between $\Theta = 60°$ and $\Theta = 170°$ that is typical for irregular particles. We assume that the increased absorption removes structures from the phase function by damping resonances that are related to the symmetry of the model shapes.

A systematic overestimation of the element F_{22}/F_{11} is observed at scattering angles $\Theta > 60°$; the best agreement between simulation and measurement is found for the feldspar sample. Large discrepancies in the element F_{22}/F_{11} are found for simulations where the aspect ratio distribution has significant contributions due to near-spherical shapes (ϵ close to 1) as it is found for the green clay sample at $\lambda = 632.8$ nm. For the elements F_{33}/F_{11} and F_{44}/F_{11} the agreement of simulation and measurement is similar to what is observed for the case when *a priori* estimates for the refractive index and the size distribution are used.

Case C: If the complex refractive index is fitted and *a priori* estimates for the size distribution are used, the simulated scattering matrices are mostly between the simulations with the setting of case A and simulations with settings of case B.

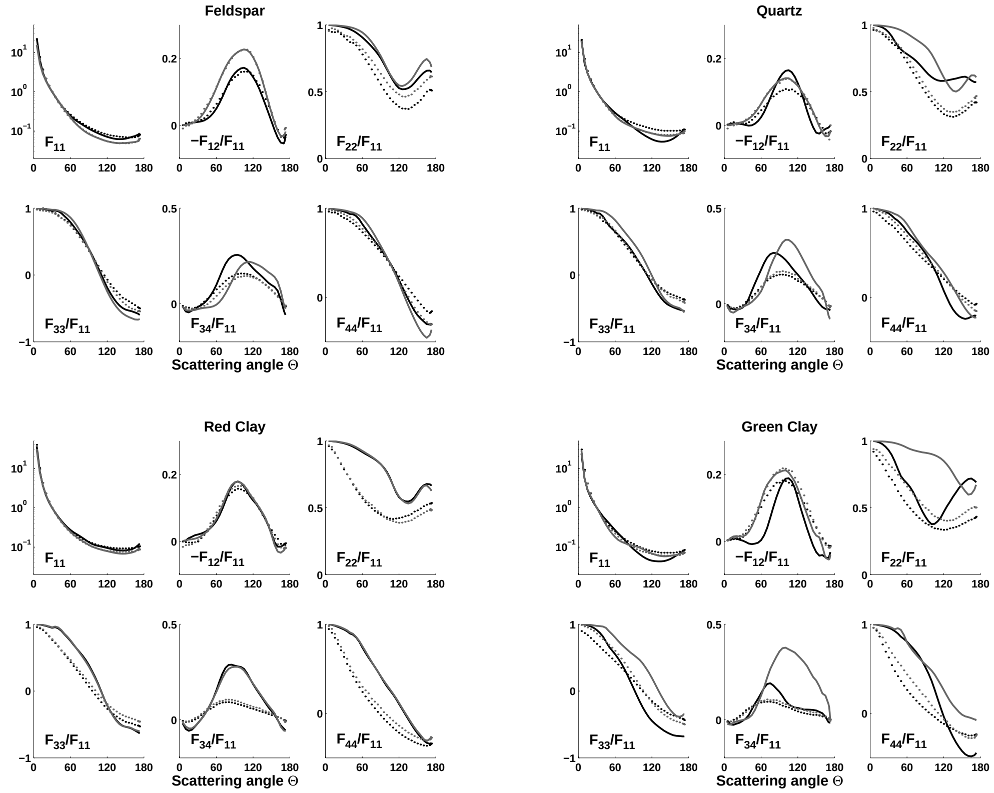

Figure 6.5: Case B: Measured scattering matrices (dots) and simulations (solid lines) for the wavelengths 441.6 nm (black) and 632.8 nm (gray). The size distribution, the shape distribution and the complex refractive index are fitted in order to achieve an optimal agreement between measurement and simulation.

6.4.2 Refractive index

In this section, we discuss the retrieved values of the complex refractive index $m = n - ik$ for the cases B and C. In case A, the refractive index is not retrieved. The retrieved values for the real part of the refractive index n are similar to the estimated values and are in the range of values that is typical for weakly absorbing mineral aerosol. This is the case for the measurements of all four samples at both wavelengths. The retrieved values do not correlate with the *a priori* estimates (Table 6.2). This is true for retrievals where the values of the size distribution are treated as a free fit parameters (case B) as well as for retrievals where the size distribution is fixed to the *a priori* estimates (case C). In case B, the values retrieved from the scattering matrices measured at 441.6 nm are larger than the values retrieved from the measurement at 632.8 nm. This trend, which was not taken into account in the *a priori* estimates, reflects the properties of many weakly absorbing minerals. This trend is not found in the retrieved values for n in case C.

	441.6 nm		632.8 nm	
	n	k	n	k
Case B:				
Feldspar	1.51 (1.57)	0.0035 (0.0005)	1.47 (1.57)	0.0045 (0.0005)
Quartz	1.60 (1.54)	0.0005 (0.0005)	1.52 (1.54)	0.0024 (0.0005)
Red Clay	1.58 (1.52)	0.0078 (0.0010)	1.54 (1.52)	0.0068 (0.0010)
Green Clay	1.55 (1.52)	0.0005 (0.0010)	1.42 (1.52)	0.0036 (0.0010)
Case C:				
Feldspar	1.53 (1.57)	0.0051 (0.0005)	1.60 (1.57)	0.0359 (0.0005)
Quartz	1.53 (1.54)	0.0005 (0.0005)	1.55 (1.54)	0.0032 (0.0005)
Red Clay	1.56 (1.52)	0.0021 (0.0010)	1.55 (1.52)	0.0023 (0.0010)
Green Clay	1.56 (1.52)	0.0089 (0.0010)	1.60 (1.52)	0.0236 (0.0010)

Table 6.2: Retrieved refractive indices compared to *a priori* estimates (in parentheses).

The imaginary part of the retrieved refractive indices k turns out to be significantly overestimated in most retrievals. In these cases the retrieved values are clearly outside the range of values that is realistic for the mineral samples. For simulations where all parameters are used as fit parameters (case B), we note that the differences between the simulated and the measured elements F_{11} and F_{12}/F_{11} are particularly large when the imaginary part of the retrieved refractive indices is not overestimated. This is true for the simulations for quartz and green clay at a wavelength of 441.6 nm. Here, the discrepancies of the phase functions are especially large in the range of scattering angles between $\Theta = 90°$ and $\Theta = 150°$ (see right graph of Figure 6.3). The agreement of the simulated and the measured scattering matrices appears to improve at the cost of a deviation of the imaginary part of the refractive indices from the true values. A large value of k damps resonances that are related to the symmetry of the spheroidal model particles and therefore tends to smoothen the simulated phase functions. An overestimation of k therefore helps to reduce differences between simulated phase functions and phase functions of truly irregular particles that typically run very smoothly in the range of scattering angles between $\Theta = 60°$ and $\Theta = 170°$.

These results indicate that the retrieval of the refractive index from measured scattering matrices using the AERONET light scattering database provides information about the real part n but not about the imaginary part k of the refractive index. The imaginary part of the refractive index is overestimated for most measurements at the wavelengths of 632.8 nm and of 441.6 nm.

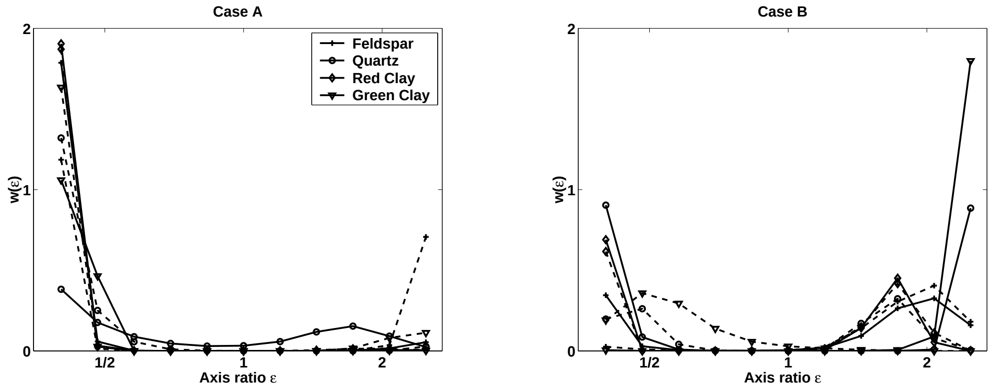

Figure 6.6: Aspect ratio distribution retrieved from the scattering matrices of the feldspar sample (crosses), the quartz sample (circles), the red clay sample (diamonds), and the green clay sample (triangles) measured at the wavelengths 421.6 nm (solid) and 632.8 nm (dashed). The left graph shows the results of a retrieval using *a priori* estimates for the refractive index and the size distribution (case A). The right graph shows results of a retrieval where all parameters are retrieved simultaneously (case B).

6.4.3 Aspect ratio distribution

For all mineral samples considered, the retrieved aspect ratio distribution $w(\epsilon)$ has very low values close to $\epsilon = 1$ (Fig. 6.6). When *a priori* estimates for the refractive index and the size distribution are used, the largest weights are assigned to the most elongated prolate and the most flattened oblate shapes with $\epsilon = 0.42$ and $\epsilon = 2.4$. When all parameters are fitted, the aspect ratio distribution gives more weight to the more moderately nonspherical shapes with $\epsilon = 0.5$ and $\epsilon = 1.8$ in various cases.

Nousiainen et al. [2004] have used a parameterized distribution of spheroidal shapes for simulating the scattering matrix of the feldspar sample. The approach of used by *Nousiainen et al.* [2004] is very similar to the approach used in this study. The optimal parameterized distribution also weights strongly the extreme aspect ratios while the weight of the (nearly) spherical shapes is (close to) zero. This kind of aspect ratio distribution is not observed in microscope images of irregular mineral samples. In a shape analysis of volcanic ash samples we have determined the probability distribution for the aspect ratio of ellipses that are fitted to the projections of a large number of particles *Muñoz et al.* [2004]. Aspect ratio distributions derived from this kind of shape analysis exhibit a maximum close to $\epsilon = 1$. Ellipses that are fitted to particle projections only capture the low-order nonsphericity. The finer structure of the particle shapes can be accounted for by including spheroids with more extreme aspect ratios. It may be concluded, that in order to capture the light scattering behavior of irregular particles, an optimized shape distribution is more useful than shape distributions that are derived from fitting ellipses directly to realistic particle shapes.

6.4.4 Size distribution

The size distribution cannot be retrieved reliably from the measured scattering matrices. The scattering matrix is measured at scattering angles $\Theta \geq 5^\circ$. Therefore, the phase function is not measured at the scattering angles close to the forward scattering direction where the sensitivity with respect to the size distribution is highest. A variation of the size distribution by 20% in both the effective radius and the effective variance has a minor effect on the simulated scattering matrix. Using the improved size distribution that is retrieved from the laser particle sizer measurement using Mie theory (Chapter 5) does not improve the agreement of simulations and measurements. All forward simulations with a fixed size distribution are therefore made for spheroids with a monomodal log-normal size distribution using the estimated effective radius and effective variance as parameters.

The retrieved size distributions do not agree well with the *a priori* estimates. This may be due to the above mentioned limitation of the measured range of scattering angles. We also note that the size distributions retrieved from scattering matrices of the same sample measured at different wavelengths do not coincide. The particle sizes retrieved from the scattering matrices measured at $\lambda = 632.8$ nm tend to be larger than the particle sizes retrieved from the scattering matrices measured at $\lambda = 441.6$ nm. The phase functions measured at the shorter wavelength are more forward-peaked and have a larger contribution at scattering angles $\Theta \leq 5^\circ$. The distribution of particle sizes may therefore be less restricted by the measurements at the shorter wavelength. The fraction of the largest particles in a sample may therefore be underestimated in the retrieval from the measurement at the shorter wavelength.

6.5 Interfering effects

In the discussion of the results we have assumed that the measurement of the scattering matrices are not contaminated with multiple-scattering. The presence of multiple-scattering components in the nephelometer measurements has largely been excluded by a simple test: The dependence of the measured light intensities from the amount of scatterers is nearly linear. The intensity of multiple-scattering components, in contrast, shows a quadratic dependence from the amount of scatterers. A simple calculation of the second order scattering contribution indicates that the discrepancies between the simulated and the measured phase functions that we observe cannot be explained by the presence of such a multiple-scattering component.

Furthermore, we have assumed that the mineral particles in the nephelometer measurement are present as individual particles rather than in the form of aggregates. The formation of aggregates is excluded in the laser particle-sizing experiment by ultrasonic vibrations. In the nephelometer experiment we cannot rule out completely the presence of aggregates. The results from the laser particle-sizing experiment indicate that the clay samples have a smaller effective radius r_{eff} than the quartz sample. A comparison of the steepness of the measured phase functions at the scattering angle $\Theta = 5°$, however, indicates that the clay particles are larger than the quartz particles. The presence of aggregates during the nephelometer measurements of the clay samples is a possible explanation for this inconsistency.

6.6 Conclusion

We have investigated the consistency of measurements and simulations for the scattering matrix of four different irregular mineral dust samples. Simulations are made using the AERONET light scattering database that is based on the spheroidal shape approximation. Simulated scattering matrices differ from the measured scattering matrices in a characteristic way. In most cases when *a priori* estimates for the size distribution and the refractive index are used, the simulations overestimate the phase function in the range of scattering angles from 60° to 90° and underestimate the phase function in the range from 120° to 150°. The element $-F_{12}/F_{11}$ tends to be underestimated while the element F_{22}/F_{11} tends to be overestimated by the simulations. Simulations with variations of the input parameters indicate that these discrepancies cannot be eliminated without assuming unphysical values for the size distribution or the refractive index. The differences between simulations and measurements have a similar amplitude as the differences in the scattering matrices that are compared in the context of radiative transfer simulations in an atmosphere containing mineral aerosol (Ch. 8). This suggests that simulations using the spheroidal shape approximation may introduce errors in aerosol retrievals that rely on the measurement of scattered sunlight. A larger number of samples with well-defined properties is necessary for a quantification of these errors.

With a simultaneous fit of the size distribution, the shape distribution and the complex refractive index $m = n - ik$, simulated scattering matrices are obtained that agree optimally with the measurements in a least-squares sense. The measured phase functions and the elements $-F_{12}/F_{11}$ are reproduced very well by these simulations. The overall differences between the simulated and the measured scattering matrices still exceed the measurement errors. The imaginary part of the retrieved refractive indices tends to be too large. An overestimation of k appears to be necessary in order to reproduce the flat run of the phase function in the range of scattering angles between $\Theta = 60°$ and 170° that is characteristic to light scattering by irregular particles. If the scattering matrix of real dust is simulated, one may consider using an artificially increased value for k. This indicates that the imaginary part of the refractive index of mineral dust aerosol retrieved from scattered sunlight measurements may be systematically overestimated, if direct extinction measurements are not available. This may be the case especially for typical satellite observations of reflected sunlight that is singly-scattered with scattering angles between $\Theta = 60°$ and $\Theta = 170°$. The real part of the retrieved refractive indices is close to the *a priori* estimates. This indicates that retrievals of the real part of the refractive index provide useful results for the distinction of mineral aerosol from other aerosol types. Comparing various mineral samples, we note that the retrieved values do not correlate with the *a priori* estimates. This suggests that it may be difficult or impossible to distinguish between the mineral aerosol types presented based on scattered sunlight observations alone. The retrieval of the size distribution from the measured scattering matrices does not provide meaningful results. This is due to the limited range of scattering angles that excludes the scattering angles close to the forward scattering direction with $\Theta < 5°$.

We observe that a good agreement of the simulated and the measured scattering matrices can be achieved only if some of the input parameters are allowed to take values outside of the range that is assumed to be realistic for the mineral samples. Conversely, if the input parameters are fixed to realistic estimates, the discrepancies between the simulated and the measured scattering matrices increase. We observe the general behavior, that if part of the input parameters are fixed to *a priori* estimates, the retrieved values of the remaining parameters differ from the *a priori* estimates more than if all parameters are used as free fit parameters. This indicates that there is a certain general disagreement between the predictions of the spheroidal shape approximation used here and the measured light scattering properties of truly irregular mineral particles.

Aspect ratios ranging from 0.42 to 2.4 are included in the light scattering model used in this study. T-matrix calculations show that including more extreme aspect ratios in the ensemble of model particles improves the agreement of simulations and measurements (Ch. 8). Including more extreme aspect ratios in the kernel database may improve the consistency of the simulations and the measurements. However, we assume that a part of the inconsistency is due to a general difference between the predictions of the spheroidal shape approximation and light scattering by truly irregular particles.

At present, there is no efficient technique to simulate the light scattering by truly irregular particles. The light scattering techniques that are applicable to irregular shapes with internal inhomogeneities are computationally so demanding that the generation of a practical light scattering database like the AERONET light scattering database is not possible in the near future. The best step to take is therefore to devise new instrumentation, to develop new methods to generate well-defined irregular particle samples, and thus to generate a large experimental light scattering database.

Bibliography

Dubovik, O., and M. D. King, A flexible algorithm for retrieval of aerosol optical properties from sun and sky radiance measurements, *J. Geophys. Res., 105*, 20673–20696, 2000.

Dubovik, O., B. N. Holben, T. F. Eck, A. Smirnov, Y. J. Kaufman, M. D. King, D. Tanré, and I. Slutsker, Variability of absorption and optical properties of key aerosol types observed in worldwide locations, *J. Atmos. Sci., 59*, 590–608, 2002.

Dubovik, O., B. N. Holben, T. Lapyonok, A. Sinyuk, M. I. Mishchenko, P. Yang, and I. Slutsker, Non-spherical aerosol retrieval method employing light scattering by spheroids, *Geophys. Res. Lett., 29*, doi:10.1029/2001GL014506, 51-1, 2002.

Holben, B. N. and coautors, A federated instrument network and data archive for aerosol characterization, *Remote Sens. Environ., 66*, 1–16, 1998.

Huffman, D. R., The interaction of light with a small-particle system, *Adv. Phys., 26*, 129-130, 1977.

Kahn, R., R. West, D. McDonald, B. Rheingans, and M. I. Mishchenko, Sensitivity of multi-angle remote sensing observations to aerosol sphericity, *J. Geophys. Res., 102*, 16861–16870, 1997.

Kahnert, F. M., and A. Kylling, Radiance and flux simulations for mineral dust aerosols: Assessing the error due to using spherical or spheroidal model particles, *J. Geophys. Res., 109*, doi:10.1029/2003JD004318, 2004.

Klein, C., *Manual of Mineral Science, 22nd ed.*, John Wiley, New York, 2002.

Mishchenko, M. I., A. A. Lacis, B. E. Carlson, and L. D. Travis, Nonsphericity of dust-like tropospheric aerosols: implications for aerosol remote sensing and climate modeling, *Geophys. Res. Lett., 22*, 1077–1080, 1995.

Muñoz, O., H. Volten, J. W. Hovenier, B. Veihelmann, W. J. van der Zande, L. B. F. M. Waters, and W. I. Rose, Scattering matrices of volcanis ash particles of Mount St. Helens, Redoubt, and Mount Spurr Volcanoes, *J. Geophys. Res., 109*, D1620110.1029/2004JD004684, 2004.

Nousiainen, T., and K. Vermeulen, Comparison of measured single-scattering matrix of feldspar particles with T-matrix simulations using spheroids, *J. Quant. Spectrosc. Radiat. Transfer, 79-80*, 1031–1042, 2003.

Nousiainen, T., F. M. Kahnert, and B. Veihelmann, Light scattering modeling of small feldspar particles using simplified shapes, *J. Quant. Spectrosc. Radiat. Transfer*, accepted.

Sokolik, I. N., and O. B. Toon, Incorporation of mineralogical composition into models of the radiative properties of mineral aerosol from UV to IR wavelengths, *J. Geophys. Res., 104*, 9423–9444, 1999.

Veihelmann, B., H. Volten, and W. J. van der Zande, Light reflected by an atmosphere containing irregular mineral dust aerosol, *Geophys. Res. Lett., 31*, L04113, 1-4, doi:10.1029/2003GL018229, 2004.

Volten, H., O. Muñoz, E. Rol, J. F. de Haan, W. Vassen, J. W. Hovenier, K. Muinonen, and T. Nousiainen, Scattering matrices of mineral particles at 441.6 nm and 632.8 nm, *J. Geophys. Res., 106*, 17375–17401, 2001.

Chapter 7

Light scattering by small feldspar particles simulated using the Gaussian random sphere geometry

Abstract

The single-scattering properties of Gaussian random spheres are calculated using the discrete dipole approximation. The ensemble of model particles is representative for a sample of weakly-absorbing irregularly-shaped feldspar particles. The morphology of Gaussian random spheres is modeled based on a statistical shape analysis using microscope images of feldspar particles. The orientation-averaged and ensemble-averaged scattering matrices and cross sections are compared with T-matrix calculations for ensembles of oblate and prolate spheroids. The Gaussian random sphere model and the spheroidal shape model are assessed using the measured scattering matrix of the feldspar dust sample as a reference.

7.1 Introduction

Atmospheric aerosols are monitored with ground-based and satellite-based sensors measuring scattered sunlight [*Holben et al.*, 1998; *Kaufman et al.*, 2002]. An accurate knowledge of the light scattering properties of the aerosol is essential for the interpretation of measured intensity and polarization data. In practice, a numerical model is required that describes the cross sections of scattering and absorption as well as the scattering matrix as a function of the refractive index, the size distribution, and the shape of the aerosol particles. A large fraction of aerosol mass present in the Earth atmosphere is irregularly-shaped mineral dust [*D'Almeida et al.*, 1991]. It has been shown in various studies that neglecting the nonsphericity of mineral aerosol particles can yield large errors of simulated radiances and retrieved aerosol parameters [*Mishchenko et al.*, 1995; *Kahn et al.*, 1997; *Kalashnikova and Sokolik*, 2002]. In a recent study it has been shown as well that simulated radiation flux data can be erroneous if irregular aerosol particles are approximated by spheres [*Kahnert and Kylling*, 2004]. In order to take the nonsphericity of mineral aerosol into account in light scattering simulations, shape approximations are used. Irregular aerosol particles may be represented by ensembles of simple non-spherical shapes such as spheroids, prisms, cylinders or more complex shapes [*Bohren and Huffmann*, 1983]. The single-scattering properties of these model particles must then be calculated using numerical light scattering codes which in general impose constraints on the ensemble of model particles [cf. *Mishchenko et al.*, 2002].

The single-scattering properties of aerosol are usually expressed in terms of the cross sections for scattering c_{scat} and absorption c_{abs} and the scattering matrix **F**. The cross sections describe the probability of a scattering or an absorption process to occur. For convenience, we will use as well the scattering efficiency $Q_{\mathrm{scat}} = c_{\mathrm{scat}}/(\pi r_{\mathrm{v}}^2)$ defined as the ratio of the scattering cross section and the projected area of the volume-equivalent sphere with the radius r_{v}. The scattering matrix is used to simulate the change of the intensity and the polarization of light in a single-scattering process. The intensity and the polarization of a light beam is characterized by the Stokes vector $\mathbf{I}$ = (I,Q,U,V). Its elements represent the total intensity (I) and linearly (Q and U) and circularly (V) polarized components. The scattering matrix **F** relates the Stokes vectors of incident light $\mathbf{I}_{\mathrm{in}}$ and scattered light $\mathbf{I}_{\mathrm{sc}}$ in a single scattering process by

$$\mathbf{I}_{\mathrm{sc}} \propto \mathbf{F} \cdot \mathbf{I}_{\mathrm{in}} \tag{7.1}$$

[e.g. *Bohren and Huffmann*, 1983]. The scattering matrix **F** has the block diagonal form

$$\mathbf{F}(\boldsymbol{\Theta}) = \begin{pmatrix} F_{11}(\Theta) & F_{12}(\Theta) & 0 & 0 \\ F_{12}(\Theta) & F_{22}(\Theta) & 0 & 0 \\ 0 & 0 & F_{33}(\Theta) & F_{34}(\Theta) \\ 0 & 0 & -F_{34}(\Theta) & F_{44}(\Theta) \end{pmatrix} \tag{7.2}$$

for ensembles of randomly-oriented scatterers that include particles and mirror particles in equal numbers. Scattering matrices of natural, randomly-oriented, irregularly-shaped aerosol particles usually have this block-diagonal form. The matrix elements depend on the scattering angle Θ, i.e. the angle between incoming and scattered beam. The scattering angle $\Theta = 0°$ denotes forward scattering.

Measured scattering matrices can be used as reference for testing numerical models and shape approximation used for the simulation of light scattered by small irregular particles. *Volten et al.* [2001] have experimentally determined the scattering matrix of many irregularly-shaped mineral dust samples with a so-called nephelometer experiment (see Chapter 4). The scattering matrix elements $F_{ij}(\Theta)$ of dust samples are measured in the range of scattering angles from 5° to 173° at the wavelengths $\lambda = 441.6$ nm and $\lambda = 632.8$ nm. The measurement of a feldspar sample has been used in a number of validation studies of this kind. The feldspar sample originates from grinding a bulk crystal. The refractive index of feldspar is estimated to be $m = 1.57 - 0.0005\mathrm{i}$. The real part is taken from *Huffman* [1977] while the imaginary part is adopted from other weakly absorbing silicate minerals (mica) [*Sokolik and Toon*, 1999]. The size distribution is estimated based on a light scattering measurement using a laser particle sizer. The estimates for the effective radius and the effective variance are $r_{\mathrm{eff}} = 1\ \mu$m and $v_{\mathrm{eff}} = 1$ respectively [for definition see *Hansen and Travis*, 1974]. According to the refractive index and the size distribution, the feldspar sample is representative for weakly-absorbing atmospheric mineral aerosol [*Dubovik et al.*, 2002; *Tratt et al.*, 2001; *Maring et al.*, 2003].

A widely-used approach is to represent irregular aerosol particles by an ensemble of rotationally symmetric spheroids with various aspect ratios. The aspect ratio $\epsilon = a/b$ is defined by the length of the symmetry axis b and the length of an axis a that is orthogonal to the symmetry axis. The single-scattering properties of small spheroidal particles can be calculated using the T-matrix code [*Mishchenko*, 1991]. *Nousiainen and Vermeulen* [2003] have compared T-matrix calculations for a mixture of prolate and oblate spheroids with the feldspar measurement. An equiprobable shape distribution is used, i.e. particles with different aspect ratios are assumed to be present in equal numbers. Based on the same reference measurement, *Veihelmann et al.* [2004] have investigated the impact of shape approximations on polarimetric satellite observations including their sensitivity with respect to the optical thickness and the single-scattering albedo of the aerosol. *Nousiainen et al.* [2004] have derived an optimal estimate as well as a practical parameterization for the aspect ratio distribution based on the feldspar measurement. *Kahnert et al.* [2004] applied this parameterization as well as the measured phase function of the feldspar sample for atmospheric radiance and flux simulations in the visible.

The conclusion of these studies is that the spheroidal shape approximation constitutes a major improvement over the spherical shape approximation for the simulation of light scattered by irregular particles. The agreement between measured and simulated scattering matrices depends critically on the aspect ratio distribution. The optimal estimate for the aspect ratio distribution derived by *Nousiainen et al.* [2004] for the feldspar sample strongly weights the more extreme spheroids while the weight of the nearly spherical shapes is reduced. Systematic differences remain between the measured scattering matrices and the simulations based on the spheroidal shape approximation. These discrepancies may be related to the symmetry of the model particles which is not found for natural mineral aerosol particles. The discrepancies may as well be due to the absence of inhomogeneities in the model particles, or to the absence of small scale structures in the shapes of the model particles.

We investigate whether the simulation of light scattering by irregular aerosol particles can be improved by using model shapes with no axis or plane of symmetry. We statistically model the morphology of the feldspar sample based on objective observations of true irregular particle shapes using the Gaussian random sphere geometry [*Muinonen et al.*, 1996] (Section 7.2). In the general formalism, Gaussian random spheres have no symmetry. In that sense, the statistical shape model using Gaussian random spheres is more representative for natural irregular particles than the spheroidal shape approximation. The ensemble of model particles used for the light scattering simulations is representative for the feldspar sample regarding the refractive index, the size distribution, and the particle shape. The statistical shape parameters of the feldspar particles are extracted from Scanning Electron Microscope (SEM) images of the mineral sample. For this purpose, we use a method discribed by *Nousiainen et al.* [2003] and *Nousiainen and McFarquhar* [2004]. Using this strategy, *Nousiainen et al.* [2003] have simulated light scattering by Gaussian random spheres representing large Sahara dust particles with a modified ray-optics approximation. Due to the limitations of the modified ray-optics approximation, this study accounts for model particles representing large soil-derived airborne particles in dust storms with typical volume-equivalent radii of $r_{\mathrm{v}} = 8$ μm. In the study presented here we consider small particles that are representative for tropospheric aerosol in background conditions with typical volume-equivalent radii of $r_{\mathrm{v}} = 1$ μm.

The orientation-averaged scattering matrix, the cross sections of scattering and absorption of the Gaussian random spheres are calculated using the discrete dipole approximation (DDA) at a wavelength of $\lambda = 632.8$ nm (Section 7.3). This matches one of the wavelengths used in the nephelometer measurements. The simulations of light scattering by Gaussian random spheres at this wavelength are confined to particles with volume-equivalent sphere radii $r_{\mathrm{v}} \leq 1.3$ μm due to the computational burden of DDA calculations for large particles. Firstly, we investigate the agreement and the differences between the Gaussian random sphere model and the spheroidal shape approximation which is introduced in Section 7.4. For this purpose, we use T-matrix calculations for ensembles of prolate and oblate spheroids with the same refractive index and the same particle volume. For the shape averaging we use parameterized shape distributions including a parameterization that was optimized for the feldspar sample by *Nousiainen et al.* [2004]. In Section 7.5 the comparison is presented for individual size classes.

The simulated scattering matrices are size-averaged using the size distribution of the feldspar sample. With the DDA calculations we include about 86% of the total scattering cross section of the feldspar sample. With the simulations for spheroidal particles 97% of the total effective scattering cross section is accounted for. We merge the DDA simulations for Gaussian random spheres with radii r_{v} ranging from 0.1 μm to 1.4 μm with T-matrix simulations for spheroids with radii r_{v} ranging from 1.4 μm to 2.6 μm. This enables us to assess the Gaussian random sphere model and the spheroidal model using the measured scattering matrix of the feldspar sample as reference (Section 7.6).

7.2 Gaussian random sphere geometry

Natural mineral aerosol particles are irregular in the sense that there is no simple function that could describe their shape. We use the Gaussian random sphere geometry [*Muinonen et al.*, 1996; *Muinonen*, 2000] to model the statistical properties of the shapes of the feldspar dust sample. The Gaussian random sphere is a statistical shape described by the radius r as a function of the spherical coordinates θ and ϕ

$$r(\theta, \phi) = \frac{a}{\sqrt{1+\sigma^2}} \exp(s(\theta, \phi)) \tag{7.3}$$

and depends on the mean radius a, the relative standard deviation of the radius σ, and the logradius s

$$s(\theta, \phi) = \sum_{l=0}^{\infty} \sum_{m=-l}^{l} s_{lm} Y_{lm}(\theta, \phi), \tag{7.4}$$

which is the sum of spherical harmonic functions Y_{lm}

$$Y_{lm}(\theta, \phi) = P_{lm}(\cos(\theta)) e^{im\phi} \tag{7.5}$$

that are weighted with the complex coefficients s_{lm}. P_{lm} denote the associated Legendre-functions. The complex coefficients s_{lm} have zero mean values and a variance

$$\mathrm{Var(Real(s_{lm}))} = (1 + \delta_{\mathrm{m0}})\frac{2\pi}{2\mathrm{l}+1}\mathrm{C_l} \tag{7.6}$$

$$\mathrm{Var(Imag(s_{lm}))} = (1 - \delta_{\mathrm{m0}})\frac{2\pi}{2\mathrm{l}+1}\mathrm{C_l} \tag{7.7}$$

for $l = 0, 1, 2, ..., \infty$ and $m = -l, ..., l$ [see *Nousiainen et al.*, 2001]. Note that the variance of the coefficients s_{lm} depends only on the coefficient C_l of the same order l.

The coefficients C_l are related to the covariance function $\Sigma_r(\gamma)$ of the radius $r(\gamma)$ of an intersection of the Gaussian random sphere. The radius r is measured from the geometric center of the intersection as a function of the polar angle γ. The covariance function of the radius is a measure of the particle morphology. Naturally, the covariance function $\Sigma_r(\gamma)$ of a sphere is a constant. For non-spherical shapes Σ_r has a maximum at $\gamma = 0$. The shape features have a certain scale. The smaller this scale, the faster $\Sigma_r(\gamma)$ drops with increasing angle γ from its maximum value $\Sigma_r(0) = \sigma$. The covariance function Σ_r of the radius is related to the covariance function of the logradius Σ_s

$$\Sigma_s = \ln(\Sigma_r + 1), \tag{7.8}$$

which can be expanded in a series of Legendre-functions

$$\Sigma_s(\gamma) = \sum_{l=0}^{\infty} C_l P_l(\cos(\gamma)), \tag{7.9}$$

where the sum of the coefficients C_l equals the variance of the logradius β^2, viz.

$$\sum_{l=0}^{\infty} C_l = \beta^2 = \ln(1 + \sigma^2). \tag{7.10}$$

By analogy with the concepts used in Fourier-analysis, the coefficients C_l can be regarded as a power spectrum of the logradius. The shape of a Gaussian random sphere is isotropic in the sense that the covariance function of a Gaussian random sphere is independent of the orientation of the intersection. That is why an ensemble of generated Gaussian random sphere realizations is randomly oriented.

We generate a finite ensemble of Gaussian random sphere realizations with shape statistics that are representative for the feldspar sample following the approach described by *Nousiainen et al.* [2003] and *Nousiainen and McFarquhar* [2004]. We determine the ensemble-averaged covariance function $\Sigma_r(\gamma)$ of many feldspar particles in order to obtain an estimate for the statistical properties of the feldspar particles. The particle intersections of the feldspar particles cannot be measured with the devices available. Instead we analyze the particle projections taken from Scanning Electron Microscope (SEM) images. The radius $r(\gamma)$ of the projections of more than 200 particles is evaluated. The morphology of the feldspar sample is now captured in terms of the ensemble-average of the series of coefficients C_l. The coefficients C_l extracted from the SEM images of the feldspar sample follow reasonably well the power law relation $C_l = l^{-\nu}$ with $\nu = 2.5$. We obtain a value of 0.2 for the parameter σ. A morphology analysis of a Sahara dust sample yields a similar power law relation with the parameter $\nu = 4$ [*Nousiainen et al.*, 2003]. According to the exponent ν, the shapes of the Sahara dust particles are more rounded than the shapes of the feldspar particles. This finding is in agreement with the shapes observed on microspcope images of both dust samples.

A part of the information regarding the fine structure of the particle surfaces is lost when using the particle projections instead of the particle intersection. This is partly due to shadowing effects. Therefore, we cannot extract the high-order Legendre-coefficients C_l from the particle projections. We extrapolate the series of coefficients to an order up to $l_{\max} = 15$ using the power law relation mentioned above following the approach described in *Nousiainen et al.* [2003]. Including even higher order contributions has very little impact on the particle shape.

The coefficients s_{lm} in Eq. (7.4) with $l \leq 1$ are mainly responsible for a variation of the particle volume. These coefficients are set to zero in order to generate an ensemble of Gaussian random spheres realizations with a controlled volume. The remaining variance of the particle volume is small and acceptable for our purposes. The ensemble-averaged volume $\langle V \rangle$ is

$$\langle V \rangle = \frac{4}{3} a^3 \exp[3 \ln(\sigma^2 + 1)] \tag{7.11}$$

[*Muinonen*, 1998]. With the parameter $\sigma = 0.2$, the ensemble of generated Gaussian random sphere realizations has a very narrow distribution with an effective radius of $r_{\text{eff}} = 1.04a$ and an effective variance of about $v_{\text{eff}} = 0.0002$.

7.3 Light scattering by Gaussian random spheres

We have tested two numerical codes for the calculation of the single-scattering properties of Gaussian random spheres with linear dimensions comparable to the wavelength. This includes the code DDSCAT 6.1 which is based on the discrete dipole approximation [*Draine and Flatau*, 1994], and SScaTT which is based on computing the T-matrix with the null-field method using discrete sources [*Wriedt and Doicu*, 1998]. The convergence of DDSCAT is less sensitive with respect to the particle shape than SScaTT. Furthermore, we were able to compute a larger range of particle sizes with DDSCAT. That is why we chose the discrete dipole approximation for the light scattering calculations based on the Gaussian random sphere model.

In the discrete dipole approximation the target is replaced by an array of dipoles with a chosen polarizability. The electro-magnetic response of each dipole is determined as a function of the external field and the fields scattered by all other dipoles [*Purcell and Pennypacker*, 1973]. Targets are generated as 3-dimensional arrays of dipoles with a

Gaussian random sphere realization as an envelope [*Muinonen et al.*, 1996]. The volume-equivalent sphere radius of each particle is derived from the number of dipoles [*Draine and Flatau*, 2004]. The elements of the scattering matrix are calculated accurately (with errors less than a few %) if the condition

$$|m|\frac{2\pi}{\lambda}d < 0.5 \tag{7.12}$$

is satisfied [*Draine and Flatau*, 2004]. This poses an upper limit to the lattice spacing d of the dipole array. The required number of dipoles for a spherical particle with a given radius and a refractive index, $m = 1.57 - 0.001\mathrm{i}$ can be estimated by

$$N \approx 100 \cdot x^3, \tag{7.13}$$

where $x = 2\pi r_\mathrm{v}/\lambda$ is the size parameter. The largest particle size we can take into account is therefore limited by the internal memory of the computers used, and by the computing time that increases dramatically with increasing number of dipoles.

The light scattering problem is solved for 196 target orientations. The scattering matrices, the scattering efficiency and the absorption efficiency are averaged over all orientations. The scattering matrices of all shapes in each size class are averaged using the scattering cross sections as weight. Measured scattering matrices of large ensembles of natural irregular shapes have the block diagonal form given in Eq. (7.2). This indicates that the measured particle ensemble has no chirality, as it is the case when particles and mirror particles are present in equal numbers. For each Gaussian particle of the ensemble we include as well the mirror particle. With this we ensure that the ensemble of Gaussian particles with a limited number of individual shapes with no plane of symmetry has no chirality. For size classes with a volume-equivalent radius $r_\mathrm{v} \leq 1$ μm we include 50 pairs of particles and mirror particles. For the size classes with larger radii, not more than 10 particles are used due to computation time reasons. With the computational resources available, the light scattering by particles with volume-equivalent radii up to 1.3 μm are simulated at a wavelength of $\lambda = 632.8$ nm. In total, we have invested more than 6 months of computing (CPU) time in the DDA calculations.

All scattering matrices that were obtained in this work have been tested for consistency. The Cloude test is satisfied for all scattering angles [*Hovenier and Van der Mee*, 2000]. The conditions for the scattering angles 0° and 180° given by *Hovenier and Van der Mee* [1996] are also satisfied.

7.4 Spheroidal shape approximation

The widely-used spheroidal shape approximation is used to put the results of the Gaussian random sphere model into context. The scattering matrix and the cross sections for scattering and extinction of an ensemble of randomly oriented spheroids are calculated using the T-matrix code developed by *Mishchenko* [1991]. This code is based on calculating the

T-matrix using the null-field method. The spheroidal shapes can be characterized by the shape parameter ξ

$$\xi = \begin{cases} \epsilon - 1 & : \quad \epsilon \geq 1 \quad \text{(oblate)} \\ 1 - \frac{1}{\epsilon} & : \quad \epsilon < 1 \quad \text{(prolate)} \end{cases} \tag{7.14}$$

where ϵ of an oblate (prolate) spheroid is defined as the ratio of the major to the minor (minor to major) axis length. Following *Nousiainen et al.* [2004], a parameterized shape distribution $h_n(\xi)$ is used for the shape averaging

$$h_n(\xi) = \begin{cases} C\,|\xi^n| & : \quad \xi_{\text{min}} \leq \xi \leq \xi_{\text{max}} \\ 0 & : \quad \text{otherwise} \end{cases} \tag{7.15}$$

where C is a normalization constant. This shape distribution gives more weight to the extreme shapes with increasing parameter n. We consider spheroidal shape models with the equiprobable shape distribution with $n = 0$, and the shape distributions with $n = 1$ and $n = 3$. In the following, these shape approximations will be referred to as spheroidal-ξ^n models. The shape distribution of the spheroidal-ξ^3 models strongly weights the extreme aspect ratios while the near-spherical shapes are suppressed. The value $n = 3$ was found to be optimal for the feldspar sample *Nousiainen et al.* [2004]. We include spheroids with shape parameters ξ ranging from -2 to 2 in equidistant steps. This corresponds to aspect ratios ϵ between 1/3 and 3.

7.5 Size-specific results

The single-scattering properties simulated using the Gaussian random sphere model are compared with simulations using spheroidal models with various shape distributions. We compare the simulations for particles with the same volume. This is a commonly used approach for small particles with typical dimensions smaller than the wavelength. The surface area is more appropriate for describing the size of larger particles [e.g. *Bohren and Huffmann*, 1983]. In this study we consider size distributions that include significant contributions in both size domains. It is desirable to characterize consistently the size of all particles. To this end, we chose the particle volume since the surface area of the Gaussian random spheres is much more difficult to determine. Light scattering calculations are made for 22 size classes with radii ranging from $r_{\text{v}} = 0.01$ μm to $r_{\text{v}} = 1.3$ μm at a wavelength of $\lambda = 632.8$ nm. The radii are evenly spaced on a logarithmic scale. The model particles of each size class of the Gaussian random sphere model have an effective variance of about 0.0002. The T-matrix simulations for spheroids are therefore made for narrow log-normal size distributions with the same variance. We simulate the light scattering by spheroidal particles for size classes with effective size parameters x ranging from 0.01 to 26.

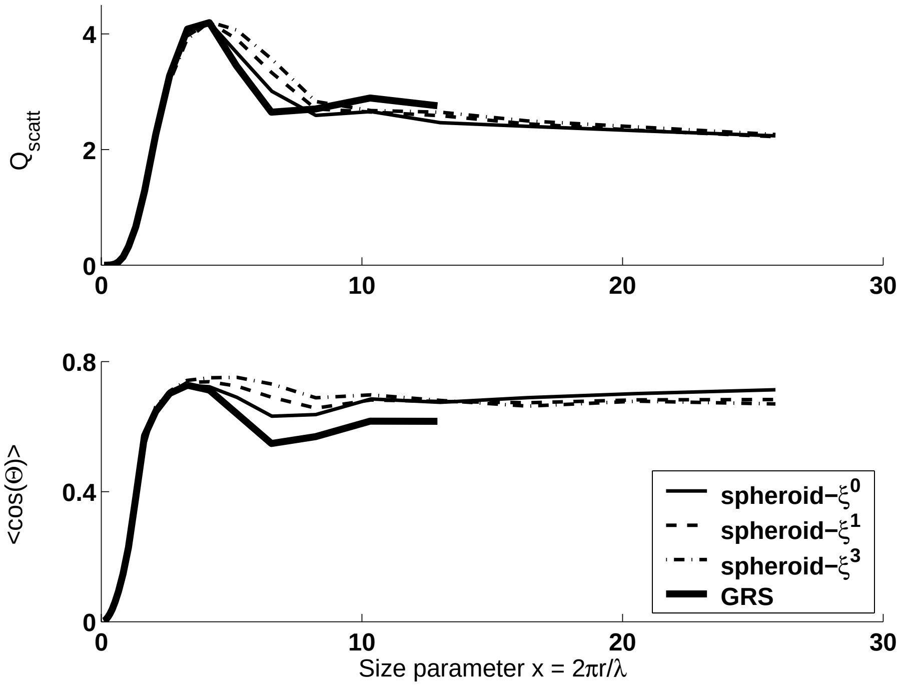

Figure 7.1: Simulated scattering efficiency Q_{scat} and asymmetry parameter $g = \langle\cos(\Theta)\rangle$ for Gaussian random spheres (thick solid) and mixtures of prolate and oblate spheroids (thin lines) with the shape distributions ξ^0 (solid), ξ^1 (dashed), and ξ^3 (dash-dotted).

In Fig. 7.1, the simulated scattering efficiency $Q_{\text{scat}} = c_{\text{scat}}/(\pi r_{\text{v}}^2)$ and the asymmetry parameter g are shown for the Gaussian random sphere model (thick solid) and the spheroidal models with $n = 0$ (thin solid), $n = 1$ (thin dashed), and $n = 3$ (thin dash-dotted) as a function of the size parameter x. The asymmetry parameter g

$$g = \langle\cos(\Theta)\rangle = \frac{\int_0^\pi \cos(\Theta)\sin(\Theta)F_{11}(\Theta)d\Theta}{\int_0^\pi \sin(\Theta)F_{11}(\Theta)d\Theta} \tag{7.16}$$

is the average cosine of the scattering angle. This parameter is used in radiation flux simulations. The higher its value the more light is scattered into directions with $\Theta > 90°$. The asymmetry parameter vanishes if the scattering is symmetric with respect the scattering angle $\Theta = 90°$. The asymmetry parameters and the scattering efficiency Q_{scat} of all shape models coincide for size parameters up to $x = 4$. For larger sizes ($x \geq 7$), the spheroidal models predict a larger scattering efficiency than the Gaussian random sphere model. In the size range with $5 < x < 10$, the scattering efficiency of the spheroidal model with $n = 0$ fits best to the results of the Gaussian random sphere model. The same holds in the size range $5 < x < 8$ for the asymmetry parameter.

In Figure 7.2 the simulated scattering matrices of particles with a size parameter $x = 10$ are depicted. This plot shows the variation of scattering matrices of the ensemble of Gaussian random spheres in one size class. The results of the Gaussian random sphere model are depicted as the mean values of the matrix elements of 100 model shapes (thick solid lines). The gray shaded areas indicate the 1-σ environment of the ensemble. The non-zero elements of the scattering matrices are shown as a function of the scattering angle Θ.

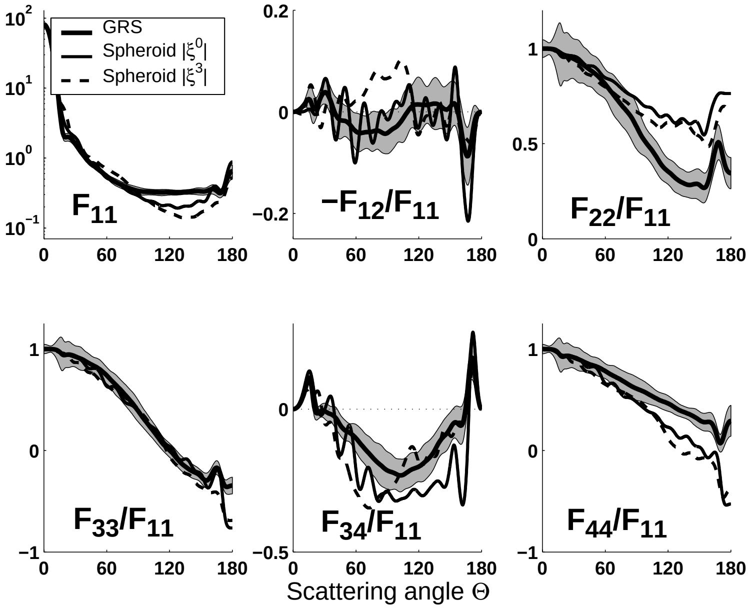

Figure 7.2: Simulated scattering matrix of Gaussian random spheres with a size parameter $x = 10$ and a refractive index of $1.57 - 0.0005i$ (thck solid). The gray shaded areas depict the 1-σ environment of the matrix elements of 100 model shapes. The scattering matrices of mixtures of prolate and oblate spheroids with the same refractive index and the same volume are shown. We include spheroids with aspect ratios ranging from 1/3 to 3 with the equi-probable shape distribution (thin solid) and the spheroidal-ξ^3 model where the nonspherical shapes have a stronger weight (dashed).

Note that the phase function $F_{11}(\Theta)$ is plotted on a logarithmic scale and is normalized using the condition

$$\frac{1}{2}\int_0^\pi \sin(\Theta)F_{11}(\Theta)d\Theta = 1. \tag{7.17}$$

The scattering matrices of the spheroidal models with $n = 0$ (thin solid) and $n = 3$ (thin dashed) are included. The differences between the scattering matrices of the spheroidal models and the Gaussian random sphere model exceed the standard deviations in all elements at various scattering angles. The differences between the shape models are therefore regarded as significant. Note that the phase function close to 140° of the Gaussian random sphere model exceeds the phase functions of the spheroidal-ξ^3 model by a factor up to 2.

The differences between the scattering matrices of the Gaussian random sphere model and the spheroidal model depend on the particle size, the shape distribution used in the spheroidal model, the matrix element, and the scattering angle. In Figure 7.3 the elements $F_{11}(\Theta)$, $F_{12}(\Theta)/F_{11}(\Theta)$, and $F_{22}(\Theta)/F_{11}(\Theta)$ of simulated scattering matrices are shown. We include results of the Gaussian random sphere model (thick solid), and the spheroidal models (thin) for the size parameters of $x_\mathrm{v} = 1.7$, 4.1 and 12.8. The simulated scattering matrices of particles with a size parameter close to $x = 0.1$ are similar to the scattering matrix of Rayleigh scattering. For these particle sizes, the scattering matrices of the Gaussian random spheres and the spheroids coincide. The Gaussian model and the spheroidal model agree well in the phase function F_{11} at scattering angles close to the forward scattering direction for all particle sizes considered. For $x > 2$, the phase function of the spheroidal-ξ^3 model has lower values than the phase function of the Gaussian random sphere model in the range of scattering angles $100° < \Theta < 150°$. In this range of scattering angles, the phase functions differ by a factor of up to 1.5 ($x = 1.7$), 1.7 ($x = 4.1$), and 2 ($x = 12.8$). The largest differences in $-F_{12}/F_{11}$ between the Gaussian random sphere model and the spheroidal-ξ^3 model are observed for size parameters close to $x = 2$ (not shown). The spheroidal models show a similarity with the Gaussian random sphere model in the shape of $-F_{12}/F_{11}$ for size parameters up to $x = 6.5$ (not shown). All models considered predict $-F_{12}/F_{11}$ to decrease in amplitude and to exhibit more peaks and dips with increasing particles size.

The element F_{22}/F_{11} at angles $\Theta > 60°$ is known to be very sensitive with respect to the particle nonsphericity. For spherical particles, F_{22}/F_{11} is unity for all scattering angles. The values of F_{22}/F_{11} decrease with increasing nonsphericity especially in the range of scattering angles from 100° to 160°. For size parameters $x < 2.6$, the Gaussian random sphere model predicts higher values than the spheroidal models. The opposite is true for $x > 2.6$. Light scattering in the size range from about $x = 1$ to $x = 2.6$ appears to be insensitive to the fine structure of the particle shapes. The non-spherical character appears to be determined rather by the global oblateness or prolateness of the shapes.

We note that the spheroidal model with $n = 0$ agrees better with the Gaussian random sphere model than the spheroidal-ξ^3 model regarding the simulated scattering matrix in the size range between $x = 1$ and $x = 6$. For larger sizes, the differences between the Gaussian random sphere model and the spheroidal models have a similar amplitude as the differences between the spheroidal-ξ^0 and the spheroidal-ξ^3 models.

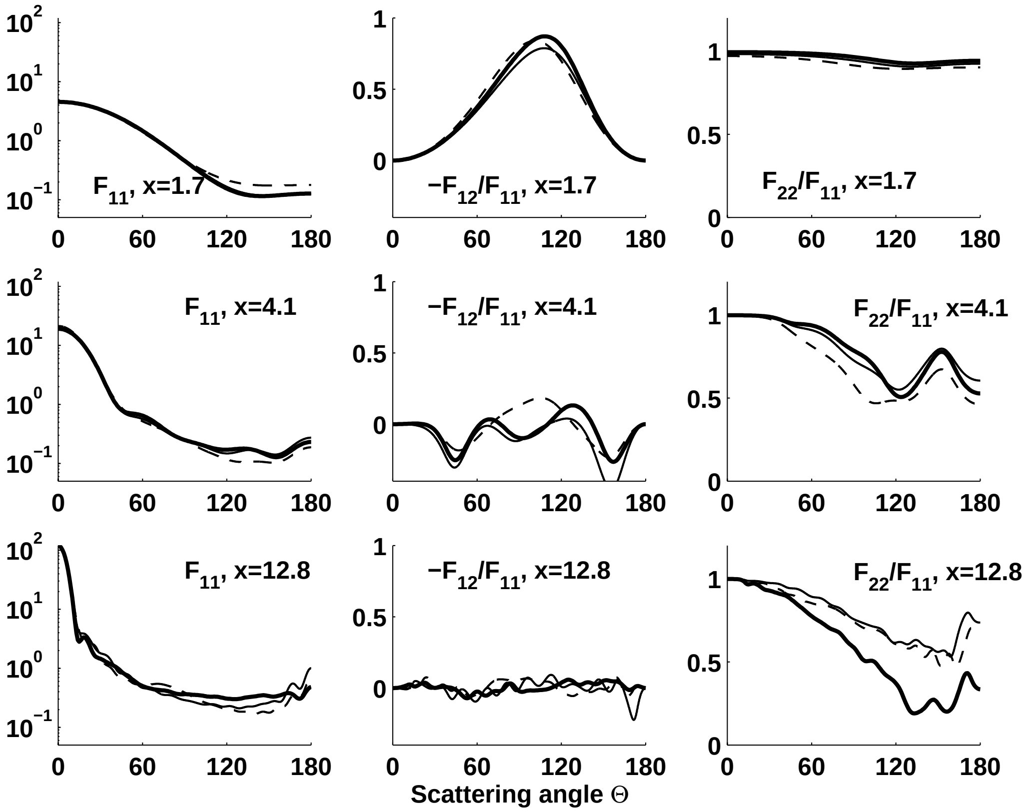

Figure 7.3: Simulated phase function (F_{11}) and the elements F_{12}/F_{11} and F_{22}/F_{11} of the scattering matrix of Gaussian random spheres. We show the matrix elements for ensembles of 100 Gaussian random spheres shapes with a refractive index of $1.57 - 0.0005i$ with the size parameters $x = 1.7$, $x = 4.1$, and $x = 12.8$ (thick solid). The results are compared with simulations for mixtures of prolate and oblate spheroids with the same volume-equivalent sphere radius. We include spheroids with aspect ratios ranging from 1/3 to 3 with the equi-probable shape distribution (thin solid) and the spheroidal-ξ^3 model (thin dashed).

The differences between the scattering matrices of individual sizes simulated using the various models are large enough to affect radiative transfer simulations [for comparison see *Kahnert et al.*, 2004; *Nousiainen et al.*, 2004]. A comparison of the models with an independent objective reference is therefore relevant.

7.6 Size-averaged results

In order to compare the simulated scattering matrices with the feldspar measurement, the simulations are size-averaged using the size distribution of the feldspar sample. We use a log-normal size distribution with an effective radius $r_{\text{eff}} = 1$ μm and an effective variance $v_{\text{eff}} = 1$. This size distribution is consistent with the size distribution of the feldspar sample derived in Chapter 5.

As discussed in Section 7.3, the light scattering simulations for Gaussian random spheres are confined to volume-equivalent sphere radii smaller than $r \leq 1.3$ μm. Therefore, it is important to estimate the fraction of the total scattering cross section of the dust sample that is accounted for by the simulations. To this end, the scattering cross section of spheroidal particles with the spheroidal-ξ^3 model are determined for a large range of particle sizes. The cross sections of spheroids with aspect ratios ranging from 1/3 to 3 and with volume-equivalent sphere radii up to 100 μm are calculated using a light scattering model developed by *Min et al.* [2003]. In this way, the total scattering cross section of the entire distribution can be compared to the total cross section of truncated size distributions. Using the Gaussian random sphere model we account for 86% of the total scattering cross section of the feldspar sample. With the spheroidal models, particles with volume equivalent sphere radii up to 2.6 are included. With this, 97% of the total scattering cross section of the sample is taken into account.

We investigate whether the simulations of light scattering by Gaussian random spheres can be extended to larger particle sizes using the ray-optics approximation (ROA). To this end, scattering matrices of Gaussian random spheres with a size parameter $x = 26$ are calculated using the ray-optics approximation. This approximation is applicable to weakly-absorbing spherical particles with size parameters $x \geq 80$. This size limit decreases with increasing nonsphericity of the scatterers. A comparison of simulations with various models for the size parameters $x = 13$ and $x = 26$ indicates that the ROA provides useful values for the phase function for Gaussian random spheres with size parameter of $x = 26$ (Figure 7.4). The phase functions of spheroids with the sizes parameters $x = 13$ (dotted) and $x = 26$ (dashed) are very similar except for scattering angles close to $\Theta = 0$. The same is true for DDA calculations for Gaussian random spheres with a size parameter $x = 13$ (thin solid) and ROA calculations for Gaussian random spheres with a size parameter $x = 26$ (thick solid). The phase functions of the Gaussian random spheres are significantly flatter than the phase functions of the spheroidal particles for both size parameters. The phase function of particles in this size range appear to be rather insensitive with respect to the particle size. Based on this notion we may conclude that ROA calculations for the phase function at a size parameter $x = 26$ capture the features that are characteristic for the Gaussian random sphere geometry. For the other elements, the comparison of the scattering matrices does not provide the basis for a conclusive statement of this kind.

The feldspar sample has only a negligible fraction of the total scattering cross section in the size range where it is known for sure that ROA simulations produce reliable results for the entire scattering matrix. That is why the DDA simulations for Gaussian random spheres are extended to larger sizes using the results of the spheroidal-ξ^3 model. An effec-

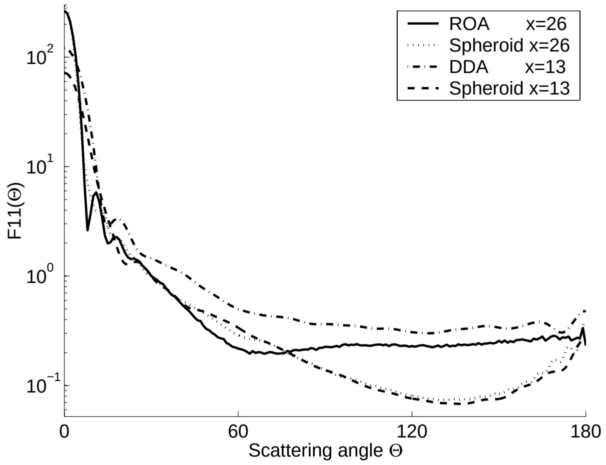

Figure 7.4: Simulated phase functions (F_{11}) using DDA for Gaussian random spheres with $x = 13$ (dash-dotted), ROA for Gaussian random spheres with $x = 26$ (solid), and the spheroidal-ξ^3 model for $x = 13$ (dashed) and $x = 26$ (dotted).

tive scattering matrix is considered that comprises contributions from Gaussian random spheres with volume-equivalent sphere radii $r \leq 1.3$ μm and from spheroids with radii between 1.3 μm and 2.6 μm. Another valid approach would be to compare the DDA simulations for Gaussian random spheres directly with the measured scattering matrix keeping in mind that 14% of the total scattering cross section of the sample is not accounted for in the simulations. Both approaches are equivalent, since the merged scattering matrix is very similar to the result using the Gaussian random sphere model with the truncated size distribution.

In Figure 7.5 we compare the merged scattering matrix (thick solid) with the results of the spheroidal-ξ^0 model (thin solid), the spheroidal-ξ^3 model (thin dashed), and the measurement (solid line with dots). The phase function of the Gaussian random sphere model is flat in the range of scattering angles from 100° to 170°. This is characteristic for phase functions of irregular mineral particles and has been observed in many measurements of mineral dust samples [*Volten et al.*, 2005]. The simulated phase functions of the spheroidal models show a broad dip with a minimum between $\Theta = 120°$ and 140°. The Gaussian random sphere model as well as the spheroidal-ξ^0 model overestimate the phase function for scattering angles $\Theta > 60°$. Close to $\Theta = 150°$ both models overestimate the phase function by a factor of 1.7. A variation of the size distribution shows that

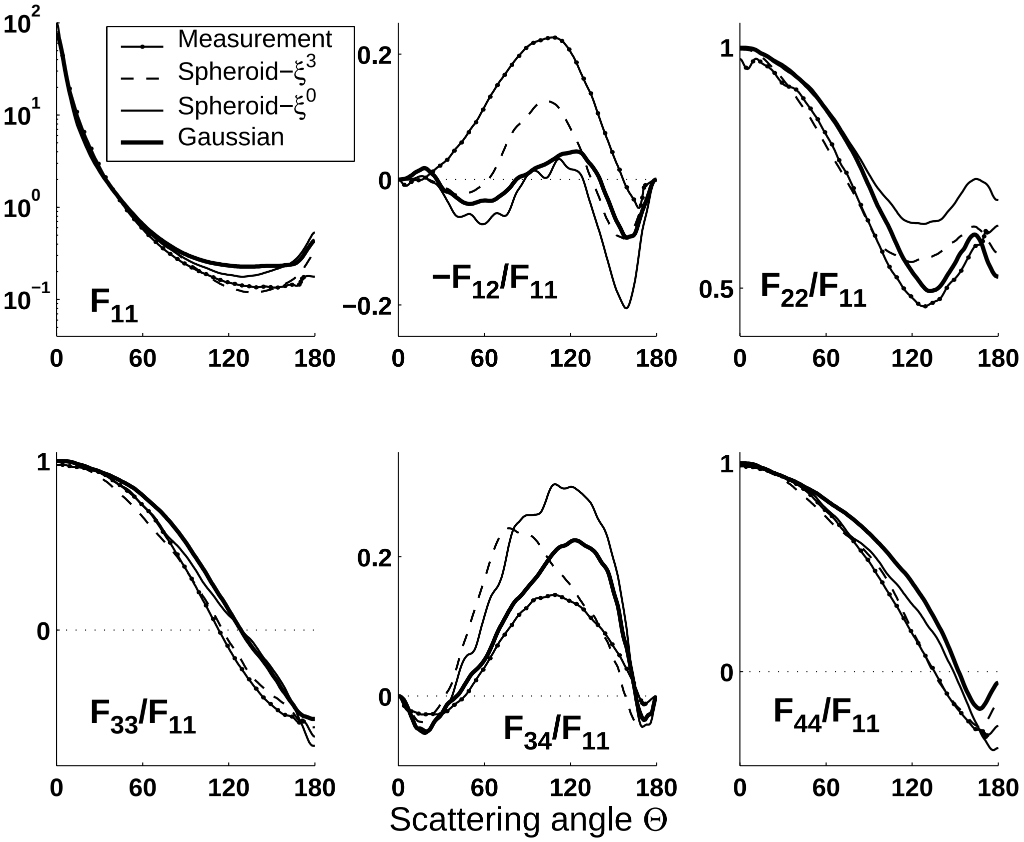

Figure 7.5: Size-averaged scattering matrices using the Gaussian random sphere model (thick solid), the spheroidal-ξ^0 model (thin solid), and the spheroidal-ξ^0 model (thin dashed) are compared with the measured scattering matrix (solid line with dots).

this overestimation cannot be caused by an error in the size distribution alone. None of the models tested here captures the large values of the element $-F_{12}/F_{11}$ in the sideward scattering directions. For the element $-F_{12}/F_{11}$, the result of the Gaussian random sphere model lies between the results of the spheroidal models at most scattering angles. Note that the simulated values of F_{22}/F_{11} using the Gaussian random sphere model are close to the measured values, especially in the range of scattering angles from 120° and 160°. In this respect, the non-sphericity of the Gaussian random spheres appears to be adequate for the feldspar dust sample.

The differences between the scattering matrix of the Gaussian random sphere model and the results from the spheroidal models are in the same order of magnitude as the differences between the results from the spheroidal models. The best agreement with the measured phase function could be achieved with the spheroidal-ξ^3 model. This is true for the phase function, for $-F_{12}/F_{11}$ in the sideward scattering directions, for F_{22}/F_{11} at scattering angles $\Theta \leq 110°$, for F_{33}/F_{11} and F_{44}/F_{11}. The Gaussian random sphere model shows a better agreement with the measurement only for F_{22}/F_{11} at $120° < \Theta < 160°$ and for F_{34}/F_{11} at $40° < \Theta < 100°$.

7.7 Conclusions

The single-scattering properties of an ensemble of Gaussian random spheres are calculated using the discrete dipole approximation. The ensemble of Gaussian random spheres is representative for a feldspar dust sample regarding the morphology, the refractive index as well as the size distribution. The obtained scattering properties are compared with T-matrix calculations for various shape distributions of prolate and oblate spheroids. This includes an equiprobable shape distribution (spheroidal-ξ^0 model) and a shape distribution that has been optimized for the feldspar measurement (spheroidal-ξ^3 model). The size-averaged scattering matrices are compared with the measured scattering matrix of the feldspar sample.

The simulated scattering cross sections and scattering matrices of individual sizes, defined by the particle volume, agree very well for small particle sizes. The largest differences between the scattering cross section simulated using the Gaussian random sphere model and the spheroidal models are found in the size range between $x = 5$ and $x = 10$. In this size range the scattering cross sections of the Gaussian random sphere model agree best with the results of the spheroidal model with an equiprobable shape distribution. For the scattering matrix, the differences tend to increase with increasing particle size. In the size range from $x = 1$ to $x = 6$ the Gaussian random sphere model agrees best with the spheroidal model with an equiprobable shape distribution.

After size-averaging, the simulated scattering matrices are compared with the measured scattering matrix of the feldspar sample. Overall, the spheroidal-ξ^3 model agrees better with the measurements than the Gaussian random sphere model. In various respects, the Gaussian random sphere model reflects the light scattering properties predicted by the spheroidal-ξ^0 model, which comprises larger contributions of rounded shapes. On the other hand, the Gaussian random sphere model renders best the flat shape of the phase function in the range of scattering angles from 100° to 170°, and the F_{22}/F_{11} element between $\Theta = 120°$ and $\Theta = 170°$. These features are characteristic for light scattering by truly irregular mineral dust particles.

The Gaussian random sphere model has been applied, especially in order to capture the nonspherical and nonsymmetric nature of the particle shapes. However, the Gaussian random sphere geometry cannot reproduce the sharp edges and the flat surfaces of the feldspar particles that are observed on microscopic images. The relative phases of the spherical harmonic functions that are required to reproduce the exact shapes of true particles are not taken into account. This may explain why the light scattering predicted by the Gaussian random sphere model shows similarities with the light scattering of more rounded shapes in various respects. Differences between the measurement and the simulations shown in the study may as well be due to small-scale structures of the surface and inhomogeneities in the volume of mineral dust particles that are not accounted for in any of the models used. Until light scattering by true mineral aerosols can be reproduced accurately by models, light scattering measurements remain a benchmark relevant for further developments.

Bibliography

Bohren, C. F., and D. R. Huffman, *Absorption and Scattering of Light by Small Particles*, ed. J. Wiley, New York, 1983.

D'Almeida, G. A., P. Koepke, and E. P. Shettle, *Atmospheric Aerosol Global Climatology and Radiative Characteristics*, Deepak Publ., 1991.

Draine, B. T., and J. P. Flatau, Discrete-dipole approximation for scattering calculations, *J. Opt. Sc. Am. A, 11*, 1491–1499, 1994.

Draine, B. T., and J. P. Flatau, User Guide for the Discrete Dipole Approximation Code DDSCAT 6.1, http://arxiv.org/abs/astro-ph/0309069, 2004.

Dubovik et al., Variability of absorption and optical properties of key aerosol types observed in worldwide locations, *J. of the Atmos. Sci., 59*, 590–608, 2002.

Hansen, J. E., L. D. Travis, Light scattering in planetary atmospheres, *Space Sci. Rev., 16*, 527–610, 1974.

Holben, B. N., and coautors, A federated instrument network and data archive for aerosol characterization, *Remote Sens. Environ., 66*, 1–16, 1998.

Hovenier, J. W., and C. V. M. van der Mee, Basic relationships for matrices describing scattering by small particles, chapter in *Light scattering by nonspherical particles: Theory, Measurements, and Applications*, edt. M. I. Mishchenko, J. W. Hovenier, and L. D. Travis, Academic Press, San Diego, 61–85, 2000.

Hovenier, J. W., and C. V. M. van der Mee, Testing scattering matrices: a compendium of recipes, *J. Quant. Spectrosc. Radiat. Transfer, 55*, 649–661, 1996.

Huffman, D. R., The interaction of light with a small-particle system, *Adv. Phys., 26*, 129–130, 1977.

Kaufman, Y. J., D. Tanré, and O. Bouché, A satellite view of aerosols in the climate system, *Nature, 419*, 215–223, 2002.

Kahn, R., R. West, D. McDonald, B. Rheingans, and M. I. Mishchenko, Sensitivity of multi-angle remote sensing observations to aerosol sphericity, *J. Geophys. Res., 102*, 16861–16870, 1997.

Kahnert, F. M., J. J. Stamnes, and K. Stamnes, Can simple particle shapes be used to model scalar optical properties of an ensemble of wavelength-sized particles with complex shapes?, *J. Opt. Soc. Am. A, 19*, 521–531, 2002.

Kahnert, F. M., and A. Kylling, Radiance and flux simulations for mineral dust aerosols: Assessing the error due to using spherical or spheroidal model particles, *J. Geophys. Res., 109*, doi:10.1029/2003JD004318, errata: doi:10.1029/2004JD005311, 2004.

Kahnert, F. M., T. Nousiainen, and B. Veihelmann, Spherical and Spheroidal model particles as an error source in aerosol climate forcing and radiation computations: a case study for feldspar aerosols, *J. Geophys. Res.*, submitted.

Kalashnikova, O., and I. Sokolik, Modeling the radiative properties of nonspherical soil-derived mineral aerosols, *J. Quant. Spectrosc. Radiat. Transfer, 87*, 137–166, 2004.

Kalashnikova, O., and I. Sokolik, Importance of shape and composition of wind-blown dust particles for remote sensing at solar wavelengths, *Geophys. Res. Lett., 29*, 10.1029/2002GL014947, 2002.

Maring, H., D. L. Savoie, M. A. Izaguirre, L. Custals, and J. S. Reid, Mineral dust aerosol size distribution change during atmospheric transport, *J. Geophys. Res., 108*, doi:10.1029/2002JD002536, PRD8, 1–6, 2003

Min, M., J. W. Hovenier, and A. de Koter, Scattering and absorption cross sections for randomly oriented spheroids of arbitrary size, *J. Quant. Spectrosc. Radiat. Transfer, 79*, 939-+, 2003

Mishchenko, M. I., L. D. Travis and A. A. Lacis, *Scattering, Absorption, and Emission of Light by Small Particles*, Cambridge University Press, New York, 2002.

Mishchenko, M. I. , J. W. Hovenier, L. D. Travis, T-matrix method and its applications, chapter in *Light Scattering by Nonspherical Particles*, ed. M. I. Mishchenko, J. W. Hovenier and L. D. Travis, Academic Press, San Diego, 147–172, 2000.

Mishchenko, M. I., and L. D. Travis, Capabilities and limitations of a current FORTRAN implementation of the T-matrix method for randomly oriented, rotationally symmetric scatterers, *J. Quant. Spectrosc. Radiat. Transfer, 60*, 309–324, 1998.

Mishchenko, M. I., A. A. Lacis, B. E. Carlson, and L. D. Travis, Nonsphericity of dust-like tropospheric aerosols: implications for aerosol remote sensing and climate modeling, *Geophys. Res. Lett., 22*, 1077–1080, 1995.

Mishchenko, M. I., Light scattering by randomly oriented axially symmetric particles, *J. Opt. Soc. Am. A, 8*, 871–882, 1991.

Muinonen, K. , Light scattering by stochastically shaped particles, chapter in *Light scattering by Nonspherical Particles*, edited by M. I. Mishchenko, J. W. Hovenier, and L. D. Travis, pp. 323–352, Academic Press, San Diego, 2000.

Muinonen, K., Introducing the Gaussian shape hypothesis for asteroids ad comets, *Astron. Astrophys., 332*, 1087–1098, 1998.

Muinonen, K., T. Nousiainen, P. Fast, K. Lumme and J. I. Peltoniemi, Light scattering by Gaussian Random Particles: Ray optics approximation, *J. Quant. Spectrosc. Radiat. Transfer, 55*, 577–601, 1996.

Muñoz, O., H. Volten, J. W. Hovenier, B. Veihelmann, W. J. van der Zande, L. B. F. M. Waters, and W. I. Rose, Scattering matrices of volcanis ash particles of Mount St. Helens, Redoubt, and Mount Spurr Volcanoes, *J. Geophys. Res., 109*, D1620110.1029/2004JD004684, 2004.

Nousiainen, T., and G. M. McFarquhar, Light scattering by quasi-spherical ice crystals, *J. Atmos. Sci., 61*, 2229–2248, 2004.

Nousiainen, T., M. Kahnert, and B. Veihelmann, Light scattering modeling of small feldspar particles using simplified shapes, *J. Quant. Spectrosc. Radiat. Transfer*, accepted.

Nousiainen, T., and K. Vermeulen, Comparison of measured single-scattering matrix of feldspar particles with T-matrix simulations using spheroids, *J. Quant. Spectrosc. Radiat. Transfer, 79-80*, 1031–1042, 2003.

Nousiainen, T., K. Muinonen, and P. Räisänen, Scattering of light by large Saharan dust particles in a modified ray-optics approximation, *J. Geophys. Res., 108*, doi:10.1029/2001JD001277, 2003.

Nousiainen, T., K. Muinonen, J. Avelin, and A. Sivola, Microwave backscattering by nonspherical ice particles at 5.6 GHz using second-order perturbation series, *J. Quant. Spectrosc. Radiat. Transfer, 70*, 639–663, 2001.

Purcell, E. M., and C. R. Pennypacker, Scattering and Absorption of Light by Nonspherical Dielectrical Grains, *Astrophysical J., 186*, 705–714, 1973.

Sokolik, I. N., and O. B. Toon, Incorporation of mineralogical composition into models of the radiative properties of mineral aerosol from UV to IR wavelengths, *J. Geophys. Res., 104*, 9423–9444, 1999.

Tratt, D. M., R. J. Frouin, and D. L. Westphal, April 1998 Asian dust event: A southern Californian perspective, *J. Geophys. Res., 106*, 18371–18379, 2001.

Veihelmann, B., H. Volten, and W. J. van der Zande, Light reflected by an atmosphere containing irregular mineral dust aerosol, *Geophys. Res. Lett., 31*, L04113, 1-4, doi:10.1029/2003GL018229, 2004.

Volten, H., O. Muñoz, E. Rol, J. F. de Haan, W. Vassen, J. W. Hovenier, K. Muinonen, and T. Nousiainen, Scattering matrices of mineral particles at 441.6 nm and 632.8 nm, *J. Geophys. Res., 106*, 17375–17401, 2001.

Volten, H., O. Muñoz, J. W. Hovenier, J. F. de Haan, W. Vassen , W. J. van der Zande, and L. B. F. M. Waters, WWW scattering matrix database for small mineral particles at 441.6 nm and 632.8 nm, *J. Quant. Spectrosc. Radiat. Transfer, 90*, 191–206, 2005.

Waterman, P. C., Numerical solutions of electromagnetic scattering problems. In *Computer Techniques for Electromagnetics*, ed. R. Mittra, 97–157, Pergamon Oxford, 1973.

Wriedt, T., and U. Comberg, Comparison of computational scattering models, *J. Quant. Spectrosc. Radiat. Transfer, 60*, 411–423, 1998.

Wriedt, T., and A. Doicu, Formulation of the extended boundary condition method for three-dimensional scattering using the method of discrete sources, *J. Modern Optics, 45*, 199–214, 1998.

Chapter 8

Light Reflected by an Atmosphere Containing Irregular Mineral Dust Aerosol

Abstract

We simulate polarimetric satellite observations of sunlight reflected by a turbid atmosphere over the ocean. We determine the sensitivity of these observations with respect to the optical thickness and the single-scattering albedo of irregular mineral aerosol. Simulated results indicate that both quantities can be retrieved from simultaneous polarization and intensity measurements. Aerosol scattering is modelled using a true measured scattering matrix of irregularly-shaped mineral dust aerosol. We study the suitability of various approximations of the particle shape used for the numerical calculation of scattering matrices. Approximations with spheres or spheroids with a distribution of moderate axis ratios can lead to large errors of the simulated light intensities. A spheroidal approximation including extreme axis ratios is found to be the most appropriate one for simulations of light scattering by irregular mineral aerosol particles if measured scattering matrices are not available.

8.1 Introduction

Mineral dust aerosols influence the Earth's radiation budget by reflection and absorption of solar radiation. Scattering processes increase the photon path length and enhance gaseous absorption. Dust aerosols play a vital role in cloud formation processes and, by virtue of their large surface area, control many heterogeneous reactions in the atmosphere. The dust is mainly raised in dry lakebeds in the Sahara, east Asia and the Saudi Arabian deserts and can be transported over distances of more than thousand kilometers [*Husar et al.*, 1997]. The amount of dust raised and the atmospheric residence time depend strongly on the meteorological conditions and depend amongst others on the size of the particles [*Nho et al.*, 1996]. Satellite observations of reflected sunlight are used to monitor dust aerosols and to estimate their climatic effect. However, the retrieval of the aerosol load as well as its microphysical properties from satellite measurements of reflected sunlight [e.g. *Masuda et al.*, 2002] remains difficult. For a unique solution, multi-spectral multi-angle measurements including both the intensity as well as the polarization are necessary [*Chowdhary et al.*, 2001].

We study the sensitivity of simultaneous observations of the intensity and the polarization with respect to the aerosol optical thickness and the single-scattering albedo. Furthermore, we specify viewing geometries that are essential for the separation of both quantities. For this purpose, we simulate the Earth's reflectance for a model atmosphere over the ocean loaded with mineral dust aerosol. Aerosol retrievals require an accurate knowledge of the aerosol scattering described by a scattering matrix and the scattering cross section which depend on the refractive index, the size, and the shape of the particles. We model aerosol scattering based on an accurately measured scattering matrix of a mineral dust sample [*Volten et al.*, 2001] that is representative for atmospheric mineral aerosol. The dust sample includes a large variety of highly irregular shapes as we observed on SEM-graphs (not shown).

In many applications scattering matrices are determined numerically. However, for irregularly-shaped mineral aerosol this calculation is so time consuming that it is practically impossible. In practice, a dust aerosol is often approximated with an ensemble of spheres or spheroids with a distribution of sizes and axis ratios. Spherical scatterers can be treated according to the Lorenz-Mie theory. For spheroidal particles the T-matrix method is applicable [*Mishchenko et al.*, 2000], albeit with constraints that are due to computing time and convergence criteria of the numerical code [*Mishchenko and Travis*, 1998]. We compare the measured scattering matrix with calculations for ensembles of particles with the projected area equivalent size distribution and the refractive index of the dust sample (section 8.2). Firstly, we use a spherical shape approximation. Secondly, we approximate the aerosol with an ensemble of randomly oriented oblate and prolate spheroids with moderate axis ratios. Finally, we consider a distribution of spheroidal shapes that includes extreme axis ratios up to the convergence limit of the quadruple precision version of the T-matrix code for each size. We estimate the suitability of the shape approximations for aerosol retrievals. For this purpose, we use the reflectance simulations based on the measured scattering matrix as a reference and compare them with simulations based on calculated scattering matrices (section 8.3).

8.2 Scattering matrices

A light beam is characterized by the Stokes vector $\mathbf{I}$ = (I,Q,U,V). Its elements represent the total intensity (I) and linearly (Q and U) and circularly (V) polarized components with the units W/m^2/sr. A single-scattering process is described by the matrix multiplication

$$\mathbf{I}_{scat} \propto \mathbf{F}\,\mathbf{I}_{in}. \tag{8.1}$$

$\mathbf{I}_{in}$ and $\mathbf{I}_{scat}$ are the Stokes vectors of the incoming and the scattered light. For an ensemble of randomly-oriented scatterers, where particles and their mirror particles are present in equal numbers, the scattering matrix $\mathbf{F}$ has the block diagonal form

$$\mathbf{F}(\Theta) = \begin{pmatrix} F_{11}(\Theta) & F_{12}(\Theta) & 0 & 0 \\ F_{12}(\Theta) & F_{22}(\Theta) & 0 & 0 \\ 0 & 0 & F_{33}(\Theta) & F_{34}(\Theta) \\ 0 & 0 & -F_{34}(\Theta) & F_{44}(\Theta) \end{pmatrix} \tag{8.2}$$

and depends on the scattering angle Θ, i.e. the angle between incoming and scattered beam. The scattering angle $\Theta = 0°$ denotes forward scattering. *Volten et al.* [2001] have experimentally determined the scattering matrix elements $F_{ij}(\Theta)$ of a feldspar dust sample. The refractive index of feldspar is estimated to be $m = 1.57 - 0.0005\text{i}$. The real part is taken from *Huffman* [1977], while the imaginary part is adopted from other weakly absorbing silicate minerals (mica) [*Sokolik and Toon*, 1999]. The size distribution measured is characterized by an effective radius $r_{eff} = 1$ μm and a standard deviation $\sigma_{eff} = 1$ [for definition see *Hansen and Travis*, 1974]. The dust sample is representative for weakly absorbing silicate aerosol [see *Dubovik et al.*, 2002]. The matrix elements have been measured at the wavelength 632.8 nm in the range of scattering angles from 5° to 173° with intensities relative to the intensity at $\Theta = 30°$. Since the full range of scattering angles from 0° to 180^o is required for radiative transfer simulations, we extend the scattering element $F_{11}(\Theta)$ according to a method suggested by *Liu et al.* [2003]. In the forward-scattering direction the scattering of small particles with moderate aspect ratios is dominated by Fraunhofer diffraction and is largely the same as for projected area equivalent spheres. Hence, we merge the Lorenz-Mie result from 0° to 5° with the measured $F_{11}(\Theta)$ that is extrapolated to 180°, and scale the measurement until the standard normalization condition

$$\frac{1}{2}\int_0^{\pi} F_{11}(\Theta) sin(\Theta) d\Theta = 1 \tag{8.3}$$

is met. For the relative scattering matrix elements $F_{ij}(\Theta)/F_{11}(\Theta)$ a cubic spline extrapolation is used for both the forward and the backscattering direction. Forward and backscattering values are determined consistent with the conditions given by *Hovenier and Van der Mee* [1996] such that they allow the elements $F_{ij}(\Theta)/F_{11}(\Theta)$ to run smoothly towards 0° and 180° and satisfy the Cloude test at all angles.

For comparison, we consider 3 types of numerically determined scattering matrices. Firstly, the irregularly-shaped aerosol is approximated with an ensemble of spherical particles with the projected area equivalent size distribution of the dust sample. The scattering matrix is then calculated using the Lorenz-Mie theory. Secondly, the irregularly-shaped aerosol is approximated with an ensemble of randomly oriented oblate and prolate spheroids [*Bohren and Huffmann*, 1983]. Scattering matrices are determined using the T-matrix method [*Mishchenko et al.*, 2000] for a simple distribution of moderate axis ratios (major/minor ≤ 2) that does not vary with the particle size. Thirdly, we consider a distribution that includes extreme axis ratios up to the convergence limit of the quadruple precision version of the T-matrix code for each size. The maximum axis ratio for which convergence is achieved decreases with the particle size. In Table 8.1 the maximum axis ratio is given as a function of the size parameter $x = 2\pi r/\lambda$ given for the projected

Axis ratio:	15	9	6	3.5	2	1.2
Size parameter:	1	5	10	20	50	80

Table 8.1: Maximum axis ratios, where convergence is achieved.

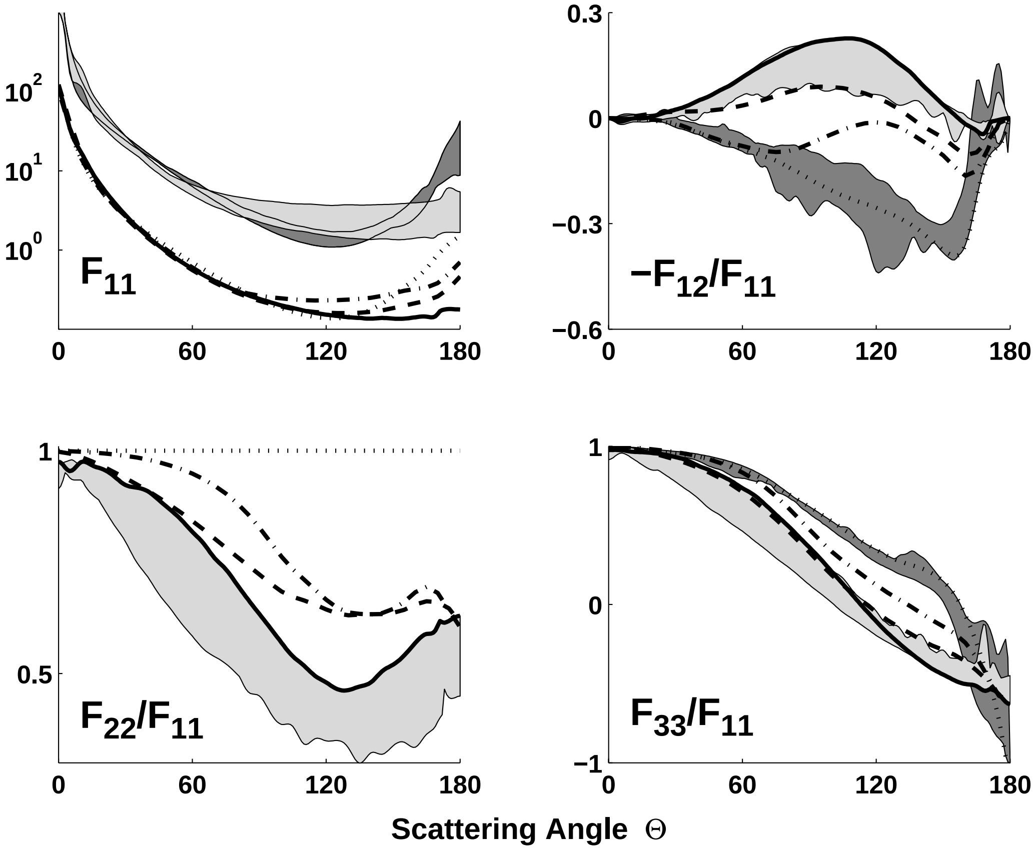

Figure 8.1: The measured scattering matrix elements $F_{11}(\Theta)$, $-F_{12}(\Theta)/F_{11}(\Theta)$, $F_{22}(\Theta)/F_{11}(\Theta)$ and $F_{33}(\Theta)/F_{11}(\Theta)$ of feldspar dust (solid) are compared with calculations based on shape approximations with spheres (dotted) and spheroids including moderate (dash-dotted) and extreme (dashed) axis ratios. The areas (shifted by a factor of 10 in the upper left graph) show that the mismatch of measurements (ligth gray) with Lorenz-Mie calculations for spheres with a projected area equivalent size distribution (dark gary) is found as well for other irregular mineral dust samples.

area equivalent radius r and a wavelength of 632.8 nm. Scattering matrices are determined for 31 sizes and up to 20 axis ratios. The ensemble average scattering matrix is obtained by weighting with the scattering cross sections and the normalized size distribution of the dust sample. We assume an equiprobable distribution of axis ratios on a logarithmically equidistant grid.

Lorenz-Mie calculations (dotted in Figure 8.1) for the estimated refractive index of the dust sample show a poor agreement with the measured results (solid), especially for F_{11} from 120° to 180° and for $-F_{12}/F_{11}$. This disagreement is found for all irregularly-shaped mineral dust samples measured by *Volten et al.* [2001] and *Muñoz et al.* [2001], as indicated by the gray shaded areas. The agreement with the measurement improves when the particle shapes are approximated with spheroids with moderate axis ratios (dash-dotted). Especially for achieving the bell shape of the element $-F_{12}/F_{11}$ it is essential to incorporate extreme axis ratios (dashed). The element F_{22}/F_{11} obtained from T-matrix calculations shows a peak around 160° that is not present in the measurements. This has been observed as well by *Nousiainen and Vermeulen* [2003]. T-matrix calculations of *Zakharova and Mishchenko* [2001] indicate that discrepancies of the element F_{22}/F_{11} will not vanish by taking into account even more extreme aspect ratios.

The measured scattering matrix, including the elements F_{34}/F_{11} and F_{44}/F_{11} (not shown), is rendered best, when extreme axis ratios are included. We tried various modifications of both the shape as well as the size distribution, but none of them significantly improves the agreement with the scattering matrix measured. The discrepancy may be partly or entirely due to the fundamental difference between scattering by irregular and by spheroidal particles.

We find similar differences between true and calculated scattering matrices for the feldspar sample presented as well as for other aerosol samples with different properties, i.e. a green clay sample ($r_{\mathit{eff}} = 1.5, m = 1.52 - 0.001\mathrm{i}$) and a quartz sample ($r_{\mathit{eff}} = 2.4, m = 1.54 - 0\mathrm{i}$). We estimate the spheroidal shape approximation including small particles with extreme axis ratios to be of practical use for the simulation of light scattering by atmospheric irregular mineral aerosol.

8.3 Simulations

We simulate satellite observations of the intensity and the polarization of sunlight reflected by a turbid atmosphere over a rough oceanic water interface at a wavelength of 632.8 nm. The radiative transfer model is based on the doubling-adding method [*De Haan et al.*, 1986] and includes multiple scattering and polarization. We incorporated a module describing the reflection by an oceanic surface [see *Mishchenko and Travis*, 1997]. The roughness of the water interface is dependent on the near-surface wind speed. We assume a low wind speed of 0.5 m/s in order to avoid a broad sun glint. The atmosphere is sampled by 5 homogeneous plane-parallel layers. Each layer is characterized by the scattering matrix, the single-scattering albedo and the optical thickness of the aerosol. Molecular scattering is described by Rayleigh scattering with a depolarization factor of 0.0310 for air [*Hansen and Travis*, 1974], while molecular absorption is neglected.

We present simulations of reflected sunlight for a solar zenith angle of 30° and various viewing angles within the principal plane. Figure 8.2 shows simulations with the viewing angles −30°, +15°, +45°, and +60°. The nadir is at 0° and the peak of the sun glint is observed at the viewing angle +30° (not shown). The polarization is represented by the

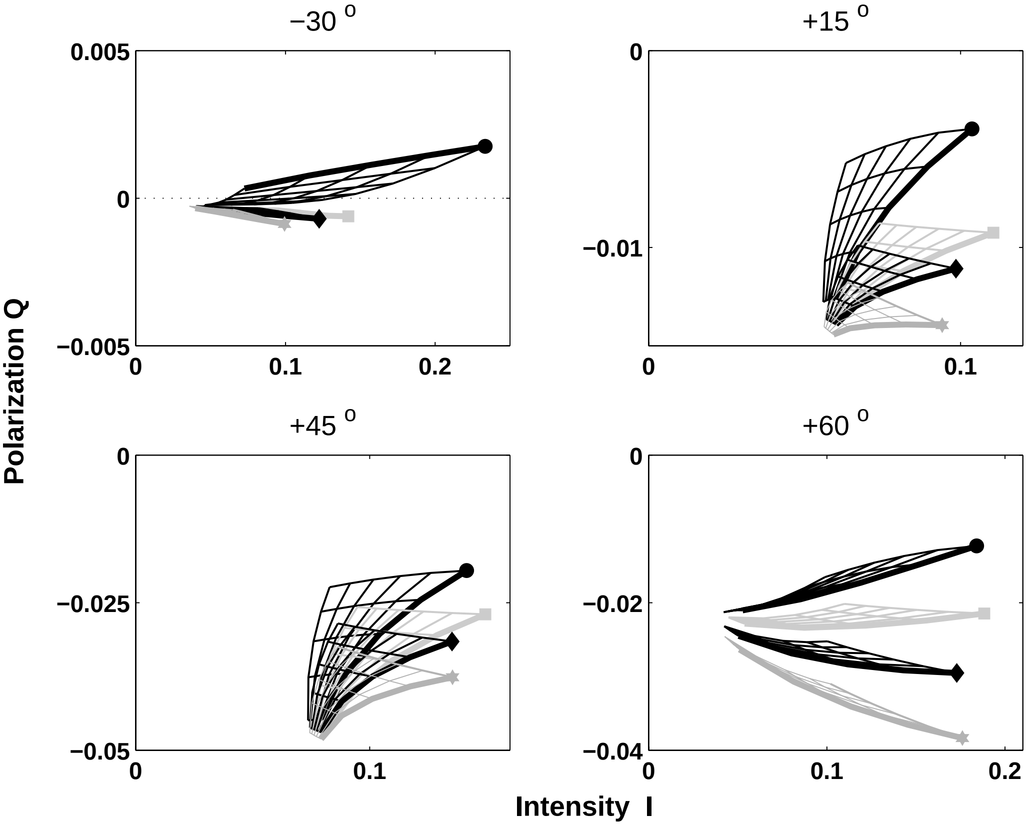

Figure 8.2: Simulations of the intensity I (abscissa) and the polarization Q (ordinate) of reflected sunlight. The grids represent variations of the aerosol optical thickness and the single-scattering albedo. The thick lines indicate a single-scattering albedo of 1; the markers denote an aerosol optical thickness of 0.5. Simulations using the measured scattering matrix (dark gray, marked with asterisks) are compared with simulations based on shape approximations with spheres (black, bullets) and spheroids including moderate (light gray, squares) and extreme axis ratios (black, diamonds).

Stokes parameter Q (ordinate) and is plotted against the total intensity I (abscissa). Both parameters are given as radiances in $\mathrm{W/m^2/sr}$ for an unpolarized incident solar flux of π $\mathrm{W/m^2}$ measured perpendicular to the incoming direction. The Stokes parameter U is zero due to the symmetry of the scenario.

We study the sensitivity of these satellite observations with respect to the aerosol optical thickness and the single-scattering albedo. Simulations are shown as grids representing the variation of both the aerosol optical thickness [0.1, 0.2,..., 0.5] and the single-scattering albedo [0.8, 0.84,..., 1]. An aerosol optical thickness of this order of magnitude is often observed in the lee of deserts [*Díaz et al.*, 2001]. The range of single-scattering albedos is chosen according to an imaginary part of the refractive index ranging from 0 (e.g. for quartz) up to 0.02 (e.g. for volcanic ash [*Patterson*, 1981]). The single-scattering albedo of the feldspar sample is close to unity according to its estimated refractive index. For the simulations based on the measured scattering matrix, we vary the single-scattering albedo without modifying the scattering matrix. This is justified by comparisons of scattering matrices of various samples; we find that differences due to the refractive index are significantly smaller than differences due to the particle shapes used. For all calculated scattering matrices we use the refractive indices that correspond to the various values of the single-scattering albedo. Simulations using the measured scattering matrix are depicted in dark gray and are marked with asterisks. These results are compared to simulations based on shape approximations with spheres (black, bullets) and spheroids including moderate (light gray, squares) and extreme axis ratios (black, diamonds).

The polarization and the intensity of reflected sunlight are determined by aerosol scattering, Rayleigh scattering and the surface reflection. As a consequence, the parameter Q has small values at the viewing angle −30° (i.e. backscattering geometry); the small non-zero values are due to multiple scattering and to reflections from the ocean surface. The presence of aerosol increases the intensity of the reflected light. The dependence of this intensity on the aerosol optical thickness is sensitive to the particle shape. This is especially pronounced at viewing angles close to −30°. In this geometry the intensity is overestimated by up to 135% when irregular particles are approximated as spheres and by up to 42% or 23% when using the spheroidal shape approximation including moderate or extreme axis ratios respectively.

The presence of aerosol reduces the surface reflection that dominates the polarization observed in geometries where the sun glint contributes to the signal. This leads to an increase of the Stokes parameter Q. When the surface reflection is not too strong, the decrease of the surface reflection is overcompensated by the increase of the aerosol scattering. This is the case for the viewing angles +15° and +45°. Here the lines of constant aerosol optical thickness and lines of constant single-scattering albedo are nearly orthogonal. This is not the case for other geometries, e.g. at viewing angles −30°, −15° (not shown), 0° (not shown) and +60°, where the area spanned by the two variations is degenerated to a narrow stripe.

8.4 Conclusion

Both the polarization and the intensity of reflected sunlight are sensitive to the shape of the particles. This indicates that the retrieval of the amount and the properties of mineral aerosol from satellite observations requires an appropriate description of the particle shape. This is in agreement with the findings of *Deuzé (private communications)* who use the intensity and the polarization of reflected sunlight observed by POLDER-ADEOS-1 (POLarization and Directionality of the Earth's Reflectance, [*Deuzé et al.*, 1999]). He found that in cases when mineral dust is present the retrieval of the aerosol optical thickness can be significantly improved by using an average scattering matrix based on scattering matrices measured by *Volten et al.* [2001] instead of Lorenz-Mie calculations.

Simultaneous observations of the polarization and the intensity are sensitive to the single-scattering albedo as well as the aerosol optical thickness. Such observations in geometries where the sun glint contributes weakly to the observed signal provide independent information about the single-scattering albedo and the aerosol optical thickness, provided that the specular reflection is described accurately.

Based on our sensitivity studies, we conclude that the aerosol optical thickness and the single-scattering albedo retrieved using the observation geometries studied, may comprise large error contributions, if the particle shape is approximated by spheres or spheroids with moderate axis ratios. Polarimetric observations of light scattered by irregular mineral aerosol appear to be best, although not perfectly represented by simulations using the spheroidal shape approximation including small particles with extreme axis ratios. The presented results indicate that the use of measured scattering data instead of simulated data using simple shape approximations has the potential to improve aerosol retrievals and radiative forcing estimates.

Bibliography

Bohren, C. F., and D. R. Huffman, *Absorption and Scattering of Light by Small Particles*, John Wiley, New York, 1983.

Chowdhary, J., B. Cairns, M. I. Mishchenko and L. D. Travis, Retrieval of aerosol properties over the ocean using multispectral and multiangle photopolarimetric measurements from the research scanning polarimeter, *Geophys. Res. Lett., 28*, 243–246, 2001.

De Haan, J. F., P. B. Bosma, and J. W. Hovenier, The adding method for multiple scattering calculations of polarized light, *Astron. Astrophys., 183*, 371–391, 1986.

Deuzé, J.-L., M. Herman, P. Gouloub, D. Tanré and A. Merchand, Characterization of aersols over ocean from POLDER-ADEOS-1, *Geophys. Res. Lett., 26*, 1421–1425, 1999.

Díaz, J. P., F. J. Expósito, C. J. Torres and F. Herrera, Radiative properties of aerosols in sahara dust outbreaks using ground-based and satellite data: application to radiative forcing, *J. Geophys. Res., 106*, 18403–18416, 2001.

Dubovik, O., B. N. Holben, T. F. Eck, A. Smirnov, Y. J. Kaufman, M. D. King, D. Tanré, and I. Slutsker, Variability of absorption and optical properties of key aerosol types observed in worldwide locations, *J. of the Atmos. Sci., 59*, 590–608, 2002.

Hansen, J. E., and L. D. Travis, Light scattering in planetary atmospheres, *Space Sci. Rev., 16*, 527–610, 1974.

Hovenier, J. W., and C. V. M. van der Mee, Testing scattering matrices: a compendium of recipes, *J. Quant. Spectrosc. Radiat. Transfer, 55*, 649–661, 1996.

Husar, R. B., J. M. Prospero, and L. L. Stowe, Characterization of tropospheric aerosol over the ocean with the NOAA Advanced Very High Resolution Radiometer optical thickness operational product, *J. Geophys. Res., 102*, 16889–16909, 1997.

Huffman, D. R., The interaction of light with a small-particle system, *Adv. Phys., 26*, 129–130, 1977.

Liu, L., M. I. Mishchenko, J. W. Hovenier, H. Volten, and O. Muñoz, Scattering matrix of quartz aerosols: comparison and synthesis of laboratory and Lorenz-Mie results, *J. Quant. Spectrosc. Radiat. Transfer, 79-80*, 911–920, 2003.

Masuda, K., Y. Mano, H. Ishimoto, M. Tokuno, Y. Yoshizaki, and N. Okawara, Assessment of the nonsphericity of mineral dust from geostationary satellite measurements, *Remote Sens. Env., 82*, 238–247, 2002.

Mishchenko, M. I., and L. D. Travis, Satellite retrieval of aerosol properties over the ocean using polarization as well as intensity of reflected sunlight, *J. Geophys. Res., 102*, 16989–17013, 1997.

Mishchenko, M. I., and L. D. Travis, Capabilities and limitations of a current FORTRAN implementation of the T-matrix method for randomly oriented, rotationally symmetric scatterers, *J. Quant. Spectrosc. Radiat. Transfer, 60*, 309–324, 1998.

Mishchenko, M. I., J. W. Hovenier, L. D. Travis, T-matrix method and its applications, in *Light Scattering by Nonspherical Particles*, edited by M. I. Mishchenko, J. W. Hovenier, and L. D. Travis, Academic Press, San Diego, 147–172, 2000.

Muñoz, O., H. Volten, J. F. de Haan, W. Vassen, and J. W. Hovenier, Experimental determination of scattering matrices of randomly oriented fly ash and clay particles at 442 and 633 nm, *J. Geophys. Res., 106*, 833–844, 2001.

Nho, E.-Y., B. Ardouin, M. F. Le Cloarec, and M. Ramonet, Origins of Po^{210} in the atmosphere at Lamto, Ivory Coast: Biomass burning and saharan dusts, *Atmos. Env., 30*, 3705–3714, 1996.

Nousiainen, T., and K. Vermeulen , Comparison of measured single-scattering matrix of feldspar particles with T-matrix simulations using spheroids, *J. Quant. Spectrosc. Radiat. Transfer, 79–80*, 1031–1042, 2003.

Sokolik, I. N., and O. B. Toon, Incorporation of mineralogical composition into models of the radiative properties of mineral aerosol from UV to IR wavelengths, *J. Geophys. Res., 104*, 9423–9444, 1999.

Patterson, E. M., Measurements of the imaginary part of the refractive index between 300 and 700 nanometers for Mount St. Helens ash, *Science, 211*, 836–838, 1981.

Volten, H., O. Muñoz, E. Rol, J. F. de Haan, W. Vassen, J. W. Hovenier, K. Muinonen, and T. Nousiainen, Scattering matrices of mineral particles at 441.6 nm and 632.8 nm, *J. Geophys. Res., 106*, 17375–17401, 2001.

Zakharova, N. T., and M. I. Mishchenko, Scattering by randomly oriented thin ice disks with moderate equivalent-sphere size parameters, *J. Quant. Spectrosc. Radiat. Transfer, 70*, 465–471, 2001.

Appendix

Table 2: Line position and intensity and air broadening parameters for error flagged lines in HITRAN-2001 and ULB-UFR-BIRA. Line position and intensity data from [*Schermaul et al.*, 2002] are included as reference.

HIT-01				ULB-04				Schermaul-02	
wn	S	ga	key*	wn	S	ga	key*	wn	S
13502.7740	4.19e-025	0.0710	i	13502.7750	3.30e-025	0.0880	+	13502.7738	3.20e-025
13503.6620	2.89e-026	0.0964	+	13503.6650	2.92e-026	0.0749	i	00000.0000	0.00e-000
13505.8620	2.91e-026	0.0964	+	13505.8620	2.96e-026	0.1191	i	00000.0000	0.00e-000
13508.4440	3.66e-026	0.0558	i	13508.4460	3.09e-026	0.0311	+	00000.0000	0.00e-000
13511.0680	4.24e-025	0.0644	i	13511.0690	3.48e-025	0.0780	w	13511.0676	3.39e-025
13513.2790	5.06e-026	0.0617	+	13513.2820	3.51e-026	0.1651	i	00000.0000	0.00e-000
13513.7210	1.11e-025	0.0644	+	13513.7220	1.06e-025	0.0930	c	13513.7195	1.13e-025
13514.3370	1.07e-025	0.0778	+	13514.3400	9.93e-026	0.0681	i	00000.0000	0.00e-000
13515.0600	9.37e-025	0.0833	w	13515.0610	9.28e-025	0.0770	w	13515.0597	9.10e-025
13524.9330	6.08e-025	0.0817	i	13524.9340	7.66e-025	0.0780	c	13524.9329	7.68e-025
13530.6650	3.55e-025	0.0644	c	13530.6660	2.88e-025	0.0690	i	13530.6643	2.81e-025
13540.2820	4.90e-025	0.0558	p	13540.2830	4.89e-025	0.0450	c	13540.2829	4.38e-025
13543.6180	5.28e-025	0.0710	c	13543.6190	5.47e-025	0.0710	c	13543.6182	5.30e-025
13545.5190	3.22e-025	0.0683	+	13545.5200	3.35e-025	0.0910	w	13545.5179	3.33e-025
13549.4780	9.73e-025	0.0870	c	13549.4790	1.01e-024	0.0850	w	13549.4782	9.92e-025
13571.0550	3.40e-025	0.0722	w	13571.0560	2.95e-025	0.0480	c	13571.0552	2.85e-025
13572.0790	3.53e-025	0.0617	c	13572.0800	3.13e-025	0.0480	i	13572.0789	3.19e-025
13572.6170	1.25e-025	0.0683	c	13572.6180	8.85e-025	0.0500	i	13572.6165	8.72e-025
13572.7980	7.22e-025	0.0778	c	13572.7990	5.93e-025	0.0700	+	00000.0000	0.00e-000
13572.9770	2.15e-025	0.0778	c	13572.9780	1.86e-025	0.0730	+	00000.0000	0.00e-000
13573.1140	2.38e-026	0.0964	c	13573.1130	1.91e-026	0.0900	+	00000.0000	0.00e-000
13573.4470	8.05e-025	0.0683	i	13573.4480	9.24e-025	0.0610	w	13573.4464	9.16e-025
13579.5130	5.13e-025	0.0778	i	13579.5150	4.27e-025	0.0960	+	13579.5138	4.32e-025
13585.3320	8.68e-025	0.0986	c	13585.3330	9.33e-025	0.1090	c	13585.3318	9.26e-025
13589.8560	2.42e-025	0.0964	+	13589.8570	2.47e-025	0.1090	c	13589.8556	2.50e-025
13594.4620	8.13e-025	0.0644	+	13594.4630	8.62e-025	0.0800	c	13594.4617	8.55e-025
13604.9990	5.08e-025	0.0758	c	13605.0010	5.12e-025	0.0810	i	13604.9995	5.07e-025
13605.3270	1.03e-024	0.1089	c	13605.3280	1.10e-024	0.1030	i	13605.3275	1.08e-024
13606.6510	4.37e-025	0.1033	w	13606.6530	4.44e-025	0.0870	w	13606.6518	4.40e-025
13618.6440	5.07e-026	0.1089	+	13618.6530	6.69e-026	0.1301	i	00000.0000	0.00e-000
13618.7210	8.30e-026	0.0964	+	13618.7280	5.05e-026	0.0837	i	00000.0000	0.00e-000
13621.0970	2.92e-026	0.0683	i	13621.0950	2.98e-026	0.0551	+	00000.0000	0.00e-000
13621.4610	4.25e-025	0.0778	i	13621.4620	3.56e-025	0.0890	+	13621.4615	3.58e-025
13625.6880	2.56e-025	0.0810	i	13625.6880	2.22e-025	0.0910	+	13625.6879	2.08e-025
13628.1700	6.47e-025	0.0710	i	13628.1710	5.00e-025	0.0800	+	13628.1703	4.99e-025
13639.2090	2.12e-026	0.0778	i	13639.2160	2.29e-026	0.1021	+	00000.0000	0.00e-000
13642.1860	3.68e-025	0.0505	c	13642.1870	3.18e-025	0.0490	+	13642.1860	3.16e-025
13648.7080	1.10e-024	0.0846	c	13648.7090	1.05e-024	0.0990	+	13648.7078	1.05e-024
13652.7850	1.87e-026	0.0789	+	13652.7860	2.52e-026	0.0401	i	00000.0000	0.00e-000
13667.6030	7.45e-025	0.0942	c	13667.6070	8.74e-025	0.1000	c	13667.6034	7.76e-025
13667.6710	3.48e-025	0.1066	c	13667.6820	2.45e-025	0.0960	c	13667.6746	3.38e-025
13683.8820	5.26e-025	0.0737	i	13683.8830	4.54e-025	0.0780	+	13683.8822	4.54e-025
13684.3200	9.50e-025	0.0919	i	13684.3210	9.06e-025	0.1050	+	13684.3204	9.06e-025
13692.5290	4.48e-025	0.0738	i	13692.5300	3.74e-025	0.0880	+	13692.5293	3.85e-025
13706.3430	4.12e-025	0.0644	i	13706.3440	3.34e-025	0.0740	+	13706.3432	3.36e-025
13742.6230	1.62e-025	0.0778	i	13742.6240	1.56e-025	0.0830	i	13742.6226	1.64e-025
13743.3550	2.80e-025	0.0843	+	13743.3570	2.96e-025	0.0990	i	13743.3555	3.10e-025
13744.1270	6.51e-025	0.0644	i	13744.1280	5.25e-025	0.0870	+	13744.1270	5.17e-025
13754.7930	7.62e-025	0.0750	i	13754.7940	6.07e-025	0.0810	w	13754.7925	6.05e-025
13762.8110	2.48e-025	0.0644	i	13762.8120	2.01e-025	0.0820	+	13762.8107	1.93e-025
13771.1590	6.76e-025	0.1068	c	13771.1590	4.96e-025	0.0930	+	13771.1580	5.12e-025
00000.0000	0.00e-000	0.0000	+	13776.9410	1.02e-025	0.0900	c	00000.0000	0.00e-000
13776.9840	1.77e-025	0.0964	+	13776.9910	1.11e-025	0.0730	c	13776.9856	1.45e-025

HIT-01				ULB-04				Schermaul-02	
wn	S	ga	key*	wn	S	ga	key*	wn	S
13779.0620	1.20e-025	0.0964	c	13779.0630	1.09e-025	0.0420	i	13779.0619	9.85e-026
13812.2350	8.65e-025	0.0844	c	13812.2360	8.61e-025	0.0730	w	13812.2347	8.58e-025
13812.4810	3.48e-025	0.0844	i	13812.4810	2.89e-025	0.0690	+	13812.4799	2.99e-025
13825.6000	1.71e-025	0.0710	i	13825.6020	1.46e-025	0.0660	+	13825.6013	1.66e-025
13844.9740	7.84e-026	0.0683	+	13844.9750	8.65e-026	0.0321	i	00000.0000	0.00e-000
13848.4180	7.48e-025	0.0778	p	13848.4180	8.18e-025	0.0740	c	13848.4193	6.32e-025
13855.1630	6.20e-025	0.0900	i	13855.1650	5.10e-025	0.0960	+	13855.1633	5.03e-025
13857.0720	4.03e-025	0.0644	i	13857.0740	3.21e-025	0.0920	+	13857.0720	3.19e-025
13865.2400	9.99e-026	0.0710	i	13865.2420	8.62e-026	0.0911	+	00000.0000	0.00e-000
13869.9020	1.95e-025	0.0993	+	13869.9070	1.86e-025	0.0460	i	13869.9000	2.02e-025
13869.9690	2.83e-025	0.0644	x	13869.9750	2.91e-025	0.0330	i	13869.9707	2.70e-025
13885.4940	3.54e-025	0.0680	i	13885.4950	2.70e-025	0.0810	+	13885.4934	2.70e-025
13918.3210	1.33e-025	0.0964	i	13919.0870	4.85e-025	0.1030	+	13919.0862	4.93e-025
13932.7750	5.92e-025	0.0710	i	13932.7760	4.96e-025	0.0820	+	13932.7746	4.91e-025
13945.5390	3.38e-025	0.0282	i	13945.5400	3.18e-025	0.0650	+	13945.5390	3.19e-025
13950.1220	1.39e-025	0.0964	+	13950.1200	1.52e-025	0.2410	i	13950.1201	1.44e-025
13950.6200	3.87e-025	0.0617	c	13950.6250	4.39e-025	0.0430	+	13950.6202	3.31e-025
13955.0790	3.95e-025	0.0617	c	13955.0800	3.44e-025	0.0490	c	13955.0786	3.37e-025
13956.2100	1.65e-025	0.0558	c	13956.2100	1.50e-025	0.0370	i	13956.2093	1.50e-025
13957.3090	3.25e-025	0.0710	i	13957.3150	4.65e-025	0.0990	+	13957.3080	3.36e-025
13960.2920	4.93e-026	0.0943	c	13960.2930	4.65e-026	0.0491	+	00000.0000	0.00e-000
13972.2580	3.48e-025	0.0683	c	13972.2590	2.83e-025	0.0750	c	13972.2580	2.86e-025
13975.6330	2.14e-025	0.0964	+	13975.6340	2.18e-025	0.0830	i	13975.6330	2.14e-025
14001.4820	3.57e-026	0.0964	+	14001.4800	5.94e-026	0.0591	i	00000.0000	0.00e-000
14005.5400	1.69e-025	0.0406	i	14005.5410	1.38e-025	0.0760	+	14005.5401	1.38e-025
14005.6850	5.48e-026	0.0778	i	14005.6900	4.09e-026	0.1091	+	00000.0000	0.00e-000
14006.0970	9.51e-026	0.0810	+	14006.1020	7.48e-026	0.0951	i	00000.0000	0.00e-000
14009.5120	4.32e-026	0.0964	+	14009.5110	3.55e-026	0.0501	i	00000.0000	0.00e-000
14021.1060	2.37e-025	0.0458	p	14021.1050	2.02e-025	0.0700	i	14021.1039	2.14e-025
14021.5630	1.45e-025	0.0964	i	00000.0000	0.00e-000	0.0000	i	00000.0000	0.00e-000
14049.8930	3.72e-025	0.0587	x	14049.8960	2.71e-025	0.0900	w	14049.8934	3.33e-025
14051.7470	5.08e-026	0.1003	i	14051.7510	3.96e-026	0.0931	+	00000.0000	0.00e-000
14053.0230	1.84e-025	0.0608	i	14053.0400	2.95e-025	0.0880	p	00000.0000	0.00e-000
00000.0000	0.00e-000	0.0000	i	14053.0400	2.95e-025	0.0880	p	00000.0000	0.00e-000
14053.0550	1.86e-025	0.0710	i	14053.0400	2.95e-025	0.0880	p	00000.0000	0.00e-000
14060.1700	1.49e-025	0.0891	i	14060.1670	1.54e-025	0.0800	i	14060.1662	1.57e-025
14062.2000	1.83e-025	0.1037	i	14062.2040	2.96e-025	0.0990	i	00000.0000	0.00e-000
14062.4270	2.01e-025	0.0617	c	14062.4270	2.06e-025	0.0450	+	14062.4264	1.94e-025
14062.6600	1.24e-025	0.0921	i	00000.0000	0.00e-000	0.0000	+	00000.0000	0.00e-000
14067.8510	5.06e-025	0.0844	i	14067.8520	3.95e-025	0.0940	+	14067.8516	3.97e-025
14068.4250	6.42e-025	0.0778	i	14068.4260	5.42e-025	0.0940	+	14068.4248	5.44e-025
14073.4540	5.32e-026	0.0993	i	14073.4480	4.31e-026	0.0571	+	00000.0000	0.00e-000
14076.1230	5.47e-025	0.0737	p	14076.1250	5.21e-025	0.0960	w	14076.1230	5.16e-025
14092.4500	4.91e-025	0.0683	c	14092.4510	4.64e-025	0.0570	c	14092.4499	4.54e-025
14104.1660	5.72e-025	0.0840	c	14104.1670	7.54e-025	0.0980	+	14104.1653	7.17e-025
14112.1730	3.60e-026	0.0844	i	14112.1710	3.25e-026	0.0491	+	00000.0000	0.00e-000
14115.0560	1.60e-025	0.0843	i	14115.0540	1.54e-025	0.1060	i	14115.0530	1.55e-025
14115.6110	1.91e-025	0.0789	+	14115.6110	1.57e-025	0.0880	i	14115.6097	1.60e-025
14116.3470	4.50e-026	0.0844	+	14116.3420	4.34e-026	0.0121	i	00000.0000	0.00e-000
14118.4820	4.31e-025	0.0701	c	14118.4850	3.68e-025	0.0910	+	14118.4825	3.99e-025
14121.1950	6.91e-025	0.0758	c	14121.1950	7.04e-025	0.0650	c	14121.1943	6.96e-025
14122.7240	7.14e-025	0.0848	c	14122.7250	7.88e-025	0.0890	+	14122.7237	7.83e-025
14123.9020	9.04e-025	0.0955	c	14123.9040	9.35e-025	0.1040	c	14123.9030	9.13e-025
00000.0000	0.00e-000	0.0000	+	14131.4280	1.08e-025	0.0980	c	14131.4273	1.09e-025
14133.1200	2.35e-025	0.0710	+	14133.1200	1.96e-025	0.0890	i	14133.1190	1.95e-025
14135.3760	4.53e-025	0.0710	i	14135.3760	3.66e-025	0.0960	i	14135.3754	3.69e-025
14146.6940	5.20e-025	0.0766	i	14146.6960	4.35e-025	0.0870	c	14146.6947	4.31e-025
14155.9130	3.50e-026	0.0758	i	14155.9160	2.27e-026	0.1221	+	00000.0000	0.00e-000
14157.3700	6.32e-025	0.0986	i	14157.3710	7.63e-025	0.1010	c	14157.3702	7.54e-025

HIT-01				ULB-04				Schermaul-02	
wn	S	ga	key*	wn	S	ga	key*	wn	S
14161.1930	1.33e-025	0.0644	x	14161.1920	2.51e-025	0.1350	c	00000.0000	0.00e-000
14170.9790	6.17e-025	0.0975	c	14170.9790	5.24e-025	0.0990	c	14170.9784	5.19e-025
14186.7900	8.71e-025	0.0841	i	14186.7910	1.09e-024	0.0950	c	14186.7908	1.14e-024
14193.1540	3.20e-025	0.0505	p	14193.1540	2.67e-025	0.0520	i	14193.1532	2.69e-025
14193.8940	4.17e-026	0.0644	+	14193.9000	3.11e-026	0.0771	i	00000.0000	0.00e-000
14197.1120	8.18e-025	0.0922	+	14197.1140	8.28e-025	0.0950	p	14197.1127	8.26e-025
14219.5190	3.85e-025	0.0710	c	14219.5200	3.35e-025	0.0650	c	14219.5191	3.35e-025
14239.8630	7.13e-025	0.0883	c	14239.8630	5.96e-025	0.0910	c	14239.8626	5.93e-025
14250.6370	9.70e-025	0.0711	c	14250.6380	1.03e-024	0.0750	c	14250.6372	1.02e-024
14260.0750	2.66e-025	0.0701	i	14260.0760	2.13e-025	0.0830	+	14260.0755	2.19e-025
14261.6700	1.12e-024	0.1030	w	14261.6700	1.18e-024	0.1060	c	14261.6695	1.18e-024
14262.9400	5.31e-025	0.0993	i	14262.9420	4.53e-025	0.1020	c	14262.9410	4.54e-025
14264.9520	5.76e-025	0.0875	+	14264.9540	5.70e-025	0.0940	w	14264.9533	5.70e-025
14266.0670	1.98e-025	0.0796	i	14266.0500	4.13e-025	0.0870	+	14266.0497	3.50e-025
14272.7320	4.98e-025	0.0889	+	14272.7330	4.04e-025	0.1130	i	14272.7318	4.09e-025
14277.4100	8.33e-025	0.1018	c	14277.4110	8.94e-025	0.1010	w	14277.4103	8.93e-025
14298.5370	5.14e-025	0.0872	c	14298.5380	5.40e-025	0.0880	c	14298.5368	5.38e-025

* Legend

+ = No error
i = Line intensity error
w = Line width error
p = Line position error
c = Combination of errors
x = Unclassified feature

Summary

This thesis is dedicated to two atmospheric constituents: water vapor and mineral aerosol and in particular to their interaction with sunlight. We validated and tested state-of-the-art knowledge about the light scattering by mineral aerosol and about light absorption by water vapor in the visible and the near infrared part of the electro-magnetic spectrum. We identified limitations of existing data and models, tested various new approaches and indicated directions for future improvements. In the following the studies presented in this thesis are summarized and their scientific relevance is outlined briefly.

Water vapor absorbs light mainly in the visible and in the infrared. It is responsible for a large part of the natural greenhouse effect and plays an important role in the Earth's weather and climate. Atmospheric water vapor is extensively monitored using measurements of reflected sunlight from satellite-borne spectrometers. The amount of water vapor is derived from the intensity of the reflected light that is measured as a function of the wavelength. Especially the weak absorption features in the visible and near infrared have a large diagnostic potential because of the large amounts of atmospheric water vapor. An accurate knowledge of the water vapor absorption spectrum is a precondition for this retrieval. The water vapor absorption spectrum is so complex that it must be derived from a combination of theory and experiments using complex long path absorption cell measurements. Therefore, the water vapor spectroscopy data need independent validation.

In the first part of the thesis, we validated existing spectroscopic data in the context of radiative transfer simulations and water vapor retrievals under atmospheric conditions. To this end, we compared ground-based Fourier transform spectrometer measurements of transmitted sunlight with radiative transfer simulations. These measurements have been made at the Rutherford Appleton Laboratory (UK). We used measurements with a high spectral resolution such that individual absorption lines are resolved. The spectral resolution used is comparable with the spectral resolution of laboratory experiments that are dedicated to water vapor spectroscopy, and is better than the spectral resolution of most satellite instrument that measure water vapor using reflected sunlight. We evaluated the spectroscopic data of various state-of-the-art databases for two absorption bands at the wavelengths from 585 to 605 nm and from 700 to 740 nm, which are spectral regions containing very many absorption lines. The weak 585-605 nm band is interesting for water vapor retrievals due to the absence of saturation. The absorption of sunlight in the 700-740 nm band is also relevant for the Earth radiation balance. For the 700-740 nm band (Chapter 2), we quantified the information content of the ground-based spectrum about the spectroscopic line parameters. Furthermore, we derived accuracy requirements for atmospheric profile information used in the radiative transfer simulations. We compared this information content in the ground-based spectrum with the accuracy of line parameters given in spectroscopic databases. Based on this comparison we automatically selected lines for which the ground-based measurement adds information or is a significant test. For these lines, a list of error-flagged line parameters was derived. The results of this validation were validated for a subset of the line parameters using an independent dataset that had been measured with an exceptionally high signal to noise ratio. For the 585-605 nm band we derived a global quality estimate for various databases (Chapter 3). For lines that show little blending, we derived the sign and the amplitude of line intensity parameter errors. Furthermore, we quantified the impact of line parameter errors on satellite observations of reflected sunlight with moderate resolution (like GOME measurements). A threshold water vapor column has been provided above which the database errors become significant in such satellite observations. These studies provide a valuable input for future spectroscopy campaigns and have also facilitated line list compilations used as inputs for HITRAN-2004, a recently released spectroscopic database.

A large fraction of the atmospheric aerosol is mineral aerosol. Mineral aerosol reflects and absorbs sunlight and has an impact on the radiative properties and the lifetime of clouds. Currently, one of the largest uncertainties of the Earth radiation balance is due to deficiencies in our knowledge of aerosols. Atmospheric aerosols are monitored from spaceborne and from ground-based instruments that measure reflected or transmitted sunlight. In order to retrieve the amount and the type of the aerosol the light scattering properties of the aerosol have to be known accurately. Whereas the light scattering properties of spherical particles can be easily determined using Mie theory, these properties are very difficult to predict for irregular mineral particles. Light scattering models that can treat particles with internal inhomogeneities and shapes with no symmetries are too slow to be used for aerosol retrievals, which require very efficient light scattering simulations. In practice, shape approximations are used. Experimental data are currently the only reference for the light scattering properties of truly irregular particles.

The second part of this thesis is dedicated to the knowledge of the light scattering properties of mineral aerosols and the light scattering models used for radiative transfer simulations. We confronted the predictions of light scattering models with measured scattering matrices that had been measured in the laboratory with a nephelometer experiment. In order to make a meaningful comparison, the mineral samples measured have to be well-characterized. Chapter 5 is dedicated to the characterization of the size distribution of the mineral samples. In the widely-used spheroidal shape approximation the irregular shapes are represented by an ensemble of oblate and prolate spheroids. In Chapter 6 we tested the consistency of measurements with simulations based on the spheroidal shape approximation in a systematic way. An innovative light scattering model based on a combination of two techniques has been introduced, tested and evaluated (Chapter 7). The irregular shapes are modeled statistically using the Gaussian random sphere model based on objective shape information that is extracted from microscope images of the mineral samples. The light scattering by these model shapes was simulated using the discrete dipole approximation. In Chapter 8, we investigate the impact of shape approximations on satellite observations of reflected sunlight. The results of these studies are relevant for aerosol monitoring from ground-based sun and sky radiometer measurements and from satellite-borne instruments measuring reflected sunlight.

Our intention was to extend the knowledge of the interactions of atmospheric water vapor and mineral aerosol with sunlight, to identify shortcomings in the existing models and databases, and to estimate the impact of related approximations and uncertainties on satellite observations. In the case of water vapor, it was shown that the quality of the existing spectroscopic databases could be further refined using atmospheric observations. We also gave recommendations for the necessary experimental accuracies required to substantially improve the databases. In the case of mineral aerosol, efficient light scattering models that are applicable to irregular aerosol particles are still lacking. Therefore, experimental light scattering data remain a valuable source of reference. A strong impact on aerosol remote sensing may be achieved if a large number of dust samples with well defined properties can be generated. Here large progress should and can be made still.

Samenvatting

Dit proefschrift is gewijd aan twee in onze atmosfeer aanwezige stoffen, namelijk waterdamp en mineraal aerosol, en aan de interactie van deze beide stoffen met zonlicht. Wij hebben onze huidige kennis over de verstrooiing van licht aan dit type aerosol en over de absorptie door waterdamp van het zichtbare en nabij-infarode deel van het elektromagnetische spectrum getoetst en gevalideerd. Ons onderzoek heeft beperkingen in de beschikbare gegevens en modellen aan het licht gebracht. Daarnaast hebben wij nieuwe benaderingen geprobeerd op grond waarvan wij verbeteringen voorstellen. In de nu volgende samenvatting leest u meer over de onderzoeken beschreven in dit proefschrift.

Waterdamp absorbeert zonlicht vooral in het infrarood en in mindere mate bij zichtbare en nabij-infrarode golflengtes. Deze absorptie is verantwoordelijk voor een groot deel van het natuurlijke broeikaseffect en speelt daarom een belangrijke rol in het weer en het klimaat op aarde. Waterdamp in onze atmosfeer wordt voortdurend bepaald door metingen met satellietinstrumenten van zonlicht na reflectie aan de atmosfeer en aan het aardoppervlak. De hoeveelheden waterdamp worden bepaald uit de vorm van de waargenomen lijnspectra. Deze spectra geven de intensiteit van het gereflecteerde zonlicht als functie van de golflengte en bestaan uit een groot aantal scherpe absorptielijnen. Het blijkt dat vooral de relatief zwakke absorptie in het zichtbare en in het nabij-infrarood de grootste potentie heeft als diagnostiek juist vanwege de grote hoeveelheden waterdamp in onze atmosfeer. Het is duidelijk dat kwantitatieve kennis over het waterspectrum een noodzakelijke voorwaarde is voor de bepaling van de waterdamp hoeveelheden. Water bestaande uit drie atomen is ogenschijnlijk een simpel molecuul. Echter, haar absorptie gedrag is zo complex dat het nog niet mogelijk is om met voldoende nauwkeurigheid het spectrum volledig theoretisch te voorspellen. Daarom is een combinatie van theorie en experiment noodzakelijk. Waterspectra zijn bepaald in een groot aantal laboratoria met zogenoemde lange-padlengte absorptie technieken.

In het eerste deel van dit proefschrift beschrijven wij de validatie van een aantal bestaande databases voor waterdamp in de context van simulaties van stralingstransport en waterdamp metingen in de atmosfeer. Hiertoe hebben wij spectra, die gemaakt zijn met een Fourier Transform Spectrometer, vergeleken met de resultaten van stralingstransport simulaties. De metingen zijn gemaakt bij het Rutherford Appleton Laboratorium (RAL) in het Verenigd Koninkrijk. Het gebruik van deze zeer gedetailleerde spectra stelde ons in staat meting en simulatie te vergelijken voor elke individuele absorptielijn. Het door ons gebruikte atmosfeerspectrum heeft een oplossend vermogen, dat in de buurt komt van dat gebruikt bij de beste laboratorium metingen. Dit oplossende vermogen is superieur aan dat van de meeste huidige satelliet instrumenten, die gebruikt worden voor waterdamp bepalingen. Wij hebben gekeken naar de databases HITRAN, ESA-WVB en ULB-UFR-BIRA voor twee absorptiebanden, één band tussen 585 nm en 605 nm en een tweede van 700 tot 740 nm. De eerste band is van speciaal belang voor absolute bepalingen aan waterdamp vanwege de afwezigheid van verzadigingseffecten in de atmosfeer. The tweede band is behalve als diagnostiek ook van belang voor de stralingsbalans in onze atmosfeer vanwege de significante absorptie. In het geval van de 700-740 nm band (Hoofdstuk 2) hebben we de informatie-inhoud bepaald van het hoge resolutie spectrum (RAL) met betrekking tot alle lijnparameters. Daarnaast hebben we de noodzakelijke nauwkeurigheid bepaald voor de toestand in de atmosfeer tijdens een meting vanaf de grond in het bijzonder het waterdampprofiel, zodat op grond van stralingstransport berekeningen verbetering van de kennis van het waterspectrum mogelijk is. In een geautomatiseerde procedure selecteren wij absorptie lijnen, waarvoor het RAL spectrum nieuwe informatie toevoegt. Een speciale lijst is opgesteld, waarin de mogelijke fouten in de verschillende database parameters staan samengevat. Deze lijst is verder getoetst in een vergelijking met een onafhankelijke meting met een exceptionele signaal-ruis verhouding voor de lijnsterkte parameter.

We hebben voor de 585-605 nm band de globale kwaliteit van verschillende databases vastgesteld (Hoofdstuk 3). In het geval van geïsoleerde lijnen hebben we verder de grootte en het teken van de fouten in de lijnsterkte parameter bepaald. Tenslotte hebben we de consequentie van deze lijnfouten afgeschat op satellietwaarnemingen met een realistisch, dat wil zeggen beperkt oplossend vermogen, zoals in het geval van metingen met het GOME instrument (Global Ozone Monitoring Experiment). De minimum waterdamp hoeveelheid is vastgesteld waarboven database fouten van belang worden in satellietmetingen. Deze studie bevat niet alleen waardevolle gegevens voor toekomstige meetcampagnes gericht op waterdamp spectroscopie, maar heeft ook tot het maken van verbeterde absorptielijnlijsten bijgedragen die als input zijn gebruikt voor HITRAN-2004.

Naast waterdamp bevat de atmosfeer ook aerosol. Een groot deel van dit aerosol bestaat uit minerale deeltjes (zand, stof, etc.) met een grootte van tien nm tot een paar μm. Mineraal aerosol reflecteert zonlicht, maar kan ook zonlicht absorberen. Daarnaast beïnvloeden deze deeltjes de vorming van wolken, waarbij zowel de stralingseigenschappen als de levensduur van deze wolken veranderen. Daarmee heeft aerosol ook implicaties voor weer en klimaat. Onze gebrekkige kennis over de interacties van aerosol met zonlicht is een belangrijke oorzaak voor de bestaande onzekerheden over de stralingsbalans van onze aarde. Aerosol wordt waargenomen zowel door instrumenten aan boord van satellieten als door instrumenten in grondstations. Alle instrumenten nemen door aerosol verstrooid licht waar. Ook hier geldt dat voor een kwantitatieve bepaling van de hoeveelheid aerosol, kennis van de lichtverstrooiing van aerosol essentieel is. Nu worden de lichtverstrooiingseigenschappen van bolvormige deeltjes zeer goed beschreven met de zogenoemde Mie-theorie. De beschrijving van de lichtverstrooiingseigenschappen van de onregelmatig gevormde minerale deeltjes blijkt echter zeer ingewikkeld. Berekening bij deeltjes met een grootte van de orde van de golflengte met een inhomogene samenstelling en met zeer onregelmatige vorm gaat zelfs met de huidige snelste computers veel te langzaam voor praktische aerosol toepassingen. Daarom worden er in de praktijk benaderingen toegepast; de deeltjes worden meestal homogeen verondersteld en krijgen als benadering een symmetrische vorm. In feite geldt dat experimentele gegevens de enige goede referentie vormen voor het lichtverstrooiingsgedrag van echt onregelmatige aerosol deeltjes.

Het tweede deel van de proefschrift beschrijft ons onderzoek naar de kennis van het lichtverstrooiingsgedrag van minerale deeltjes en naar de sterktes en zwaktes van oude en nieuwe modellen voor lichtverstrooiing voor toepassingen in straling transportberekeningen. We vergelijken de voorspellingen van de verschillende modellen met metingen uitgevoerd in het laboratorium met en zogenaamde nefelometer. Voor een goede vergelijking is het noodzakelijk de gebruikte stof- en aerosolmonsters goed te karakteriseren. Hoofdstuk 5 beschrijft de bepaling van de grootteverdeling van aerosolmonsters gebruik makend van lichtverstrooiing vooral kijkend naar licht dat verstrooid wordt in de voorwaartse richting, een commercieel toegepaste techniek. Wij hebben hierbij gebruik gemaakt van de benadering met sferoïdale deeltjes, ofwel omwentelingsellipsoïden. Hierbij zijn de onregelmatige deeltjes vervangen door een verzameling van oblate (pannenkoeken) en prolate (sigaren) omwentelingsellipsoïden. In hoofdstuk 6 hebben we de bovengenoemde laboratoriummetingen in een systematische studie vergeleken met simulaties op grond van de sferoïdale vormbenadering. In hoofdstuk 7 is een vernieuwde methode getest waarbij twee verschillende modellen voor de lichtverstrooiing werden gecombineerd. Hierbij werden de minerale deeltjes beschreven in de vorm van op specifieke manier vervormde bolvormige deeltjes in het zogenoemde Gaussisch willekeurige bolvorm model (Gaussian random sphere model). Hierbij hebben we de aard van de toegepaste vervorming aangepast aan vorm bepalingen van stofdeeltjes op grond van elektronenmicroscoop afbeeldingen. De lichtverstrooiingseigenschappen werden vervolgens bepaald met de Discrete Dipool benadering, waarbij de deeltjes opgebouwd worden uit een groot aantal discrete dipolen. In hoofdstuk 8, tenslotte, hebben we bepaald in welke mate verschillende vormbenaderingen de bepalingen van hoeveelheden aerosol in de atmosfeer met behulp van satellietinstrumenten beïnvloeden. We zien dat het van groot belang is om een goed model voor mineraal aerosol te gebruiken om grote fouten te voorkomen bij het doen van deze satellietbepalingen. Onze resultaten hebben ook consequenties voor de analyse van hoeveelheden aerosol en de specifieke fysisch-chemische eigenschappen van het aerosol met behulp van metingen van grondstations.

De motivatie van ons onderzoek was een verbetering van onze kennis over de interactie van zonlicht met atmosferisch waterdamp en atmosferisch mineraal aerosol, het identificeren van tekortkomingen in gebruikte modellen en in gebruikte databases en het bepalen van de consequenties van de verschillende tekortkomingen en benaderingen op de interpretatie van satellietmetingen. In het geval van waterdamp blijkt dat de kwaliteit van de databases verbeterd kunnen worden zelfs met behulp van metingen in de atmosfeer. In het geval van onregelmatig gevormde mineraal aerosol deeltjes ontbreken nog steeds efficiënte rekenmodellen voor de bepaling van de lichtverstrooiingseigenschappen. Voor mineraal aerosol blijven laboratorium bepalingen een belangrijke bron voor referentie gegevens. Het genereren van een groot aantal goed gekarakteriseerde stofmonsters, waarvan de lichtverstrooiingseigenschappen goed bepaald worden, is van groot belang voor een uiteindelijke optimale interpretatie van satellietmetingen. In dit vakgebied zijn grote vorderingen nog duidelijk mogelijk en urgent.

List of publications

Chapters in this thesis

Chapter 2: B. Veihelmann, A. N. Maurellis, K. M. Smith, R. Tolchenov, J. Tennyson, and W. J. van der Zande, Capabilities of ground-based solar occultation measurements in the validation of line spectroscopy: water vapor - a case study, to be submitted.

Chapter 3: B. Veihelmann, R. Lang, K. M. Smith, D. A. Newnham, and W. J. van der Zande, Evaluation of spectroscopic databases of water vapor between 585 and 600 nm, *Geophys. Res. Lett., 29*, doi:10.1029/2002GL015330, 2002.

Chapter 5: B. Veihelmann, M. Konert, and W. J. van der Zande, Laser particle sizing of mineral dust: a comparison of light scattering models, in preparation.

Chapter 6: B. Veihelmann, O. Dubovik, H. Volten, O. Muñoz and W. J. van der Zande, Scattering matrices of irregular mineral dust samples: the consistency of measurements and simulations using the spheroidal shape approximation, in preparation.

Chapter 7: B. Veihelmann, T. Nousiainen, F. M. Kahnert, and W. J. van der Zande, Light scattering by small feldspar particles simulated using the discrete dipole approximation for Gaussian random spheres, to be submitted.

Chapter 8: B. Veihelmann, H. Volten, and W. J. van der Zande, Light reflected by an atmosphere containing irregular mineral dust aerosol, *Geophys. Res. Lett., 31*, doi: 10.1029/2003GL018229, 2004.

Other Publications

B. Veihelmann, T. Nousiainen, F. M. Kahnert, and W. J. van der Zande, Light scattering by small feldspar particles simulated using the discrete dipole approximation for Gaussian random spheres, *Proceedings of the 8th Conference on Electromagnetic and Light Scattering by Non-spherical Particles, Granada*, accepted.

F. M. Kahnert, T. Nousiainen, and B. Veihelmann, Spherical and spheroidal model particles as an error source in aerosol climate forcing and radiation computations: a case study for feldspar aerosols, *J. Geophys. Res.*, accepted.

T. Nousiainen, F. M. Kahnert, and B. Veihelmann, Light scattering modeling of small feldspar particles using simplified shapes, *J. Quant. Spectrosc. Radiat. Transfer*, in press.

O. Muñoz, H. Volten, J. W. Hovenier, B. Veihelmann, W. J. van der Zande, L. B. F. M. Waters, and W. I. Rose, Scattering matrices of volcanic ash particles of Mount St. Helens, Redoubt, and Mount Spurr volcanoes, *J. Geophys. Res., 109*, doi:10.1029/2004JD004684, 2004.

B. Veihelmann, O. Dubovik, H. Volten, and W. J. van der Zande, Mineral Dust Aerosol: Microphysical Properties and Scattering Matrix, *Proc. AERONET/PHOTONS Workshop*, 2004.

O. Dubovik, A. Syniuk, T. Lapyonok, B. Holben, M. Mishchenko, P. Yang, A. Vermeulen, T. Eck, I. Slutsker, H. Volten, and B. Veihelmann, Accounting for non-sphericity of aerosol particles in polarimetric remote sensing of desert dust, *Proc. AERONET/ PHOTONS Workshop*, 2004. http://www.aeronet.gsfc.nasa.gov/spain2004/spain_presentations.html

O. Dubovik, A. Syniuk, T. Lapyonok, B. Holben, M. Mishchenko, P. Yang, H. Volten, B. Veihelmann, A. Vermeulen, T. Eck, and I. Slutsker, Modeling scattering by non-spherical particles in photopolarimetric remote sensing of desert dust aerosol, *Proc. Workshop "Advances in light scattering by particle systems"*, 2004.

B. Veihelmann, H. Volten, and W. J. van der Zande, Simulations of light scattered by an atmosphere containing irregularly shaped mineral aerosol over the ocean, *Proceedings of the 7th Conference on Electromagnetic and Light Scattering by Non-spherical Particles, Bremen*, 2003.

B. Veihelmann, H. Volten and W. J. van der Zande, Light scattering by irregularly shaped mineral aerosol, *Proc. NATO ASI on Photopolarimtery in Remote Sensing*, 2003.

B. Veihelmann, H. Volten, and W. J. van der Zande, Scattering by irregularly shaped mineral dust aerosol: radiative transfer simulations in the Earth's atmopshere, *EGS - AGU - EUG Joint Assembly*, 3446-+, 2003.

B. Veihelmann, K. M. Smith, D. A. Newnham, and W. J. van der Zande, Water vapor absorption in the weak vibrational rotational overtone band at 588 to 600 nm, *EGS XXVII General Assembly, 27*, 1821-+, 2002.

B. Veihelmann, F. S. Olesen, and C. Kottmeier, Sea ice surface temperature in the Weddell-Sea (Antartica) from drifting buoy and AVHRR data, *Cold Regions Sci. and Techn., 33*, 19–27, 2001.

B. Veihelmann and H. Nett, System modeling and testing of MIPAS/Envisat, *Final Report, Envisat System & Payload Project Division, ESA/ESTEC*, 2001.

Acknowledgement

I would like to thank my promotor Wim van der Zande for giving me the opportunity to do this PhD. I appreciate very much your enthousiastic and enthousing support. You encourage playful and independent thinking and you gave me the freedom to try out new ways. With your very positive approach you assisted me in boiling the essential out of my results and helped me to make my work converge to a thesis. I regard you as an outstandingly good scientific supervisor and a very nice person to work with.

Thank you Ahilleas Maurellis for copromoting my PhD and for supporting me scientifically. I enjoyed very much the exciting and fruitful discussions we had. You gave me a deeper insight in the topics we worked on together and a broader view on science.

I am grateful to you Oleg Dubovik for your openness, your generosity, and your scientific support. Our collaboration was a great enrichment for me. I would like to thank you Rüdiger Lang and Hester Volten for the ideas and impulses you gave me. Your work provided the scientific basis for the projects that resulted in my thesis. I would also like to thank Timo Nousiainen, Michael Kahnert, Kevin Smith, Olga Munoz, Martin Kohnert, Roman Tolchenov, and Jonathan Tennyson, for collaborating with me in such a fruitful way. I would like to thank Michiel Min, Daphne Stam, Johan de Haan, Joop Hovenier, and Thomas Wriedt for the enriching discussions and their interest in my work.

I am grateful to my group at AMOLF, namely Andreas, Laura, Annemieke, Hester, Rüdiger, Jason, Afric and Anouk. Thank you for sharing offices with me, for the time we spent at the lunch club with nice bread and houmous, and for all those small things that make everyday's life at work worth while. When I came to AMOLF I received immediate help with housing; for this I thank Dimitri Petrov, Christian Buggle, and Roudy van der Wijk. I am also greatful to the E&I department at AMOLF, especially to Rutger Schoone, for the technical support.

Thanks are due to the EOS group at SRON for being my scientific home base in the last year of my thesis. Thank you Ilse Aben for offering me a desk in your room. I am grateful to Bert van den Bovenkamp and Chiel Galama from SRON for saving my computers and my data after a hacker attack.

I want to thank Alfons Hoekstra and Leo Meerts for providing access to the super computers at SARA and at the Radboud University Nijmegen. An integral part of my thesis is based on the extensive light scattering simulations that you made possible.

Thank you Andreas and Laura for spending many evenings in and out in Amsterdam. I hope there will be many more. Thank you Georgiana for your love and your friendship.

The back cover shows two satellite images. The upper right image has been taken by the Meteosat satellite. This near-infrared image shows atmospheric water vapor above Europe (copyright EUMETSAT 2005). The lower left image has been taken in the visible by the Sea-viewing Wide Field-of-view Sensor (SeaWiFS, NASA). This image shows atmospheric mineral aerosol over the Eastern Mediterranean.